UNIVERSITY OF CALIFORNIA

Los Angeles

Explorations in Catalysis including Polymer Synthesis, Applications, and Design Aspects

A thesis submitted in partial satisfaction of the

requirements for the degree Master of Science

in Chemistry

by

Ashton Richard Davis

2022

ABSTRACT OF THE THESIS

Explorations in Catalysis including Polymer Synthesis, Applications, and Design Aspects

by

Ashton Richard Davis

Master of Science in Chemistry

University of California, Los Angeles, 2022

Professor Paula Loredana Diaconescu, Chair

This thesis contains results from three different projects as well as a perspective. In the first project, a nickel bromide complex supported by a non-innocent ferrocene-chelating heteroscorpionate ligand, [(fc(PPh_2)($BH(3,5\text{-}Me_2pz)_2$)NiBr] (($fc^{P,B}$)NiBr, fc = 1,1'-ferrocenediyl, pz = pyrazole), was synthesized and characterized. The compound can be readily oxidized according to UV-vis and ^{1}H NMR spectroscopy. The catalytic activity of the complex's different oxidation states in the polymerization of vinyl monomers was explored. AB and ABA-type block copolymers were made from styrene and p-chlorostyrene, offering an example of orthogonal redox control in radical polymerization.

The second project focuses on organometallic scandium chemistry. The compound (salfen)ScCl (salfen = *N*,*N'*-bis(2,4-di-*tert*-butylphenoxy)-1,1'-ferrocenediimine) was

successfully synthesized and characterized by ^{1}H and ^{13}C NMR spectroscopy. Unfortunately, synthesis of alkoxide analogues of this scandium compound could not be cleanly achieved.

The third project focuses on finding biodegradable alternatives to friction reducers used in hydraulic fracturing. Quenching experiments with poly(ethylene glycol) are attempted. Promising results are seen using poly(succinimide) derivatives.

The perspective covers design principles in compartmentalization. Several examples showcasing different aspects of compartmentalization are covered. It is ultimately determined that structure and space are the two most important aspects to consider when designing a compartment.

The thesis of Ashton Richard Davis is approved.

Amy Catherine Rowat

Chong Liu

Paula Loredana Diaconescu, Committee Chair

University of California, Los Angeles

2022

This thesis is dedicated to my parents for always being there, my friends for listening to me rant, and my dog for seeing our family through 5 degrees.

TABLE OF CONTENTS

TABLE OF FIGURES

List of Abbreviations and Symbols

fc	1,1'-ferrocenediyl
Fc	ferrocenium
pz	pyrazole
Me	methyl
Me	methyl
dppc	1,1'-bis(diphenylphosphino)-cobaltocene
($fc^{P,B}$)	$fc(PPh_2)(BH(3,5\text{-}Me_2pz)_2$
OPh	phenoxide
Ph	phenyl
p-MOS	*para*-methoxystyrene
MMA	methyl methacrylate
p-CS	*para*-chlorostyrene
n-BuMA	*n*-butyl methacrylate
EVE	ethyl vinyl ether
δ	chemical shift
ppm	parts per million
NMR	nuclear magnetic resonance
SEC	size exclusion chromotography
$CoCp_2$	cobaltocene
BAr^F	tetrakis(3,5-bis(trifluoromethyl)phenyl)borate
DFB	1,2-difluorobenzene
TBA	tetrabutylammonium

DME	1,2-dimethoxyethane
ATRP	atom transfer radical polymerization
salfen	1,1’-bis(2,4-di-*tert*-butyl-6-salicylimine) ferrocene
thiolfan*	1,1'-bis (2,4-di-*tert*-butyl-6-thiophenoxy)ferrocene
ROP	ring opening polymerization
DFT	density functional theory
PCA	principal component analysis
TMEDA	tetramethylethylenediamine
THF	tetrahyrdofuran
*n*BuLi	*n*-butyl lithium
LTMDS	lithium tetramethyldisilazane
TMDS	tetramethyldisilazane
LDA	lithium diisoproylamine
DIPA	diisoproylamine
PAM	poly(acrylamide)
HPAM	partially hydrolyzed poly(acrylamide)
C-PAM	cationic poly(acrylamide)
PEG	poly(ethylene glycol)
PSI	poly(succinimide)
PHEA	poly[(2-hydroxyethyl)-DL-aspartamide]
FENE	finite extensible nonlinear elastic
API	American Petroleum Institute
cP	centipoise

TMP	tetramesityl porphyrin
TTPPP	5,10,15,20-tetrakis(2’,4’,6’-triphenylphenyl)porphyrinato

ACKNOWLEDGMENTS

Beyond anything, this work represents the influence my teachers, colleagues, and friends have had along the way, so obviously some acknowledgements are in order.

Nathalie Co for being the most reliable person I've ever had the pleasure of working with and for convincing me to start in organometallics in the first place.

Nima Adhami for both scaring me to death pretty much every time he walked into the room and teaching me a ridiculous amount of technique.

Shuangshuang Li for starting the nickel project presented here, and my lab mates Nima Adhami, Hootan Roshandel, Yi Shen, and Nathalie Co for their help in investigation and reviewing.

Carl Aften and other members of the ACS Green Chemistry Institute Oilfield Institute Roundtable for their funding and constructive feedback on friction reducing polymer project. The people in Professor Samanvaya Srivastava's group, notably Defu Li and Advait Holkar for teaching me the necessary rheology for the oilfield experiments.

The Royal Chemical Society for permission to reprint Figure 3.2 from *Chem. Commun.* **2019**, *55* (49), 7021-7024.

While the work is not presented in this thesis, a special thanks to Amy Rowat for taking a chance on me and letting me into her group to explore my passions in food science. Sam Norris, Stephanie Kawecki, and Kathleen Chen for being instrumental in my development in cellular biology and for being some of the kindest, most caring lab-mates I've met.

And last but not least, Paula Diaconescu. Words cannot describe the amount of admiration and reverence I have for this woman and the work she does. A true powerhouse of the field and always going above and beyond as a mentor.

I truly relish my time working with you all. Thank you for the opportunity and the pleasure.

Chapter 1: Prelude

1.1 Catalysis

Catalysis as a phenomenon has been known since ancient times, but the first formalization of the term can be traced to Jöns Jakob Berzelius in 1835.[1, 2] However, it wasn't until 1894, that Ostwald posited the first physical definition still in use today.[3] Catalysis describes the process of increasing the rate of a chemical reaction by adding a sub-stoichiometric amount of a known substance which undergoes no net physical change during the course of the reaction.[4] This once misunderstood subject is now the corner stone of many synthetic practices, and catalysis has given access to a wide variety of chemicals that would not be possible without it.[5]

1.2 Inorganic catalysis

While biocatalysis in the form of fermenting sugar into alcohol was the first type of catalysis exploited by humans, the first record of inorganic catalysis is from 1552 where Valerius Cordus used sulfuric acid to catalyze the conversion of alcohols into ethers.[1, 6] Evidence of catalysts' ability to be recovered in an unaltered state after a reaction occurred came in 1817. Humphry Davy reported the autoignition of several substances in the presence of platinum or palladium wires at temperatures far lower than they would normally burn at, and the ability to reuse the wire.[7]

Since the 1800s, various types of catalysts have been developed and systematically studied, and a slew of applications have been developed from polymerization to hydroelementation reactions and everything in between.[8-10] While there are a number of categories that catalysts can be divided into, they are generally heterogenous or homogenous in nature. Inorganic catalysts can take on many different forms within these categories, and the diversity of catalysts available has been key to transform readily available building blocks into high value molecules and materials.[11]

1.3 Organometallic catalysis

The Diaconescu group focuses on the development and characterization of various types of organometallic catalysts. The behavior of these catalysts can be greatly influenced by the ligands attached to them and the microenvironment the complexes sit in. As a result, the fine tuning of these aspects can impact the reactivity of the compounds and give access to novel reactivities.

1.3.2 Redox switchable catalysis

The field of switchable catalysis has been growing exponentially in the past decade. Recently, chemists have started to develop catalysts whose reactivity can be altered in the presence of an external stimuli.[11] While there are examples in photo-, pH-, coordination-, and mechanically-driven switching, the Diaconescu group's emphasis has been on redox switching with a focus on polymerization reactions.

Redox switchability is often imparted to a catalyst through the ligand framework, and the reactivity of catalyst can be altered *in situ* by introducing oxidants or reductants.[12] The more well behaved examples of redox switchability are based on ligand frameworks that have pendant metallocenes. In 1995, Writghton and coworkers developed a Rh(I) complex supported by dppc (1,1'-bis(diphenylphosphino)-cobaltocene), and the reaction rates of hydrogenation and hydrosilylation could be altered depending on the oxidation state of the complex.[13] More commonly, ferrocene is used as the redox active moiety because of its stability and well characterized reactivity.[14] In 2006, White and coworkers delivered the first example of a pedant ferrocene moiety that could be used to switch the polymerization of lactide on and off with chemical oxidants and reductants.[15] This work was the genesis of the study of redox switchable polymerizations.[16]

While examples of the redox active element and the metal performing the catalysis are the same are known, these systems are often harder to study the reactivity of.[17-20] Therefore, the ligand frameworks employed by the Diaconescu group all contain pendant ferrocene moieties. The two ligand frameworks that will be the focus of the first half of this thesis are ferrocene-based heteroscorpionate ($fc^{P,B}$) [($fc^{P,B}$) = (fc(PPh_2)(BH(3,5-Me_2pz)$_2$), fc = 1,1'-ferrocenediyl, pz = pyrazole] and salfen. The heteroscorpionate chemistry is based on the original ($fc^{P,B}$)NiCl synthesized by our group in 2015, and attempts to apply redox control over the NiBr version of the compound to radical polymerization.[21] The salfen chemistry attempts to create a scandium analogue of [(salfen)Y(OPh)]$_2$ to investigate the effects of structural differences discovered in our 2019 computational study.[22, 23]

1.3.1 Compartmentalization

Another way to alter behavior of organometallic catalysts – besides engineering functional ligands – is to place them inside of compartments. Reactivities can change wildly as a result of confinement, leading to differences in selectivities as well as reaction rates.[24-31] As useful of a synthetic tool as confinement can be, its implementation is often cumbersome and accidental. Therefore, the last portion of this thesis offers a perspective on design elements to consider when confining organometallic catalysts, and the reader is directed to that chapter for a more in-depth background.

1.4 Integrated catalysis

To date, most catalytic systems studied rely on a singular catalyst to do a singular transformation. With so many different types of catalysis at chemist's disposal, there is an opportunity to start coupling different types of catalysts together. This will give access to more complex chemistries from simpler feedstocks by allowing the product of one catalyst to be the

substrate for the next. However, in order to make the scientific connections that integrating catalytic systems demands, the fundamentals of various types of catalysis need to be understood quite well. Therefore, this thesis is by no means about any singular type of catalysis or catalytic outcome. Instead, this work represents an intellectual grounding in various forms of catalysis as a primer to be able to start integrating systems. A lot of this work focus on polymer synthesis and characterization because polymers offer a useful lens to study reactivity through, but this work mainly presents how I conceptualize catalysts (typically organometallic ones) and how that conceptualization can be put to use.

1.5 References

(1) Wisniak, J. The History of Catalysis. From the Beginning to Nobel Prizes. *Educación Química* **2010**, *21* (1), 60-69.

(2) Berzelius, J. Sur un force jusqu'ici peu remarquée qui est probablement active dans la formation des composes organiques, Section on Vegetable Chemistry. *Jahres-Bericht* **1835**, *14*, 237.

(3) Ostwald, W. Definition der Katalyse. *Z. Phys. Chem.* **1894**, *15*, 705-706.

(4) Rodriguez, A. M. B.; Binks, B. P. Catalysis in Pickering emulsions. *Soft Matter* **2020**, *16* (45), 10221-10243, 10.1039/D0SM01636E.

(5) Kim, U. B.; Jung, D. J.; Jeon, H. J.; Rathwell, K.; Lee, S.-g. Synergistic Dual Transition Metal Catalysis. *Chem. Rev.* **2020**, *120* (24), 13382-13433.

(6) Cordus, V. Le Guidon des Apotiquaires: C'est à dire, la Vraye Forme et Maniere de Composer les Médicamens. *L. Cloquemin, E. Michel, Lyons,* **1575**.

(7) Davy, H. VIII. Some new experiments and observations on the combustion of gaseous mixtures, with an account of a method of preserving a continued light in mixtures of inflammable gases and air without flame. *Philos. Trans. R. Soc. London* **1817**, (107), 77-85.

(8) Shamiri, A.; Chakrabarti, M. H.; Jahan, S.; Hussain, M. A.; Kaminsky, W.; Aravind, P. V.; Yehye, W. A. The Influence of Ziegler-Natta and Metallocene Catalysts on Polyolefin Structure, Properties, and Processing Ability. *Materials (Basel)* **2014**, *7* (7), 5069-5108, PubMed.

(9) Walkowiak, J.; Szyling, J.; Franczyk, A.; Melen, R. L. Hydroelementation of diynes. *Chem. Soc. Rev.* **2022**, *51* (3), 869-994, 10.1039/D1CS00485A.

(10) Hayler, J. D.; Leahy, D. K.; Simmons, E. M. A Pharmaceutical Industry Perspective on Sustainable Metal Catalysis. *Organometallics* **2019**, *38* (1), 36-46.

(11) Blanco, V.; Leigh, D. A.; Marcos, V. Artificial switchable catalysts. *Chem. Soc. Rev.* **2015**, *44* (15), 5341-5370.

(12) Allgeier, A. M.; Mirkin, C. A. Ligand Design for Electrochemically Controlling Stoichiometric and Catalytic Reactivity of Transition Metals. *Angew. Chem. Int. Ed.* **1998**, *37* (7), 894-908.

(13) Lorkovic, I. M.; Duff Jr, R. R.; Wrighton, M. S. Use of the redox-active ligand 1, 1'-bis (diphenylphosphino) cobaltocene to reversibly alter the rate of the rhodium (I)-catalyzed reduction and isomerization of ketones and alkenes. *J. Am. Chem. Soc.* **1995**, *117* (12), 3617-3618.

(14) Heinze, K.; Lang, H. Ferrocene—Beauty and Function. *Organometallics* **2013**, *32* (20), 5623-5625.

(15) Gregson, C. K. A.; Gibson, V. C.; Long, N. J.; Marshall, E. L.; Oxford, P. J.; White, A. J. P. Redox Control within Single-Site Polymerization Catalysts. *J. Am. Chem. Soc.* **2006**, *128* (23), 7410-7411.

(16) Wei, J.; Diaconescu, P. L. Redox-Switchable Ring-Opening Polymerization with Ferrocene Derivatives. *Acc. Chem. Res.* **2019**, *52* (2), 415-424.

(17) Broderick, E. M.; Guo, N.; Vogel, C. S.; Xu, C.; Sutter, J.; Miller, J. T.; Meyer, K.; Mehrkhodavandi, P.; Diaconescu, P. L. Redox Control of a Ring-Opening Polymerization Catalyst. *J. Am. Chem. Soc.* **2011**, *133* (24), 9278-9281.

(18) Sauer, A.; Buffet, J. C.; Spaniol, T. P.; Nagae, H.; Mashima, K.; Okuda, J. Switching the lactide polymerization activity of a cerium complex by redox reactions. *ChemCatChem* **2013**, *5* (5), 1088-1091.

(19) Biernesser, A. B.; Delle Chiaie, K. R.; Curley, J. B.; Byers, J. A. Block Copolymerization of Lactide and an Epoxide Facilitated by a Redox Switchable Iron-Based Catalyst. *Angew. Chem. Int. Ed.* **2016**, *55* (17), 5251-5254.

(20) Biernesser, A. B.; Li, B.; Byers, J. A. Redox-Controlled Polymerization of Lactide Catalyzed by Bis(imino)pyridine Iron Bis(alkoxide) Complexes. *J. Am. Chem. Soc.* **2013**, *135* (44), 16553-16560.

(21) Abubekerov, M.; Diaconescu, P. L. Synthesis and Characterization of Ferrocene-Chelating Heteroscorpionate Complexes of Nickel(II) and Zinc(II). *Inorg. Chem.* **2015**, *54* (4), 1778-1784.

(22) Deng, S.; Diaconescu, P. L. A switchable dimeric yttrium complex and its three catalytic states in ring opening polymerization. *Inorg. Chem. Front.* **2021**, *8* (8), 2088-2096.

(23) Lai, A.; Clifton, J.; Diaconescu, P. L.; Fey, N. Computational mapping of redox-switchable metal complexes based on ferrocene derivatives. *Chem. Commun.* **2019**, *55* (49), 7021-7024.

(24) Natinsky, B. S.; Jolly, B. J.; Dumas, D. M.; Liu, C. Efficacy analysis of compartmentalization for ambient CH4 activation mediated by a RhII metalloradical in a nanowire array electrode. *Chem. Sci.* **2021**, *12* (5), 1818-1825.

(25) Natinsky, B. S.; Lu, S.; Copeland, E. D.; Quintana, J. C.; Liu, C. Solution Catalytic Cycle of Incompatible Steps for Ambient Air Oxidation of Methane to Methanol. *ACS Cent. Sci.* **2019**, *5* (9), 1584-1590.

(26) Jolly, B. J.; Co, N. H.; Davis, A. R.; Diaconescu, P. L.; Liu, C. A generalized kinetic model for compartmentalization of organometallic catalysis. *Chem. Sci.* **2022**.

(27) Liu, Y.; Wang, Y.; Wang, Y.; Lu, J.; Piñón, V.; Weck, M. Shell Cross-Linked Micelle-Based Nanoreactors for the Substrate-Selective Hydrolytic Kinetic Resolution of Epoxides. *J. Am. Chem. Soc.* **2011**, *133* (36), 14260-14263.

(28) Lee, S. J.; Cho, S.-H.; Mulfort, K. L.; Tiede, D. M.; Hupp, J. T.; Nguyen, S. T. Cavity-Tailored, Self-Sorting Supramolecular Catalytic Boxes for Selective Oxidation. *J. Am. Chem. Soc.* **2008**, *130* (50), 16828-16829.

(29) Collman, J. P.; Zhang, X.; Hembre, R. T.; Brauman, J. I. Shape-selective olefin epoxidation catalyzed by manganese picnic basket porphyrins. *J. Am. Chem. Soc.* **1990**, *112* (13), 5356-5357.

(30) Torque, C.; Sueur, B.; Cabou, J.; Bricout, H.; Hapiot, F.; Monflier, E. Substrate-selective aqueous organometallic catalysis. How small water-soluble organic molecules enhance the supramolecular discrimination. *Tetrahedron* **2005**, *61* (20), 4811-4817.

(31) Chen, Z.; Cui, Z.-M.; Li, P.; Cao, C.-Y.; Hong, Y.-L.; Wu, Z.-Y.; Song, W.-G. Diffusion Induced Reactant Shape Selectivity Inside Mesoporous Pores of Pd@meso-SiO2 Nanoreactor in Suzuki Coupling Reactions. *J. Chem. Phys. C* **2012**, *116* (28), 14986-14991.

Chapter 2: Application of a ferrocene-chelating heteroscorpionate ligand in nickel mediated radical polymerization

2.1 Introduction

Redox switchable catalysis has been gaining traction over the past decade as a method to obtain control over polymer architecture by changing electron density at either the ligand framework or the metal center.[1-7] The use of external stimuli such as chemical redox agents or electricity to control the oxidation states of catalysts can be exploited to turn on and off different complementary catalytic reactions.[8-11] This form of orthogonal reactivity has been extensively explored by our group[12-17] and others[18-22] in ring open polymerization of cyclic esters and ethers, yet there has been a limited number of attempts to expand the scope of redox controlled systems.[1, 7, 23-33]

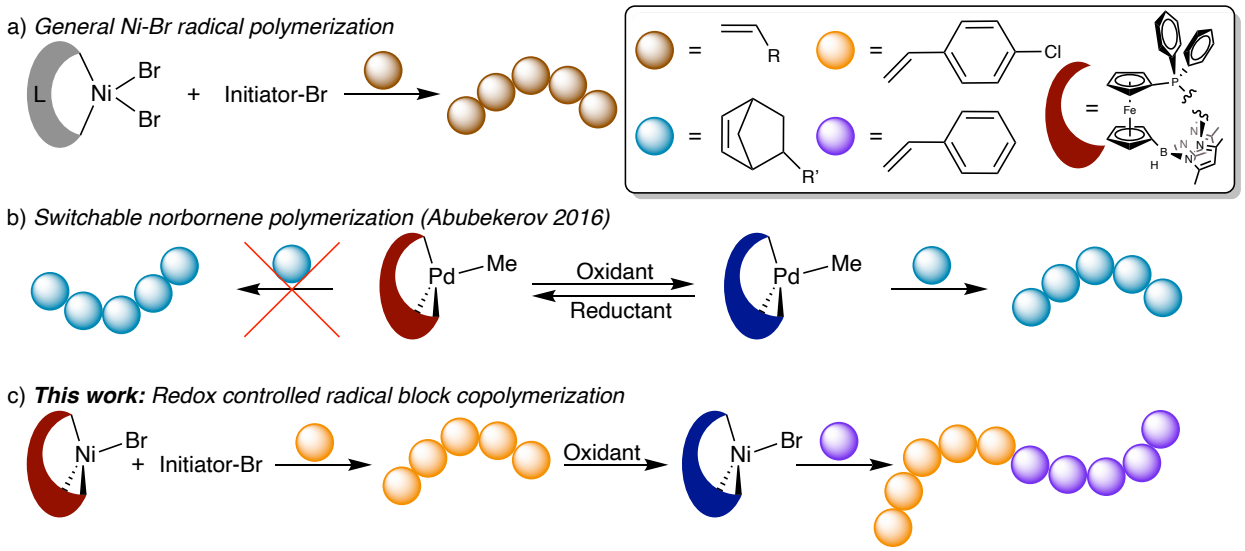

Figure 2.1 Rationale for investigating ($fc^{P,B}$)NiBr. (a) General Ni-Br radical polymerization where L is a generic neutral ligand. (b) Switchable behavior of ($fc^{P,B}$)PdMe in norbornene polymerization. (c) Redox dependent behavior of ($fc^{P,B}$)NiBr in radical block copolymerizations.[34]

Nickel halide complexes, particularly nickel bromides,[35-37] in the presence of an initiator, are active radical polymerization systems with notable examples in atom transfer radical polymerization (ATRP, Figure 2.1a).[38, 39] The rates of polymerization and equilibria in ATRP can

be influenced via changes in the redox state of the supporting ligand in metal halide species.[40] While ferrocene systems in conjunction with copper have been previously investigated,[41] the influence of the redox states of ferrocene on monomer activity and selectivity has not been investigated. Therefore, we set out to probe the effects of redox states in radical polymerization with the goal of expanding the scope of active systems for redox switchable catalysis.

We previously reported ferrocene-chelating heteroscorpionate metal complexes in order to synthesize olefinic copolymers by utilizing a chemical redox switch.[42] The palladium-alkyl heteroscorpionate [(fc(PPh_2)(BH(3,5-Me_2pz)$_2$)PdMe] (($fc^{P,B}$)PdMe, fc = 1,1'-ferrocenediyl, pz = pyrazole) was successfully used as a catalyst in the switchable polymerization of norbornene derivatives; albeit only one oxidation state was catalytically active (Figure 2.1b).[34] A brief foray into nickel chemistry revealed an incompatibility in redox behaviors of the iron contained in the ferrocene moiety and nickel, unlike what was observed with the palladium system.[42] Particularly, in the case of the nickel alkyl complex ($fc^{P,B}$)NiMe, the tendency of both metals to undergo one electron redox processes at similar potentials results in an irreversible loss of the alkyl ligand, rendering this compound unfit for redox-switchable polymerization of vinyl monomers. However, the nickel halide complex, ($fc^{P,B}$)NiCl, displays two distinct redox events, which can be attributed to the supporting ligand and nickel. The reversibility of these events warrants further investigation into the nickel halide heteroscorpionates and their potential application in redox switchable catalysis. Since nickel bromide compounds used in radical polymerization have historically given better polymer properties than nickel chloride species,[37, 43-46] we set out to investigate whether ($fc^{P,B}$)NiBr would be a good candidate for radical polymerization of vinyl monomers utilizing the principles of redox switchable catalysis (Figure 2.1c).

Herein, we report the synthesis and characterization of a ferrocene-based heteroscorpionate nickel halide complex, ($fc^{P,B}$)NiBr, which shows excellent orthogonal reactivity in two different oxidation states. A monomer screen, consisting of styrene, *p*-chlorostyrene (p-CS), methyl methacrylate (MMA), *n*-butyl methacrylate (n-BuMA), and acrylonitrile was conducted. As a proof-of-concept, AB and ABA type block copolymers of styrene and *p*-chlorostyrene were also synthesized by the sequential addition of monomers and redox reagents.

2.2 Results and discussion

2.2.1 Synthesis and characterization of the nickel bromide complex

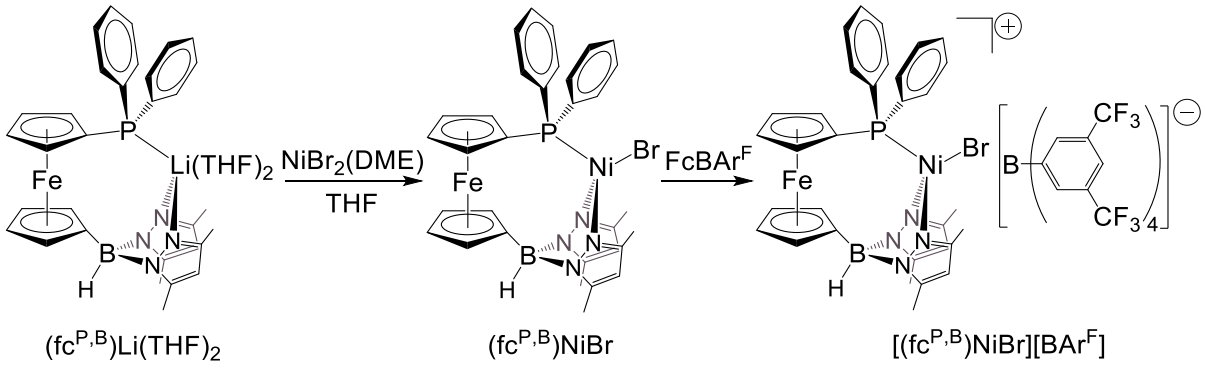

Figure 2.2 Synthesis of ($fc^{P,B}$)NiBr and [($fc^{P,B}$)NiBr][BArF] from ($fc^{P,B}$)Li(THF)$_2$.

($fc^{P,B}$)NiBr was synthesized by reacting ($fc^{P,B}$)Li·(THF)$_2$ with NiBr$_2$(DME) in THF at room temperature (Figure 2.2).[42] Attempts to characterize ($fc^{P,B}$)NiBr via ^{1}H NMR spectroscopy resulted in only broad, uninformative peaks as expected for a paramagnetic compound (Figure S10). The solid-state molecular structure of ($fc^{P,B}$)NiBr was determined by single-crystal X-ray diffraction (Figure 2.3). The coordination environment around the nickel center has a distorted tetrahedral geometry with a τ value of 0.84.[47] The metal−ligand distances (P(1)−Ni(1), 2.3235(7) Å;

Br(1)−Ni(1), 2.3488(4) Å; N(2)−Ni(4), 1.9567(19) Å; N(1)−Ni(1), 1.965(2) Å) match closely with those of the analogous ($fc^{P,B}$)NiCl.[42]

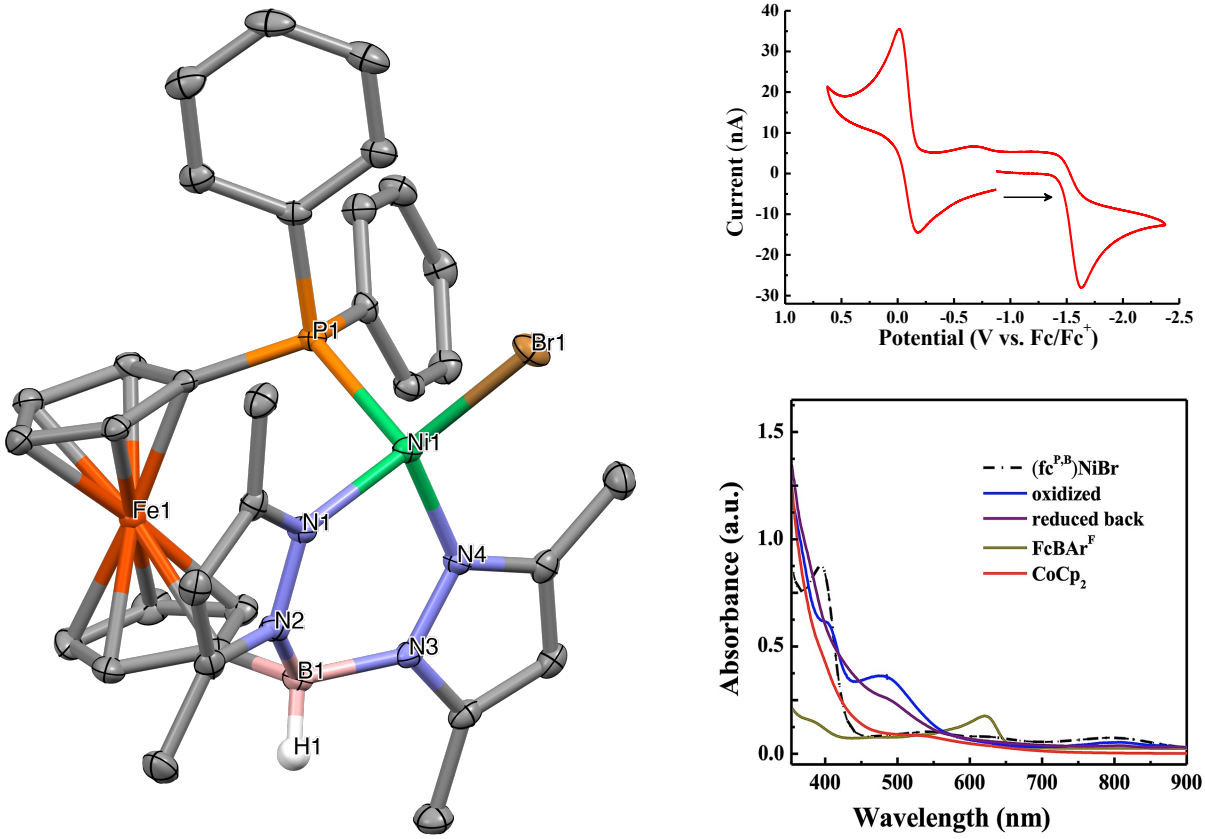

Figure 2.3 Characterization of ($fc^{P,B}$)NiBr**.** *Left:* Thermal ellipsoid (50% probability) representation of (fcP,B)NiBr; hydrogen atoms (except for B-H) and co-crystalized toluene were omitted for clarity. *Top right:* Redox behavior of (fcP,B)NiBr; cyclic voltammogram recorded with a glassy carbon electrode at 100 mV/s in THF, 0.10 M [TBA][PF6] containing 1.0 mM (fcP,B)NiBr. E1/2 = -0.09 V, -1.62 V. *Bottom right:* UV-vis study of different (fcP,B)NiBr species (0.29 mM) in 1,2-difluorobenzene.

The redox behavior of ($fc^{P,B}$)NiBr was studied using cyclic voltammetry performed in a tetrabutylammonium hexafluorophosphate ([TBA][PF_6]) solution in THF (Figure 2.3). ($fc^{P,B}$)NiBr displayed a quasi-reversible redox process at $E_{1/2}$ = -0.09 V vs Fc/Fc^+ with an i_{pc}/i_{pa} = 1.65, and a second irreversible oxidation event at $E_{1/2}$ = -1.62 V vs Fc/Fc^+. This behavior differs significantly from ($fc^{P,B}$)NiCl, which displayed two reversible redox events at $E_{1/2}$ = -0.03 V and $E_{1/2}$ = -1.58 V vs Fc/Fc^+ that were previously assigned to the ferrocene moiety and nickel, respectively.[42]

Meanwhile, the *in situ* reactions with $FcBAr^F$ (Fc = ferrocenium, BAr^F = tetrakis(3,5-bis(trifluoromethyl)phenyl)borate) as the oxidant [48] and $CoCp_2$ (cobaltocene) as the reductant in a mixture of 1,2-difluorobenzene (DFB) and C_6D_6 were monitored by ^1H NMR spectroscopy (Figure S13). No obvious peaks were observed in the oxidized spectrum, and the return of the original broad peaks was not observed after reduction with $CoCp_2$, suggesting the original compound could not be regenerated.

A qualitative solution state magnetic susceptibility study further corroborated these results as the original difference in chemical shift of the internal standard could not be regenerated and the peak splitting became quite complex (Figure S14).[49]

The color of the mixture changed during the oxidation and reduction processes, gradually from dark green to a dark-reddish brown when the oxidation occurred over the course of two hours. However, the return of the dark green color was not observed after the addition of $CoCp_2$. To help verify that the original compound is not restored upon reduction with $CoCp_2$, UV-vis data was collected (Figure 2.3). The absorbance at 392 nm in $(fc^{P,B})NiBr$ slowly disappears and an absorbance at 488 nm appears as the compound is reacted with $FcBAr^F$. Upon reaction with $CoCp_2$, the absorbance at 392 nm is not regenerated, further indicating that the original compound cannot be regenerated.

Elemental analysis results of the reduced and oxidized states of $(fc^{P,B})NiBr$ were in agreement with the calculated values. These data are consistent with an oxidized species being generated with $FcBAr^F$, and it was reasoned that the coordination of a substrate may enhance the stability of the catalytically active species. A similar situation was observed by us previously when investigating the effect of the redox state of (thiolfan*)$Zr(NEt_2)_2$ (thiolfan*= 1, 1'-bis (2,4-di- *tert*-butyl-6-thiophenoxy)ferrocene) on the hydroamination of primary and secondary aminoalkenes.[50]

2.2.2 Homopolymerization reactions

Table 2.1 Homopolymerization of various monomers by ($fc^{P,B}$)NiBr and [($fc^{P,B}$)NiBr][BArF].

Entry	Catalyst[a]	Monomer[b]	Time (h)	T (°C)	Conv. (%)	$M_{n_{calc}}$ (kg/mol)[c]	$M_{n_{exp}}$ (kg/mol)[d]	$Đ$[d]
1	**red**	styrene	70	80	NR	-	-	-
2	**ox**	styrene	0.1	RT	>99	9.9	4.6	1.40
3	**red**	*p*-CS	44	80	93	11.4	12.6	1.14
4	**ox**	*p*-CS	44	RT	<20	N/D[e]	N/D[e]	N/D[e]
5	**red**	MMA	123	80	NR	-	-	-
6	**ox**	MMA	123	RT	91	9.8	10.1	1.09
7	**red**	*n*-BuMA	44	80	95	13.1	9.9	1.29
8	**ox**	*n*-BuMA	49	RT	38	4.9	3.0	1.05
9	**red**	acrylonitrile	27	80	NR	-	-	-
10	**ox**	acrylonitrile	27	RT	NR	-	-	-

Conditions: monomer (1.05 mmol), ethyl 2-bromoisobutyrate (0.0111 mmol), ($fc^{P,B}$)NiBr (0.0111 mmol), 1,3,5-trimethoxybenzene (TMB) as an internal standard (0.1167 mmol), FcBArF as the oxidant (0.0111 mmol), and C_6D_6 and o-difluorobenzene as the solvent (a total volume of 0.5 mL); [a] "red" and "ox" refer to the reduced and in situ generated oxidized compound. [b] *p*-CS = *p*-chlorostyrene, MMA = methyl methacrylate, *n*-BuMA = *n*-butyl methacrylate. [c] Determined by ^{1}H NMR spectroscopy. [d] Determined by SEC. [e] Not determined.

The activity of ($fc^{P,B}$)NiBr and [($fc^{P,B}$)NiBr][BAr^F] toward styrene, *p*-chlorostyrene (*p*-CS), methyl methacrylate (MMA), *n*-butyl methacrylate (*n*-BuMA), and acrylonitrile polymerization was investigated in order to ascertain the effect of redox states on reactivity in radical polymerization (Table 2.1). For styrene and MMA, only the oxidized compound was active, and no activity could be observed for the reduced state (Table 2.1, entries 1-2 and 5-6). MMA reached 91% conversion after 123 hours, while styrene reached full monomer conversion after only 0.1 hours (Figures S15, S17). Poly(styrene) (PS) and poly(methyl methacrylate) (PMMA), displayed a narrow unimodal distribution, with dispersities of 1.40 and 1.09, respectively (Figures S28, S30). Both *p*-CS and *n*-BuMA displayed preferential activity toward the reduced compound, achieving a 93% and 95% conversion after 44 hours, respectively (Table 2.1, entries 3-4 and 7-8). Poly(*p*-chlorostyrene) (PCS) and poly(*n*-butyl methacrylate) (P*n*-BuMA) were well controlled and

displayed a narrow unimodal distribution, with dispersities of 1.14 and 1.09, respectively (Figures S29, 32). Though P*n*-BuMA obtained via the oxidized compound displayed a narrow unimodal distribution with a dispersity of 1.05, the conversion rate of the monomer was only 38% (Figure S33). Acrylonitrile was not active toward the oxidized nor the reduced compound. This is consistent with previous studies that used Cu-based catalysts,[51, 52] and is likely due to the nitrile functional group being too strong of a nucleophile.[34] Relevant control studies (Table S1) favor a radical mechanism.

2.2.3 Copolymerization reactions

Table 2.2 Redox controlled copolymerization studies by ($fc^{P,B}$)NiBr and [($fc^{P,B}$)NiBr][BArF].

Entry	Monomer 1[a]	Monomer 2	Monomer 3	Catalyst[b]	Time (h)	T (°C)	Conv. (%)	$M_{n_{calc}}$ (kg/mol)[c]	$M_{n_{exp}}$ (kg/mol)[d]	$Đ$
1	styrene	-	-	**ox**	0.2	25	90	9.0	6.8	1.10
2	styrene	*p*-CS	-	**ox-red**	0.2-46	25-80	90-18	11.4	10.8	1.33
3	*p*-CS	-	-	**red**	21	80	77	9.4	10.1	1.18
4	*p*-CS	styrene	-	**red-ox**	21-44	80-25	77-72	16.6	15.5	1.17
5	*p*-CS	styrene	*p*-CS	**red-ox-red**	21-44-44	80-25-80	77-72-37	21.1	19.4	1.24

Conditions: monomer (1.05 mmol), ethyl 2-bromoisobutyrate (0.0111 mmol), 1, 3, 5-trimethoxybenzene (TMB) as an internal standard (0.1167 mmol), FcBArF as oxidant (0.0111 mmol), $CoCp_2$ as reductant (0.0111 mmol), and C_6D_6 and *o*-difluorobenzene as solvent. Reaction temperatures were based on homopolymer studies, unless otherwise mentioned. [a] *p*-CS = *p*-chlorostyrene. [b] "red" and "ox" refer to the reduced and in situ generated oxidized compound. [c] Determined by 1H NMR spectroscopy. [d] Determined by SEC

Encouraged by the orthogonal monomer selectivity described above, the synthesis of block copolymers was attempted via redox-switchable radical polymerization. To create an AB diblock, we started with the oxidized compound and polymerized styrene. This was followed by the addition of $CoCp_2$ to alter the catalytic behavior of [($fc^{P,B}$)NiBr][BAr^F] and the addition of *p*-CS to start growing a *p*-CS block resulting in a PS-PCS copolymer with a relatively low *p*-CS conversion (Table 2.2, entry 2). The reverse diblock PCS-PS was also synthesized with greater

success owing to not needing to switch the oxidized compound into a different catalytic state (Table 2.2, entry 4).

In both cases, the activity of the first block is similar to that observed from homopolymerization studies, but that for the second block was comparably slower. While the SEC traces displayed narrow unimodal molecular weight distributions, diffusion order spectroscopy (DOSY) proved inconclusive for the PCS-PS copolymer since each block is of similar molecular weight (Figure S35, S3, S4). However, using the Stejskal-Tanner equation,[53] it was clear that the two blocks in the copolymer have a similar diffusion coefficient, and that if the corresponding homopolymers were present, a faster diffusion coefficient would have been observed (Figure S8). Other diblock copolymers with a variety of monomer combinations were attempted (Table S2), but none of them formed copolymers despite literature precedent for block copolymers of P*n*-BuMA-MMA[36] and P*n*-BuMA-PS.[54]

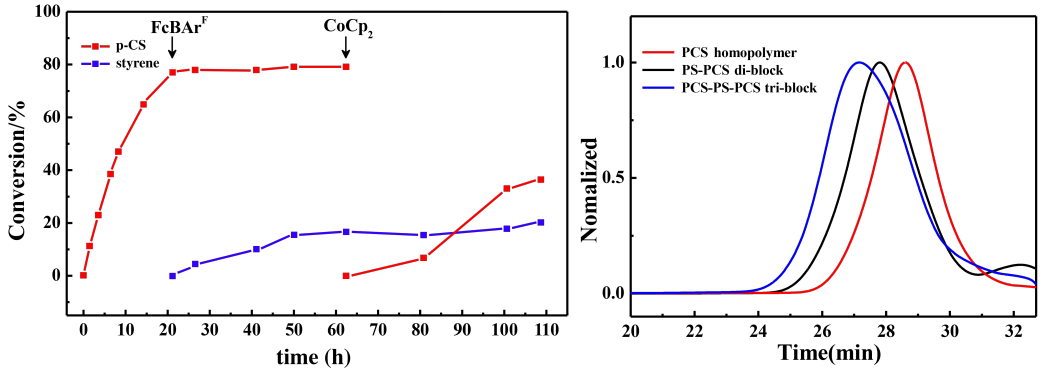

Figure 2.3 Copolymer characterization. *Left:* Plot of conversion (%) vs time for the sequential addition polymerization of *p*-CS and styrene with ($fc^{P,B}$)NiBr using *in situ* oxidation and reduction with $FcBAr^F$ and $CoCp_2$, respectively. *Right:* SEC traces of the PCS homopolymer, PCS-PS diblock copolymer, and the PCS-PS-PCS triblock copolymer (Table 2.2, entries 3-5)**.**

Previous reports of PS-PCS diblock copolymers synthesized via radical polymerization required the use of a PS macro-initiator, and triblock copolymers were not attempted.[55] The only other example of PS and PCS ABA triblock copolymers was synthesized via anionic

polymerization with sodium naphthalene.[56] Therefore, we set out to prepare ABA triblock copolymers of PCS and PS via radical polymerization and to ascertain if the catalytic activity of ($fc^{P,B}$)NiBr was regained after sequential oxidation and reduction. While a PS-PCS-PS copolymer could not be obtained (Table S2, entry 5), sequential addition of $CoCp_2$ to the PCS-PS diblock reaction mixture followed by p-CS led to the formation of a third block, incorporating 37% of *p*-CS after 44 h at 80 °C (Table 2.2, entry 5). Despite the low conversion of the third block, the triblock copolymer exhibits a narrow unimodal distribution (Figure 2.3, Figure S39). DOSY results show only one diffusion coefficient (Figure S5), and the Stejskal-Tanner plot indicates that the blocks in PCS-PS-PCS triblock have a distinct diffusion coefficient from the blocks in PS-PCS diblock (Figure S9). Therefore, it is confirmed that *p*-CS was incorporated as a third block and a triblock copolymer was formed.

Interestingly, the block copolymers synthesized here are the first examples of copolymers made by exploiting the orthogonal reactivity of different oxidation states for radical polymerization systems. Switchable catalysis studies in ATRP tend to focus on electrochemically mediated reactions, where catalysts can only be switched on or off,[57] and the synthesis of block copolymers tends to start from macroinitiators,[58-60] unlike in the present system, which can synthesize block copolymers *de novo*. Expanding the realm of redox switchable catalysts from ring opening polymerizations to include the polymerization of polar vinyl monomers offers an opportunity to couple these systems in future work. The results presented herein are an important step toward achieving both increased complexity and increased temporal control in polymer synthesis.

2.3 Conclusions

The application of a ferrocene-chelating heteroscorpionate ligand in nickel mediated radical polymerization was explored. In the presence of a radical initiator, ($fc^{P,B}$)NiBr is active in *p*-CS and *n*-BuMA polymerization, while the oxidized species is active in styrene, *p*-MOS, and MMA polymerization. Even though the oxidized species could not be chemically reduced back to ($fc^{P,B}$)NiBr, the catalytic nature of [($fc^{P,B}$)NiBr][BAr^F] could still be altered by the addition of a reductant, facilitating the preparation of PCS-PS, PS-PCS, and PCS-PS-PCS block copolymers via sequential monomer addition. These copolymers offer proof-of-concept that redox switchable catalysis can be expanded to radical polymerizations.

2.4 Experimental

General Considerations. All experiments were performed under a dry nitrogen atmosphere in an MBraun glovebox or using standard Schlenk techniques unless otherwise noted. Solvents were purified using a two-column solid-state purification system by the method of Grubbs [61] and transferred to the glovebox without exposure to air. NMR solvents were obtained from Cambridge Isotope Laboratories, degassed, and stored over activated molecular sieves prior to use. NMR spectra were recorded on Bruker AV-300, Bruker AV-400, Bruker DRX-500, or Bruker AV-600 spectrometers at room temperature unless otherwise noted. Chemical shifts are reported with respect to the residual solvent peaks, 7.16 ppm (C_6D_6) and 7.26 ($CDCl_3$) for ^{1}H NMR spectra. The monomers and 1,2-difluorobenzene (DFB) were purchased from Sigma Aldrich or Fisher Scientific and distilled over CaH_2 and then brought into the glovebox without exposure to air. ($fc^{P,B}$)Li(THF)$_2$ [34, 42] and $FcBAr^F$ (Fc = ferrocenium, BAr^F = tetrakis(3,5-bis(trifluoromethyl)-phenyl)borate)[48] were prepared according to literature procedures and, unless otherwise noted, all reagents were acquired from commercial sources and used as received. Elemental analysis of the

reduced and the oxidized compound was performed using an Exeter Analytical, Inc. CE-440 elemental analyzer. The molecular weights of the polymers were determined using a SEC-MALS instrument at UCLA. SEC-MALS uses a Shimazu Prominence-i LC 2030C 3D equipped with an autosampler, two MZ Analysentechnik MZ-Gel SDplus LS 5 μm, 300 × 8 mm linear columns, a Wyatt DAWN HELEOS-II, and a Wyatt Optilab T-rEX. The column temperature was set at 40 °C. The flow rate of the column was kept at 0.70 mL min^{-1} and samples were dissolved in THF. The number average molar mass and dispersity values were d*n*/d*c* values which were calculated by 100% mass recovery from the RI signal.

Synthesis of ($fc^{P,B}$)NiBr. To $NiBr_2$(DME) (DME = 1,2-dimethoxyethane, 0.318 g, 1.03 mmol) in 7 mL THF, a solution of ($fc^{P,B}$)Li$(THF)_2$ (0.729 g, 0.938 mmol) in 2 mL THF was added dropwise at ambient temperature, and the color of the solution changed rapidly from orange to dark greenish-black. The reaction solution was stirred for 2 h. After removal of volatiles under reduced pressure, the product was extracted into 8 mL of toluene, and then filtered through Celite. Reduction in the volume of toluene to about 7 mL *in vacuo* and layering of 10 mL of hexanes afforded a dark green crystalline material after 24 hours at -35°C. Decanting of the solution and washing of the remaining solids with 3mL of cold hexanes yielded the product as a dark green crystalline material (0.52 g, 69.1%). X-ray quality crystals were obtained from a solution of toluene layered with hexanes at -40 °C. The compound is paramagnetic. ^{1}H NMR (500 MHz, 25 °C, C_6D_6): δ (ppm) 19.50 (s,br), 14.62 (s, br), 12.02 (s, br), 4.53(s), 3.34 (s, br), -5.61 (s, br), -10.26 (s, br). ^{13}C NMR (126 MHz, 25 °C, C_6D_6): δ (ppm) 125.70 (s, br, aromatic), 99.75 (s, br, CH), 79.44 (s, Cp-*C*), 70.89 (s, br, Cp-*C*), 67.38 (s, Cp-*C*), 24.32 (s, br, C*C*H_3). ^{31}P NMR (121 MHz, 25 °C, C_6D_6): δ (ppm) 10.26 (s). Anal. ($fc^{P,B}$)NiBr·(C_7H_8) ($C_{39}H_{41}BBrFeN_4NiP$) calcd: C, 58.4; H, 5.11; N, 6.98. Found: C, 58.8; H, 5.13; N, 7.12.

Isolation of [(fc^{P,B})NiBr][BAr^{F}]. A solution of FcBAr^{F} (70.1 mg, 0.067 mmol) in 1,2-difluorobenzene (DFB, 1 mL) was added to a stirring solution of (fc^{P,B})NiBr (53.6 mg, 0.067 mmol) in DFB (1 mL) and allowed to react for 2 h before removing the volatiles under a reduced pressure. The oily residual was washed with cold hexanes three times and benzene was added to redissolve the product. After letting it stand at -35°C overnight, the solution was decanted, and the remaining dark brown oil was dried *in vacuo* for 12 h (90.1 mg, 81%). Attempts to grow crystals of the oxidized compound were unsuccessful. There are no obvious peaks in the corresponding ^{1}H NMR (500 MHz, 25 °C, C_6D_6) spectrum. Anal. [(fc^{P,B})NiBr][BAr^{F}]·(C_7H_8) ($C_{71}H_{53}B_2BrFeN_4NiPF_{24}$) calcd: C, 51.2; H, 3.18; N, 3.36. Found: C, 51.5; H, 3.11; N, 3.41.

Homopolymerizations with (fc^{P,B})NiBr. Under an inert atmosphere, (fc^{P,B})NiBr (11.1 μmol) in 0.2 mL DFB, ethyl 2-bromoisobutyrate (11.1 μmol) in 0.1 mL C_6D_6, 1,3,5-trimethoxybenzene (TMB, 0.117 mmol) in 0.1 mL C_6D_6, and monomer (1.05 mmol) were added to a J-Young NMR tube. The reaction mixture was shaken occasionally. The tube was sealed and brought out of the glovebox and placed in an oil bath when heating was required. The NMR tube was taken out of the oil bath and the monomer conversion was monitored by ^{1}H NMR spectroscopy. When the desired conversion was reached, CH_2Cl_2 was added to dissolve the polymer and the resulting solution was poured into 10 mL of cold methanol to precipitate the polymer; the mixture was centrifuged for 5 min, and the supernatant was decanted. This process was repeated twice to remove the catalyst and unreacted monomer. Polymers containing *p*-chlorostyrene were quenched with acetone and precipitated with ethanol acidified with hydrochloric acid (wt. 5 %) instead of CH_2Cl_2 and methanol. The resulting polymer was dried under reduced pressure before characterization.

Homopolymerization with *in situ* generated [($fc^{P,B}$)NiBr][BAr^F]. Under an inert atmosphere, $FcBAr^F$ (11.1 μmol) in 0.1mL DFB was added dropwise to a stirring solution of ($fc^{P,B}$)NiBr (11.1 μmol) in 0.2 mL DFB. After 2 h, the solution was filtered through Celite and added to a J-Young NMR tube with ethyl 2-bromoisobutyrate (11.1 μmol) in 0.1 mL C_6D_6, TMB (0.1167 mmol) in 0.1 mL C_6D_6, monomer (1.05 mmol). The reaction mixture was left at room temperature while being shaken occasionally. The tube was sealed and brought out of the glovebox and monomer conversion was monitored by ^{1}H NMR spectroscopy.

General procedure for copolymerizations. Under an inert atmosphere, ($fc^{P,B}$)NiBr (11.1 μmol) in 0.2 mL DFB and TMB (0.1167 mmol) in 0.1 mL C_6D_6 were added to a J-Young NMR tube. If starting with the oxidized compound, $FcBAr^F$ (11.1 μmol) in 0.1 mL DFB was added and allowed to react for 2 h followed by ethyl 2-bromoisobutyrate (11.1 μmol) in 0.1 mL C_6D_6. Otherwise, ethyl 2-bromoisobutyrate (11.1 μmol) in 0.1 mL C_6D_6 was added immediately. The NMR tube was charged with monomer (1.05 mmol), sealed, brought out of the glovebox, and placed in an oil bath when a higher than ambient temperature was needed. Monomer conversion was measured by ^{1}H NMR spectroscopy. When a desired conversion was reached, the NMR tube was brought back into the glovebox, and $CoCp_2$ (11.1 μmol) or $FcBAr^F$ (11.1 μmol) in 0.1 mL DFB was added. The reaction mixture was left at room temperature for either 15 min or 2 h, respectively, with occasional shaking before the next monomer was added. This process was repeated for the synthesis of triblock copolymers.

General procedure for polymer isolations. When the desired conversion was reached, CH_2Cl_2 was added to dissolve the polymer and the resulting solution was poured into 10 mL of cold methanol to precipitate the polymer; the mixture was centrifuged for 5 minutes, and the supernatant was decanted. This process was repeated twice to remove the catalyst and unreacted monomer.

Polymers containing *p*-chlorostyrene were quenched with acetone and precipitated with ethanol acidified with hydrochloric acid (5% wt.) instead of CH_2Cl_2 and methanol. The resulting polymer was dried under reduced pressure before characterization.

Cyclic voltammetry study of ($fc^{P,B}$)NiBr. Cyclic voltammetry studies were conducted using a 20 mL scintillation vial with electrodes fixed in position by a rubber stopper, in a 0.10 mM tetrabutylammonium hexafluorophosphate ($TBAPF_6$) solution in THF. A glassy carbon working electrode (planar circular area = 0.071 cm^2), a platinum reference electrode (planar circular area = 0.031 cm^2), and a silver-wire pseudoreference electrode (purchased from CH Instruments) were used. Before starting, the working and auxiliary electrodes were polished with an aqueous suspension of 1.00 μm, 0.30 μm, followed by 0.05 μm alumina on a Microcloth polishing pad with a deionized water. Cyclic voltammograms were acquired with the CH Instrument CHI630D potentiostat and recorded with CH Instruments software (version 13.04). All potentials are given with respect to the ferrocene-ferrocenium couple.

UV-vis spectroscopic studies. UV-vis spectra were recorded on a Hewlett Packard 8453 instrument. DFB was used as the solvent blank. In the glovebox, 0.29 mM solutions of $FcBAr^F$, $CoCp_2$, ($fc^{P,B}$)NiBr, and [($fc^{P,B}$)NiBr][BAr^F] in DFB were prepared in advance. 5 mL of the solution being measured was placed into a 1 cm quartz cuvette that could be sealed with a Schlenk cap, and UV-vis spectra were recorded. Before testing the next species, the cuvette was washed four times with DFB. For the *in situ* redox studies of ($fc^{P,B}$)NiBr, a 0.29 mM solution of ($fc^{P,B}$)NiBr in 5 mL DFB was added to the cuvette and a spectrum was recorded. $FcBAr^F$ was weighed out in a glass vial and 1 mL of the 0.29 mM ($fc^{P,B}$)NiBr solution was used to dissolve the $FcBAr^F$ before quickly transferring the resulting solution back into the cuvette. UV-vis spectra were recorded every 15 minutes for 2 h. $CoCp_2$ was then weighed out in a separate glass vial and 1 mL of the

0.29 mM [($fc^{P,B}$)NiBr][BAr^F] solution was used to dissolve the $CoCp_2$ before quickly transferring the resulting solution back into the cuvette. UV-vis spectra were again recorded every 15 min for 2 h.

X-ray crystallography. X-ray quality crystals were obtained from a toluene solution layered with hexanes and placed in a −35 °C freezer in the glovebox. The X-ray data collections were carried out on a Bruker SMART 1000 single crystal X-ray diffractometer using Cu Kα radiation and a SMART APEX CCD detector. The data was reduced by SAINTPLUS and an empirical absorption correction was applied using the package SADABS. The structure was solved and refined using SHELXTL (Bruker 1998, SMART, SAINT, XPREP AND SHELXTL, Bruker AXS Inc., Madison, Wiscosin, USA). Tables with atomic coordinates and equivalent isotropic displacement parameters, with all the distances and angles and with anisotropic displacement parameters are listed in the cif.

2.5 References

(1) Blanco, V.; Leigh, D. A.; Marcos, V. Artificial switchable catalysts. *Chem. Soc. Rev.* **2015**, *44* (15), 5341-5370.

(2) Allgeier, A. M.; Mirkin, C. A. Ligand Design for Electrochemically Controlling Stoichiometric and Catalytic Reactivity of Transition Metals. *Angew. Chem. Int. Ed.* **1998**, *37* (7), 894-908.

(3) Chen, C. Redox-Controlled Polymerization and Copolymerization. *ACS Catal.* **2018**, *8* (6), 5506-5514.

(4) Wei, J.; Diaconescu, P. L. Redox-Switchable Ring-Opening Polymerization with Ferrocene Derivatives. *Acc. Chem. Res.* **2019**, *52* (2), 415-424.

(5) Deacy, A. C.; Gregory, G. L.; Sulley, G. S.; Chen, T. T. D.; Williams, C. K. Sequence Control from Mixtures: Switchable Polymerization Catalysis and Future Materials Applications. *J. Am. Chem. Soc.* **2021**, *143* (27), 10021-10040.

(6) Teator, A. J.; Lastovickova, D. N.; Bielawski, C. W. Switchable Polymerization Catalysts. *Chem. Rev.* **2016**, *116* (4), 1969-1992.

(7) Cunningham, L.; Benson, A.; Guiry, P. J. Recent developments in the synthesis and applications of chiral ferrocene ligands and organocatalysts in asymmetric catalysis. *Org. Biomol. Chem.* **2020**, *18* (46), 9329-9370.

(8) Hern, Z. C.; Quan, S. M.; Dai, R.; Lai, A.; Wang, Y.; Liu, C.; Diaconescu, P. L. ABC and ABAB Block Copolymers by Electrochemically Controlled Ring-Opening Polymerization. *J. Am. Chem. Soc.* **2021**, *143* (47), 19802-19808.

(9) Doerr, A. M.; Burroughs, J. M.; Gitter, S. R.; Yang, X.; Boydston, A. J.; Long, B. K. Advances in Polymerizations Modulated by External Stimuli. *ACS Catal.* **2020**, *10* (24), 14457-14515.

(10) Zhao, M.; Chen, C. Accessing Multiple Catalytically Active States in Redox-Controlled Olefin Polymerization. *ACS Catal.* **2017**, *7* (11), 7490-7494.

(11) Leibfarth, F. A.; Mattson, K. M.; Fors, B. P.; Collins, H. A.; Hawker, C. J. External Regulation of Controlled Polymerizations. *Angew. Chem. Int. Ed.* **2013**, *52* (1), 199-210.

(12) Broderick, E. M.; Guo, N.; Wu, T.; Vogel, C. S.; Xu, C.; Sutter, J.; Miller, J. T.; Meyer, K.; Cantat, T.; Diaconescu, P. L. Redox control of a polymerization catalyst by changing the oxidation state of the metal center. *Chem. Commun.* **2011**, *47* (35), 9897.

(13) Quan, S. M.; Wang, X.; Zhang, R.; Diaconescu, P. L. Redox Switchable Copolymerization of Cyclic Esters and Epoxides by a Zirconium Complex. *Macromolecules* **2016**, *49* (18), 6768-6778.

(14) Wei, J.; Riffel, M. N.; Diaconescu, P. L. Redox Control of Aluminum Ring-Opening Polymerization: A Combined Experimental and DFT Investigation. *Macromolecules* **2017**, *50* (5), 1847-1861.

(15) Abubekerov, M.; Vlček, V.; Wei, J.; Miehlich, M. E.; Quan, S. M.; Meyer, K.; Neuhauser, D.; Diaconescu, P. L. Exploring Oxidation State-Dependent Selectivity in Polymerization of Cyclic Esters and Carbonates with Zinc(II) Complexes. *iScience* **2018**, *7*, 120-131.

(16) Lai, A.; Hern, Z. C.; Diaconescu, P. L. Switchable Ring-Opening Polymerization by a Ferrocene Supported Aluminum Complex. *ChemCatChem* **2019**, *11* (16), 4210-4218.

(17) Xu, X.; Luo, G.; Hou, Z.; Diaconescu, P. L.; Luo, Y. Theoretical insight into the redox-switchable activity of group 4 metal complexes for the ring-opening polymerization of ε-caprolactone. *Inorg. Chem. Front.* **2020**, *7* (4), 961-971.

(18) Biernesser, A. B.; Delle Chiaie, K. R.; Curley, J. B.; Byers, J. A. Block Copolymerization of Lactide and an Epoxide Facilitated by a Redox Switchable Iron-Based Catalyst. *Angew. Chem. Int. Ed.* **2016**, *55* (17), 5251-5254.

(19) Stößer, T.; Sulley, G. S.; Gregory, G. L.; Williams, C. K. Easy access to oxygenated block polymers via switchable catalysis. *Nat. Commun.* **2019**, *10* (1).

(20) Biernesser, A. B.; Li, B.; Byers, J. A. Redox-Controlled Polymerization of Lactide Catalyzed by Bis(imino)pyridine Iron Bis(alkoxide) Complexes. *J. Am. Chem. Soc.* **2013**, *135* (44), 16553-16560.

(21) Doerr, A. M.; Burroughs, J. M.; Legaux, N. M.; Long, B. K. Redox-switchable ring-opening polymerization by tridentate ONN-type titanium and zirconium catalysts. *Cat. Sci. Technol.* **2020**, *10* (19), 6501-6510.

(22) Delle Chiaie, K. R.; Yablon, L. M.; Biernesser, A. B.; Michalowski, G. R.; Sudyn, A. W.; Byers, J. A. Redox-triggered crosslinking of a degradable polymer. *Polym. Chem.* **2016**, *7* (28), 4675-4681.

(23) Abubekerov, M.; Khan, S. I.; Diaconescu, P. L. Ferrocene-bis(phosphinimine) Nickel(II) and Palladium(II) Alkyl Complexes: Influence of the Fe–M (M = Ni and Pd) Interaction on Redox Activity and Olefin Coordination. *Organometallics* **2017**, *36* (22), 4394-4402.

(24) Shepard, S. M.; Diaconescu, P. L. Redox-Switchable Hydroelementation of a Cobalt Complex Supported by a Ferrocene-Based Ligand. *Organometallics* **2016**, *35* (15), 2446-2453.

(25) Shen, Y.; Shepard, S. M.; Reed, C. J.; Diaconescu, P. L. Zirconium complexes supported by a ferrocene-based ligand as redox switches for hydroamination reactions. *Chem. Commun.* **2019**, *55* (39), 5587-5590.

(26) Maity, R.; Birenheide, B. S.; Breher, F.; Sarkar, B. Cooperative Effects in Multimetallic Complexes Applied in Catalysis. *ChemCatChem* **2021**, *13* (10), 2337-2370.

(27) Lastovickova, D. N.; Teator, A. J.; Shao, H.; Liu, P.; Bielawski, C. W. A redox-switchable ring-closing metathesis catalyst. *Inorg. Chem. Front.* **2017**, *4* (9), 1525-1532.

(28) Lastovickova, D. N.; Shao, H.; Lu, G.; Liu, P.; Bielawski, C. W. A Ring-Opening Metathesis Polymerization Catalyst That Exhibits Redox-Switchable Monomer Selectivities. *Chem. Eur. J.* **2017**, *23* (25), 5994-6000.

(29) Varnado, C. D.; Jr; Rosen, E. L.; Collins, M. S.; Lynch, V. M.; Bielawski, C. W. Synthesis and study of olefin metathesis catalysts supported by redox-switchable diaminocarbene[3]ferrocenophanes. *Dalton Trans.* **2013**, *42* (36), 13251.

(30) Arumugam, K.; Varnado, C. D.; Sproules, S.; Lynch, V. M.; Bielawski, C. W. Redox-Switchable Ring-Closing Metathesis: Catalyst Design, Synthesis, and Study. *Chem. Eur. J.* **2013**, *19* (33), 10866-10875.

(31) Chen, M.; Yang, B.; Chen, C. Redox-Controlled Olefin (Co)Polymerization Catalyzed by Ferrocene-Bridged Phosphine-Sulfonate Palladium Complexes. *Angew. Chem. Int. Ed.* **2015**, *54* (51), 15520-15524.

(32) Dadashi-Silab, S.; Lorandi, F.; Fantin, M.; Matyjaszewski, K. Redox-switchable atom transfer radical polymerization. *Chem. Commun.* **2019**, *55* (5), 612-615.

(33) Dadashi-Silab, S.; Matyjaszewski, K. Iron Catalysts in Atom Transfer Radical Polymerization. *Molecules* **2020**, *25* (7), 1648.

(34) Abubekerov, M.; Shepard, S. M.; Diaconescu, P. L. Switchable Polymerization of Norbornene Derivatives by a Ferrocene-Palladium(II) Heteroscorpionate Complex. *Eur. J. Inorg. Chem.* **2016**, *2016* (15-16), 2634-2640.

(35) Gillies, M. B.; Matyjaszewski, K.; Norrby, P.-O.; Pintauer, T.; Poli, R.; Richard, P. A DFT Study of R−X Bond Dissociation Enthalpies of Relevance to the Initiation Process of Atom Transfer Radical Polymerization. *Macromolecules* **2003**, *36* (22), 8551-8559.

(36) Moineau, C.; Minet, M.; Teyssié, P.; Jérôme, R. Synthesis and Characterization of Poly(methyl methacrylate)-*block*-poly(*n*-butyl acrylate)-*block*-poly(methyl methacrylate) Copolymers by Two-Step Controlled Radical Polymerization (ATRP) Catalyzed by $NiBr_2(PPh_3)_2$. *Macromolecules* **1999**, *32* (25), 8277-8282.

(37) O'Reilly, R. K.; Shaver, M. P.; Gibson, V. C. Nickel(II) α-diimine catalysts for the atom transfer radical polymerization of styrene. *Inorg. Chim. Acta* **2006**, *359* (13), 4417-4420.

(38) Braunecker, W. A.; Matyjaszewski, K. Controlled/living radical polymerization: Features, developments, and perspectives. *Prog. Polym. Sci.* **2007**, *32* (1), 93-146.

(39) Matyjaszewski, K. Atom Transfer Radical Polymerization (ATRP): Current Status and Future Perspectives. *Macromolecules* **2012**, *45* (10), 4015-4039.

(40) Tang, W.; Kwak, Y.; Braunecker, W.; Tsarevsky, N. V.; Coote, M. L.; Matyjaszewski, K. Understanding Atom Transfer Radical Polymerization: Effect of Ligand and Initiator Structures on the Equilibrium Constants. *J. Am. Chem. Soc.* **2008**, *130* (32), 10702-10713.

(41) Sunsin, A.; Wisutsri, N.; Suriyarak, S.; Teanchai, R.; Jindabot, S.; Chaicharoenwimolkul, L.; Somsook, E. Effect of ferrocene moieties on the copper-based atom transfer radical polymerization of methyl methacrylate. *J. Appl. Polym. Sci.* **2009**, *113* (6), 3766-3773.

(42) Abubekerov, M.; Diaconescu, P. L. Synthesis and Characterization of Ferrocene-Chelating Heteroscorpionate Complexes of Nickel(II) and Zinc(II). *Inorg. Chem.* **2015**, *54* (4), 1778-1784.

(43) Uegaki, H.; Kotani, Y.; Kamigaito, M.; Sawamoto, M. Nickel-Mediated Living Radical Polymerization of Methyl Methacrylate1. *Macromolecules* **1997**, *30* (8), 2249-2253.

(44) Duquesne, E.; Degée, P.; Habimana, J.; Dubois, P. Supported nickel bromide catalyst for Atom Transfer Radical Polymerization (ATRP) of methyl methacrylate. *Chem. Commun.* **2004**, (6), 640-641.

(45) Granel, C.; Dubois, P.; Jérôme, R.; Teyssié, P. Controlled Radical Polymerization of Methacrylic Monomers in the Presence of a Bis(ortho-chelated) Arylnickel(II) Complex and Different Activated Alkyl Halides. *Macromolecules* **1996**, *29* (27), 8576-8582.

(46) Uegaki, H.; Kotani, Y.; Kamigaito, M.; Sawamoto, M. $NiBr_2(Pn\text{-}Bu_3)_2$ Mediated Living Radical Polymerization of Methacrylates and Acrylates and Their Block or Random Copolymerizations. *Macromolecules* **1998**, *31* (20), 6756-6761.

(47) Yang, L.; Powell, D. R.; Houser, R. P. Structural variation in copper(I) complexes with pyridylmethylamide ligands: structural analysis with a new four-coordinate geometry index, τ_4. *Dalton Trans.* **2007**, (9), 955-964.

(48) Chávez, I.; Alvarez-Carena, A.; Molins, E.; Roig, A.; Maniukiewicz, W.; Arancibia, A.; Arancibia, V.; Brand, H.; Manuel Manríquez, J. Selective oxidants for organometallic compounds containing a stabilising anion of highly reactive cations: $(3,5(CF_3)_2C_6H_3)_4B^-)Cp_2Fe^+$ and $(3,5(CF_3)_2C_6H_3)_4B^-)Cp^*_2Fe^+$. *J. Organomet. Chem.* **2000**, *601* (1), 126-132.

(49) Evans, D. F. The determination of the paramagnetic susceptibility of substances in solution by nuclear magnetic resonance. *J. Chem. Soc.* **1959**, (0), 2003-2005.

(50) Shen, Y.; Shepard, S. M.; Reed, C. J.; Diaconescu, P. L. Zirconium Complexes Supported by a Ferrocene-Based Ligand as Redox Switches for Hydroamination Reactions. *Chem. Commun.* **2019**, *55*, 5587-5590.

(51) Matyjaszewski, K.; Jo, S. M.; Paik, H.-j.; Shipp, D. A. An Investigation into the CuX/2,2‘-Bipyridine (X = Br or Cl) Mediated Atom Transfer Radical Polymerization of Acrylonitrile. *Macromolecules* **1999**, *32* (20), 6431-6438.

(52) Percec, B. B. a. V. Metal Catalyzed Living Radical Polymerization of Acrylonitrile Initiated with Sulfonyl Chlorides. *Macromolecules* **2001**, *34*, 8626-8636.

(53) Stejskal, E. O.; Tanner, J. E. Spin Diffusion Measurements: Spin Echoes in the Presence of a Time-Dependent Field Gradient. *J. Chem. Phys.* **1965**, *42* (1), 288-292.

(54) Jianying, H.; Jiayan, C.; Jiaming, Z.; Yihong, C.; Lizong, D.; Yousi, Z. Some monomer reactivity ratios of styrene and (meth)acrylates in the presence of TEMPO. *J. Appl. Polym. Sci.* **2006**, *100* (5), 3531-3535.

(55) Butz, S.; Hillermann, J.; Schmidt-Naake, G.; Kressler, J.; Thomann, R.; Heck, B.; Stühn, B. Synthesis and microphase separation of diblock copolymers of styrene and p-chlorostyrene prepared by using N-oxyl capped macroinitiators. *Acta Polym.* **1998**, *49* (12), 693-699.

(56) Shima, M.; Yamaguchi, N.; Sato, M.; Ogawa, E. Dipole moments of (styrene-p-chlorostyrene) triblock copolymers in solutions. *Eur. Polym. J.* **1983**, *19* (7), 601-604.

(57) De Bon, F.; Fantin, M.; Isse, A. A.; Gennaro, A. Electrochemically mediated ATRP in ionic liquids: controlled polymerization of methyl acrylate in [BMIm][OTf]. *Polym. Chem.* **2018**, *9* (5), 646-655.

(58) Chmielarz, P.; Krys, P.; Park, S.; Matyjaszewski, K. PEO-b-PNIPAM copolymers via SARA ATRP and eATRP in aqueous media. *Polymer* **2015**, *71*, 143-147.

(59) Chmielarz, P.; Park, S.; Simakova, A.; Matyjaszewski, K. Electrochemically mediated ATRP of acrylamides in water. *Polymer* **2015**, *60*, 302-307.

(60) Park, S.; Cho, H. Y.; Wegner, K. B.; Burdynska, J.; Magenau, A. J. D.; Paik, H.-J.; Jurga, S.; Matyjaszewski, K. Star Synthesis Using Macroinitiators via Electrochemically Mediated Atom Transfer Radical Polymerization. *Macromolecules* **2013**, *46* (15), 5856-5860.

(61) Amy B. Pangborn, M. A. G., Robert H. Grubbs, Robert K. Rosen, and Francis J. Timmers. Safe and Convenient Procedure for Solvent Purification. *Organometallics* **1996**, *15*, 1518-1520.

Chapter 3. Misadventures in scandium chemistry

3.1 Introduction

The activity of organometallic compounds in the ring opening polymerization (ROP) of various monomers offers a practical lens to characterize their reactivity through. Over the years, our group has amassed a library of compounds shown to be active in the redox switchable ROP of various cyclic esters and ethers.[1-7] Recently, Lai and coworkers ran density functional theory (DFT) calculations relevant to ROP by varying the metals, donors, linkers, and substituents in both accessible ferrocene oxidation states (Figure 3.1), and they generated structure activity relationships using principal component analysis (PCA).[8] PCA takes a data set – such as descriptors generated by DFT – and transforms them into a set of orthogonal variables, also known as components.[9] In short, PCA is able to decompose a multivariate data set into the two variables that have the greatest level of variability. When visualized, compounds with similar structural properties will be grouped together on the resulting plot.

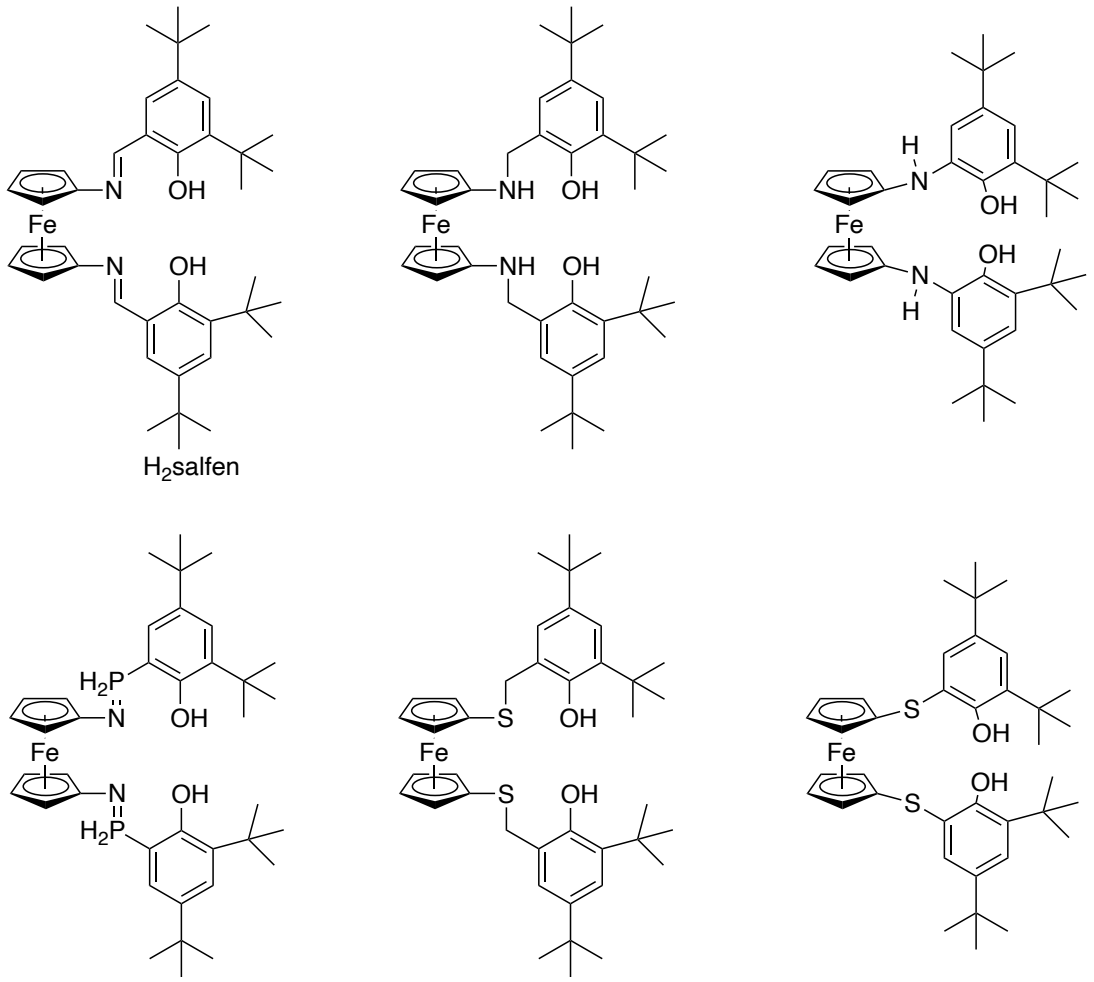

Figure 3.1 Scope of proligands studied by PCA. H_2salfen, the focus of this chapter, is labeled in the top left corner.[8]

From a structural analysis viewpoint, it was noted that the oxidized and reduced versions of the precatalysts typically map very closely to each other in PCA plots (Figure 3.2), but those with different ligand frameworks do not.[8] This implies that modifying the ferrocene oxidation state does not result in as impactful changes in the underlying structure as modifying ligand architecture does.

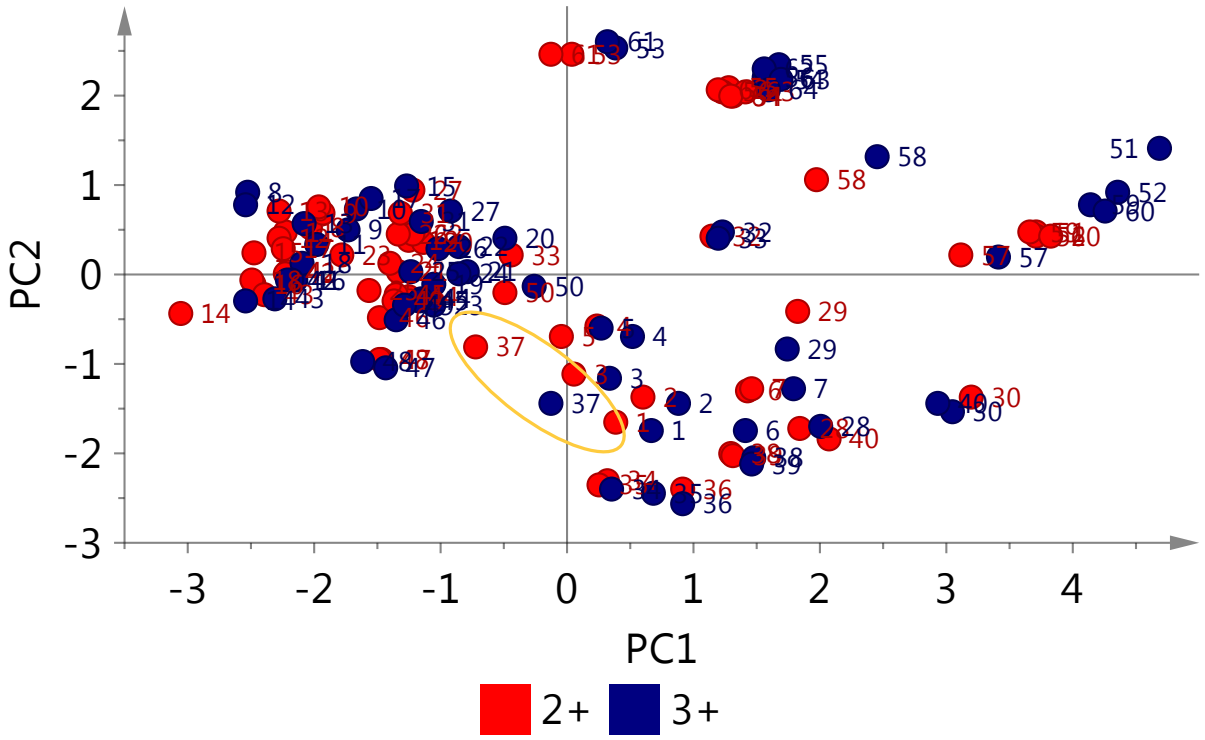

Figure 3.2 PCA plot for various ferrocene-based ligand frameworks coordinating different metals treating each oxidation state as a different entry oxidation states of ferrocene. The circled 37 is the (salfen)Sc compound at the focus of this chapter. Reprinted with minor modifications from Lai, A.; Clifton, J.; Diaconescu, P. L.; Fey, N. Computational mapping of redox-switchable metal complexes based on ferrocene derivatives. *Chem. Commun.* **2019**, *55* (49), 7021-7024, with permission from the Royal Society of Chemistry.

However, upon closer examination, the scandium versions of the compounds did not map nearly as closely as other metal centers did, suggesting oxidation states play a larger role in the scandium compounds than the other metal centers we've tested in ROP. In turn, this may give access to an unstudied area in the chemical space these precatalysts occupy. Therefore, I set out to synthesize the scandium versions of some these mapped compounds in order to ascertain why this difference exists and what effects it might have on their reactivity in ROP.

3.2 Synthetic strategies

3.2.1 Proligand synthesis

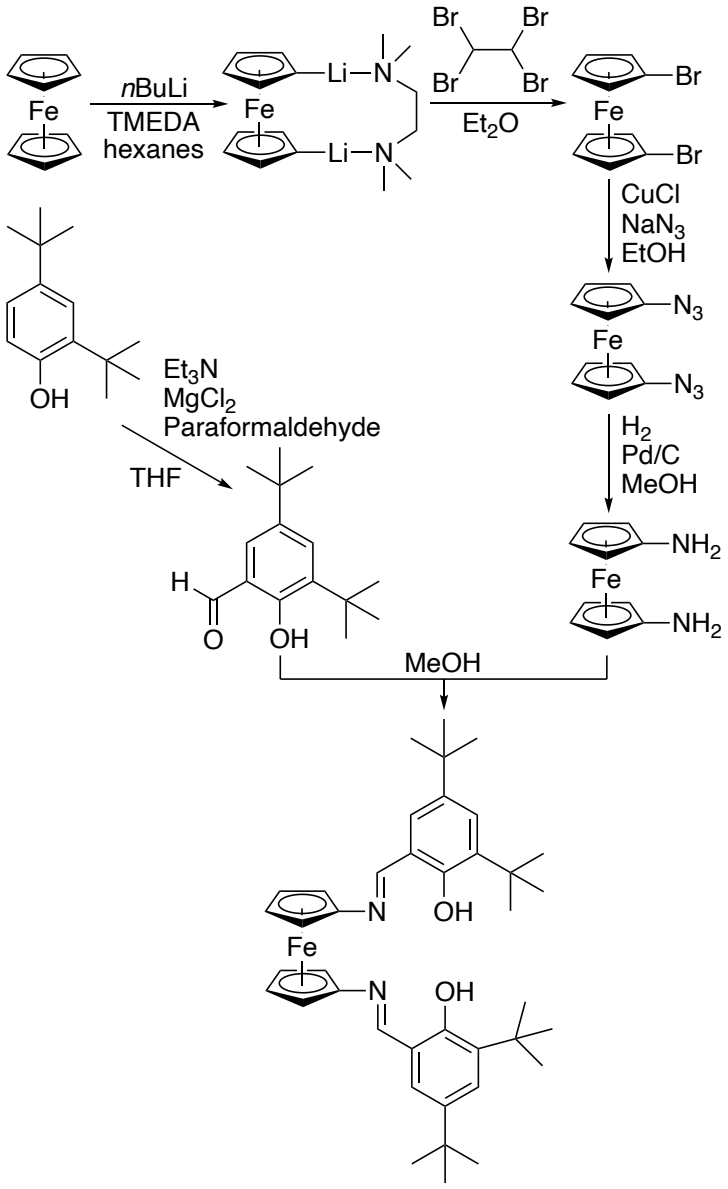

Figure 3.3 Synthetic route to H_2salfen.[10]

H_2salfen (salfen = 1,1'-bis(2,4-di-*tert*-butyl-6-salicylimine)ferrocene) is prepared in 5 synthetic steps starting from ferrocene (Figure 3.3). Ferrocene is lithiated with *n*BuLi in hexanes in a symmetric 1,1' fashion and stabilized with a tetramethylethylenediamine (TMEDA) chelate.[10] After 16 hours the resulting orange precipitate is filtered and washed with cold hexanes to obtain

$fc(Li)_2(TMEDA)$ in approximately 80% yield. The dilithioferrocene is then brominated, so it is robust enough to undergo further modifiactions. $fc(Li)_2(TMEDA)$ is reacted with 1,1,2,2-tetrabromoethane at -78°C in ether for 2 hours and allowed to stir to room temperature overnight. After quenching with water and extraction into ether, the resulting oil is crystalized from methanol to obtain 1,1'-dibromoferrocene. Dibromo ferrocene is then reacted with CuCl and NaN_3 in ethanol at room temperature with protection from light for two days. Quenching with water, extraction into hexane, and recrystallization from pentane affords 1,1'-diazidoferrocene as a light-sensitive solid. This is then converted into 1,1'-diaminoferrocene upon hydrogenation in methanol with Pd/C overnight. Filtration of the Pd/C and removal of MeOH under reduced pressure affords the desired product.

3,5-di-*tert*-butyl-2-hydroxybenzaldehyde was prepared by adding paraformaldehyde to a THF solution of 2,4-di-*tert*-butyl-phenol, triethylamine, $MgCl_2$ and refluxing at 80°C overnight. The solution is quench with a 5% HCl solution, extracted into ethyl acetate, and solvent is removed under reduced pressure to yield a yellow oil. Purification by column chromatography using hexanes as the eluent affords the product as a pale-yellow solid.[11]

Salfen is then prepared by dropwise addition of a MeOH solution of 1,1'-diaminoferrocene to a MeOH solution of 3,5-di-*tert*-butyl-2-hydroxybenzaldehyde.[12] After stirring overnight, the precipitate is collected on a frit and washed several times with methanol to afford H_2salfen as a red powder.

3.2.2 Salt metathesis route

Yttrium and scandium are both group 3 rare earth metals, and as such are expected to have relatively similar chemical properties. We had previously published on the yttrium versions of some of these compounds, so the first synthetic approaches started analogously to that of yttrium.[13]

Sc_2O_3 was converted to $ScCl_3$ via NH_4Cl sublimation.[14] Then the THF adduct was made by heating $ScCl_3$ in THF for 3 hours at 70°C in a sealed Schlenk tube to form $ScCl_3THF_{1.8}$.

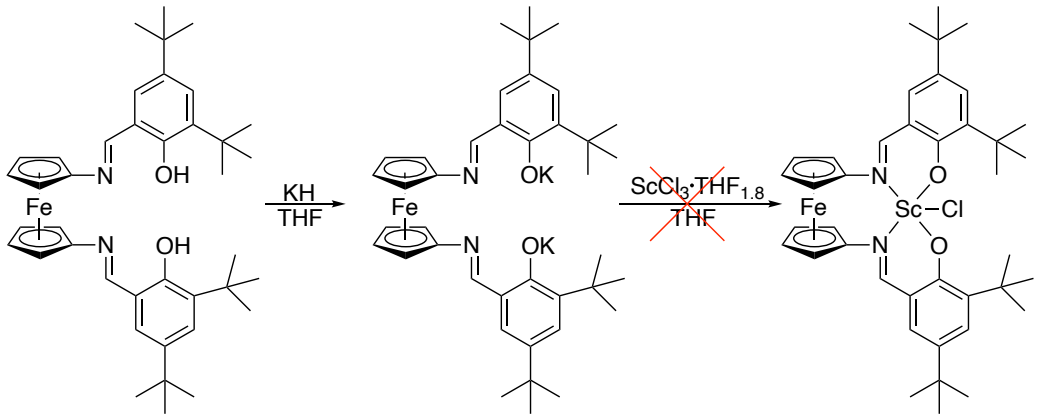

Figure 3.4 Failed salt metathesis leading to proligand decomposition.

From there, salt metathesis was attempted for the ligation step (Figure 3.4). A KH slurry in THF was added dropwise to a stirring solution of H_2salfen in THF. After 2 hours the reaction is filter through glass fiber and the resulting solution is added dropwise to a stirring suspension of $ScCl_3THF_{1.8}$ in THF at room temperature. After an additional three hours, the solution was filtered through glass fiber, and solvent was removed under reduced pressure to afford a red oil. Attempts to crystalize from a toluene solution layered with hexanes were unsuccessful.

Unfortunately, results varied quite drastically from the yttrium synthesis. Although conversion of the proligand was observed via NMR, the reaction was quite messy. As it turns out, scandium is not yttrium. Another approach would have to be taken to access the compounds of interest.

3.2.3 Benzyl elimination

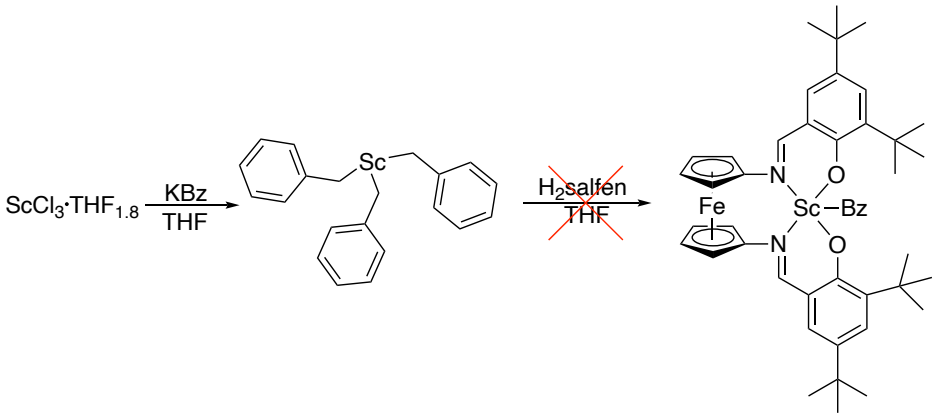

Figure 3.5 Failed benzyl elimination leading to proligand decomposition.

Our group has historically used benzyl elimination reactions to access scandium complexes (Figure 3.5).[14] Potassium benzyl is synthesized by adding *n*BuLi dropwise to a suspension of potassium *tert*-butoxide in toluene at 0°C. After stirring to room temp over 1 hour, the bright orange precipitate is filtered and washed with toluene followed by hexanes and dried under vacuum. Scandium tribenzyl is then generated *in situ* by adding a THF solution of potassium benzyl to a THF solution of $ScCl_3THF_{1.8}$ at -78°C. The solution was then allowed to stir to 0°C for 30 minutes before filtering through celite and washing with THF. The filtrate was then cooled back down to -78°C and a THF solution of H_2salfen was added dropwise and stirred for 30 minutes. Volatiles were removed under reduced pressure to yield a red oil. Attempts to recrystallize from toluene layered with hexanes were unsuccessful.

3.2.4 Extended silylamide route

All examples of scandium salen compounds in literature exclusively go through the amine elimination acid-base reaction.[15-18] Lithium tetramethyldisilazane (LTMDS) was prepared by adding *n*BuLi dropwise to a hexane solution of tetramethyldisilazane at room temperature. The

reaction was stirred overnight before solvent was removed under reduced pressure, and LTMDS was crystalized from a hexanes solution (Figure 3.6).

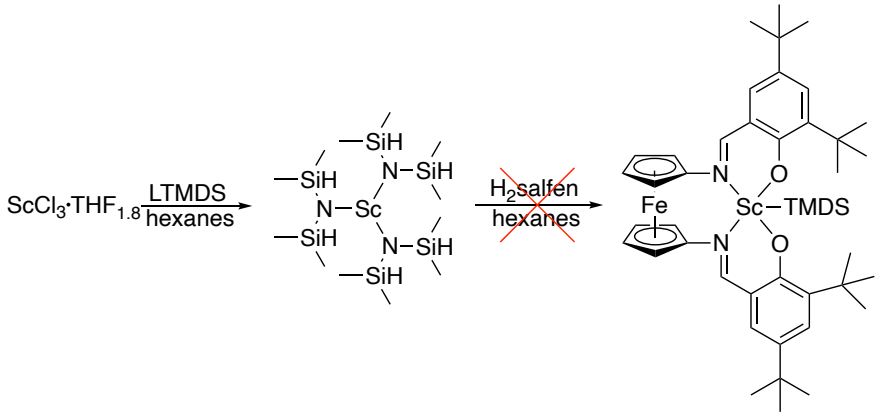

Figure 3.6 Failed silylamide elimination leading to proligand decomposition.

LTMDS powder was slowly added to a suspension of $ScCl_3THF_{1.8}$ in hexanes at room temperature and the reaction was stirred overnight. The precipitated LiCl was removed over Celite, and the solvent was removed under reduced pressure. Crystallization from hexanes yielded $Sc(TMDS)_3THF$ as thin needles.

The ligation of H_2Salfen to $Sc(TMDS)_3THF$ was attempted by dropwise addition of a THF solution of H_2Salfen to a hexanes solution of $Sc(TMDS)_3THF$ with vigorous stirring. However, attempts to isolate the desired (salfen)Sc(TMDS) were unsuccessful.

3.2.5 Diisopropylamine

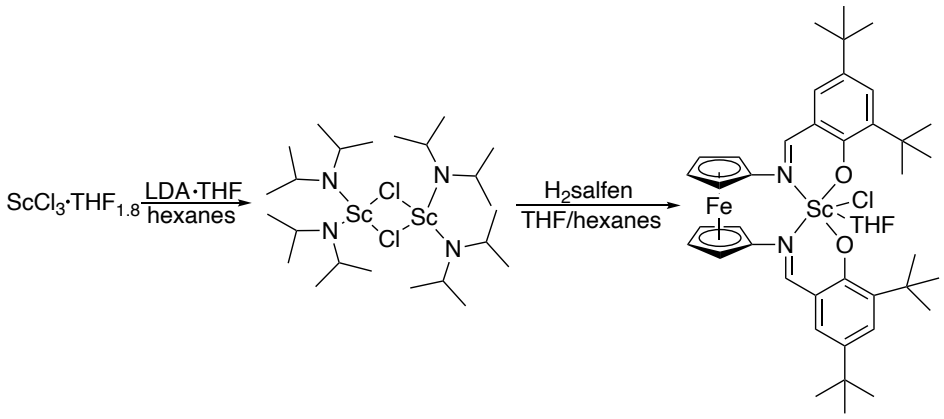

Figure 3.6 Successful diisopropylamine elimination leading to (salfen)ScCl(THF).

Scandium amide complexes with diisopropylamine (DIPA) are well studied and offered one last avenue to attempt (Figure 3.6).[19] LDA·THF is freshly prepared by adding *n*BuLi in hexanes dropwise to a solution of DIPA in THF at -78°C. The reaction is stirred for 40 minutes before removal of residual THF and hexanes under reduced pressure. Complete removal of ~15mL of the THF/hexanes mixture typically takes around 4 hours and the LDA undergoes a yellow oil stage before being dried to give a white powder in quantitative yields. $ScCl_3THF_{1.8}$ is then suspended in 10mL hexanes at room temp and the fresh LDA is added portion-wise in substoichiometric amounts. After stirring for 18 hours at room temp, the LiCl formed is allowed to settle, and the solution is decanted and filtered through celite. Solvent is removed *in vacuo*, and the resultant yellow oil is extracted into hexanes. This process is repeated twice to ensure removal of any residual LiCl. Depending on the stoichiometry of LDA employed various scandium amide complexes can be formed, but most often I used 1.9 equivalents to yield $Sc[(DIPA)_2(THF)(\mu\text{-}Cl)]_2$.

Then a THF of solution of H_2salfen was added dropwise to a hexanes solution of $Sc[(DIPA)_2(THF)(\mu\text{-}Cl)]_2$ and allowed to stir overnight at room temperature. After removal of

solvent *in vacuo* and trituration with toluene, recrystallization of the red oil from THF layer with hexanes yields (salfen)ScCl(THF) as thin orange needles.

3.3 Conclusions and future directions

Attempts to make the desired alkoxides from the scandium chloride were unfortunately unsuccessful. While this prohibited the study from reaching any sort of satisfying conclusion, I was more than happy to at least achieve a clean compound after months of trying. A potential route to form the alkoxide that I suspect might work is treating the reaction like the formation of $Sc[(DIPA)_2(THF)(\mu\text{-}Cl)]_2$. The formation of the scandium amide works because both LDA and $ScCl_3THF_{1.8}$ are insoluble in hexanes, so the reaction is slowed down by diffusion limitations. This slow reaction is necessary to prevent formation of the "-ate" compounds. Therefore, the salt metathesis reaction to form the scandium alkoxides using $Sc[(DIPA)_2(THF)(\mu\text{-}Cl)]_2$ will likely need to apply the same principles. Often, I tried dropwise addition of potassium alkoxides to $[Sc(DIPA)_2(THF)(\mu\text{-}Cl)]_2$ at -78°C in Et_2O. Then the reaction is stirred to room temp over the course of 1 hour before filtering through Celite and removal of residual solvent. The reaction is likely too fast at room temperature and destroys the compound. However, at -78°C both solutions are actually suspensions as their constituents are fairly insoluble at that temperature, so diffusion limitation can likely be leveraged here with prolonged stirring of the reaction mixture at -78°C. Overall, this scandium project was a good exercise in discipline in organometallic synthesis.

3.4 Experimental

General considerations. All experiments were performed under a dry nitrogen atmosphere in an MBraun glovebox or using standard Schlenk techniques unless otherwise stated. Solvents were purified with a two-state solid-state purification system by the method of Grubbs[20] and transferred into a glovebox without exposure to air. NMR solvents were purchased from Cambridge Isotope

Laboratories, degassed, and stored over activated molecular sieves prior to use. ^{1}H NMR spectra were recorded on Bruker AV-300, Bruker AV-500, or Bruker AV-600 spectrometers at room temperature. Chemical shifts are reported with respect to the residual solvent peaks, 7.16 ppm (C_6D_6), 7.26 ppm ($CDCl_3$) for ^{1}H NMR spectra, 128.06 (C_6D_6) for ^{13}C NMR spectra. *n*-BuLi, 2,4-di-*tert*-butylphenol, Sc_2O_3 were purchased from Sigma-Aldrich and used as received.

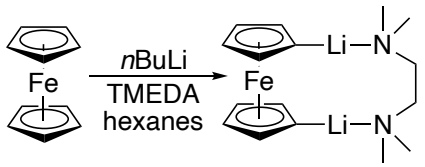

Synthesis of 1,1'-dilithioferrocene·TMEDA. Ferrocene (10 g, 53 mmol) was dissolved in 100 mL hexanes in a 500 mL round bottom flask inside the glovebox followed by TMEDA (7.50 g, 64 mmol). An addition funnel was charged with *n*BuLi (2.5 M, 47.3 mL, 117 mmol) and added dropwise over 30 minutes. The reaction was stirred for overnight at room temperature, and the precipitate was collected on a frit. The resulting orange solid was collected after washing with hexanes and dried under a reduced pressure (14.12 g, 83.8%).

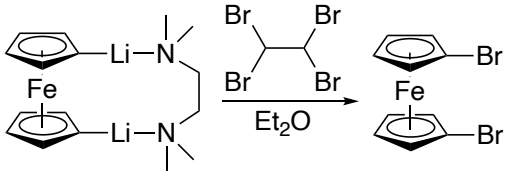

Synthesis of 1,1'-dibromoferrocene. 1,1'-dilithioferrocene·TMEDA (8.01 g, 26 mmol) was dissolved in Et_2O in the glovebox. An ethereal solution of 1,1,2,2-tetrabromoethane (TBE) (19.41 g, 56 mmol) is added to an addition funnel and the entire apparatus is cooled to -78°C with stirring for 1 hour. The TBE solution is added dropwise to the stirring ferrocene solution over 30 minutes, and the reaction is allowed to slowly warm to room temperature with stirring overnight. The next

day, the reaction is quenched with 75 mL H_2O and allowed to stir for 30 minutes, before extracting into Et_2O. The extracts are combined, dried with $MgSO_4$, decanted, and solvent is removed under reduced pressure. Recrystallization from MeOH at -35°C yields 1,1'-dibromoferrocene as a red crystalline solid (4.22 g, 59%). ^{1}H NMR (400 MHz, 298K, $CDCl_3$) δ (ppm): 4.42 (t, 4H, Cp-H), 4.17 (t, 4H, Cp-H).

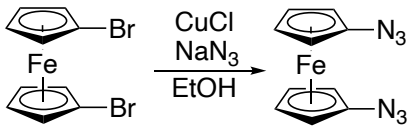

Synthesis of 1,1'-diazidoferrocene. 1,1'-dibromoferrocene (7.02 g, 20 mmol) is dissolved in 80 mL EtOH in air. In the dark, CuCl (4.24 g, 43 mmol) is added to the stirring 1,1'-dibromoferrocene solution. NaN_3 (5.31 g, 81 mmol) is dissolved in 20 mL H_2O and added to the reaction mixture and stirred for 48 hours with protection from light. 150 mL H_2O is added, and the reaction allowed to stir for an additional 30 minutes. The reaction is extracted into hexanes, dried with $MgSO_4$, decanted, and solvent is removed under reduced pressure. Recrystallization from pentane at -35°C affords the product as a light sensitive solid (3.58 g, 65%). ^{1}H NMR (300 MHz, 298K, $CDCl_3$) δ (ppm): 4.35 (t, 4H, Cp-H), 4.15 (t, 4H, Cp-H).

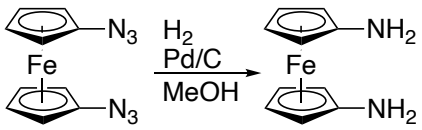

Synthesis of 1,1'-diaminoferrocene. In the glovebox, 1,1'-diazidoferrocene (1.0 g, 3.7 mmol) and Pd/C (0.2 g, 1.9 mmol) are placed into a Teflon capped Schlenk flask and suspended in 20 mL of MeOH. N_2 is evacuated from the flask and H_2 is introduced (~1 atm). The flask is cycled like

this three more times before allowing to stir for 1 hour. The flask is cycled again and allowed to stir for 1 hour. Then the flask is cycled one more time before allowing to stir overnight in a H_2 atmosphere. The next day, the flask is cycled one more time and allowed to stir for 3 hours before transferring back to the glovebox. The Pd/C is collected on a frit, and residual solvent is removed from the filtrate under reduced pressure to afford 1,1'-diaminoferrocene in quantitative yield (0.81 g, 3.7 mmol). ^{1}H NMR (300 MHz, 298K, C_6D_6) δ (ppm): 3.74 (t, 4H, Cp-H), 3.65 (t, 4H, Cp-H), 1.86 (br s, 4H, NH_2).

Synthesis of 3,5-di-*tert*-butyl-2-hydroxybenzaldehyde. 2,4-di-*tert*-butyl-phenol (5.16 g, 25 mmol), Et_3N (5.1 g, 48 mmol), and $MgCl_2$ (4.8 g, 50 mmol) are added to 80 mL dry THF and stirred for 30 minutes under N_2. Paraformaldehyde (3.0 g, 100 mmol) is added, and the solution is refluxed at 80°C overnight before cooling to room temperature. The solution is quenched with a 5% v/v HCl solution and extracted into ethyl acetate. Solvent is removed under rotary evaporation and the yellow oil is taken up into CH_2Cl_2 and washed with a 12M NaOH solution. The CH_2Cl_2 layer is treated with several drops of concentrated HCl until yellow, and the organic layer is collected. Drying over $MgSO_4$ and removal of solvent under reduced pressure affords a pale-yellow solid that can be further purified by flash chromatography with hexanes if necessary (3.17 g, 54%). ^{1}H NMR (300 MHz, 298K, $CDCl_3$). δ (ppm): 11.64 (s, 1H, OH), 9.87 (s, 1H, N=CH), 7.60 (d, 1H, Ar-H), 7.34 (d, 1H, Ar-H), 1.84 (s, 9H, CCH_3), 1.34 (s, 9H, CCH_3).

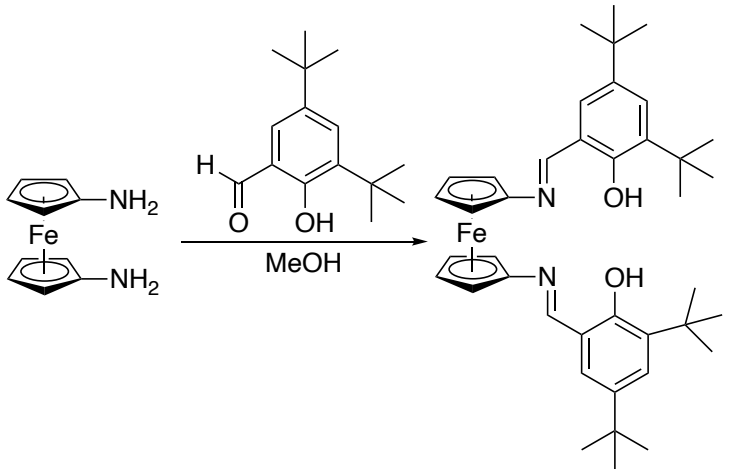

Synthesis of 2,4-di-*tert*-butyl-salicyl-1,1'-ferrocene-diimine, H2salfen. To a methanol (7 mL) solution of fc(NH3)2 (0.76 g, 3.6 mmol), a methanol (8 mL) solution of 3,5-di-*tert*-butyl-2-hydroxybenzaldehyde (1.64 g, 7.2 mmol) was added drop-wise. The dark-red solution was allowed to stir overnight. The resulting mixture was passed through a fritted filter and washed several times with methanol. After the volatiles were removed under reduced pressure, a red powder was obtained. Yield: 2.50 g, 100%. ^{1}H NMR (300 MHz, 298K, C_6D_6) δ (ppm): 14.16 (s, 2H, OH), 8.36 (s, 2H, N=CH), 7.762(d, 2H, Ar-H), 7.07 (d, 2H, Ar-H), 4.24 (br s, 4H, Cp-H), 3.94 (br s, 4H, Cp-H), 1.68 (s, 18H, CCH_3), 1.34 (s, 18H, CCH_3).

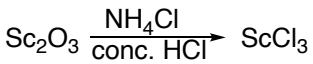

Synthesis of $ScCl_3$. Sc_2O_3 (5 g, 36 mmol) and NH_4Cl are combined in a 1 L Erlenmeyer flask and dissolved in 240 mL of 4:3 H_2O : concentrated HCl. This mixture is stirred at 105°C with a stream of air directed over the top until a semi-wet solid is obtained. This solid is transferred to the bottom of an oil bubbler trap 30 cm in length with a stop cock and heated in a tube furnace under dynamic

vacuum at 413K, 523K, and 633K for 24 hours each. Once the tube has cooled it is immediately transferred into the glove box and the off-white solid at the bottom of the tube is collected (7.4 g, 67%).

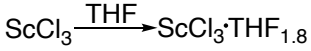

Synthesis of $ScCl_3THF_{1.8}$. $ScCl_3$ (4 g, 27 mmol) is suspended in 10 mL dry THF in a Teflon capped Schlenk tube at 55°C for 3 hours. Removal of residual THF affords the THF adduct as an off-white solid in quantitative yields (5.95 g, 100%).

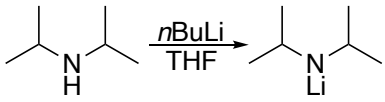

Synthesis of lithium diisopropylamine. To a solution of diisopropylamine (2 g, 19.8 mmol) in 10 mL THF, *n*BuLi (2.5 M in hexanes, 7.9 mL, 19.8 mmol) is added dropwise at -78°C. After 40 minutes, to afford LDA·THF as a white solid in quantitative yield (3.54 g, 100%).

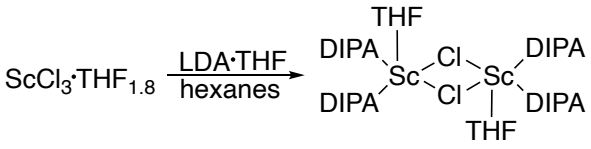

Synthesis of [Sc(DIPA)$_2$(THF)(μ-Cl)]$_2$.[19] $ScCl_3THF_{1.8}$ (1.07 g, 3.8 mmol) is suspended in 5 mL dry hexanes with vigorous stirring. LDA·THF (1.34 g, 7.4 mmol) is added portion wise, and the reaction is allowed to stir at room temperature overnight. The next day, stirring is halted and the suspension is allowed to settle before decanting and filtering through Celite. Solvent is removed *in vacuo* and the yellow oil is extracted twice more with hexanes. After removal of solvent for the final time, the yellow oil was layered with hexanes and the product crystalized at -35°C as a white solid (0.52 g, 39%). ^{1}H NMR (300 MHz, 298K, C_6D_6) spectrum of [Sc(DIPA)$_2$(THF)(μ-Cl)]$_2$. δ (ppm): 3.77 (m, 8H, OC*H*$_2$CH$_2$), 3.67 (s, 8H, C*H*(CH$_3$)$_2$), 1.38 (d, 48H, CH(C*H*$_3$)$_2$), 1.24 (m, 8H, OCH$_2$C*H*$_2$).

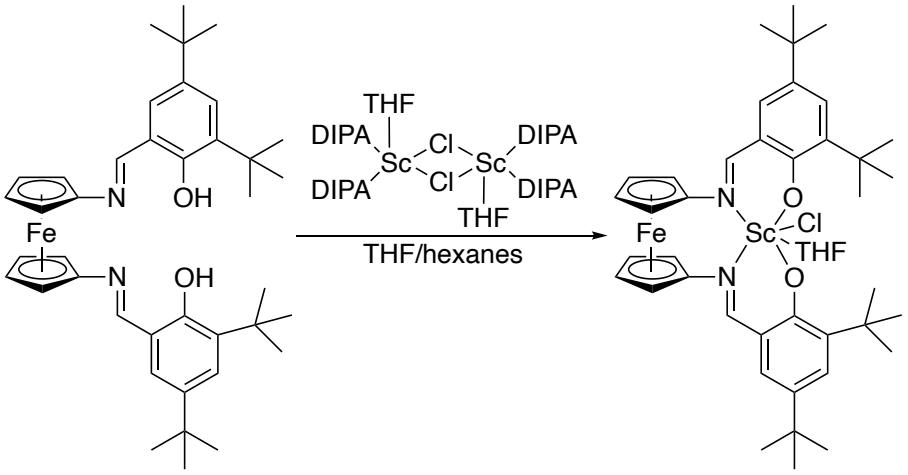

Synthesis of (salfen)ScCl(THF). A solution of H$_2$salfen (205 mg, 0.32 mmol) in THF is added dropwise to a solution of **[**Sc(DIPA)$_2$(THF)(μ-Cl)]$_2$ (112 mg, 0.16 mmol) in hexanes. The reaction is allowed to stir overnight at room temperature before solvent is removed *in vacuo*. The resulting powder is triturated twice with toluene. The powder is then redissolved in THF and layered with hexanes at -35°C overnight to afford (salfen)ScCl(THF) as orange needles (202 mg, 80%). ^{1}H

NMR (600 MHz, 298K, C_6D_6) δ (ppm): 8.03 (broad s, 2H, N=CH), 7.79 (broad s, 2H, Ar-H), 7.02 (broad s, 2H, ArH), 5.12, 3.99, 3.94 and 3.83 (broad s, 8H, Cp-H), 3.57 (broad s, 4H, OCH_2), 1.84 (broad s, 18H, CCH_3), 1.34 (broad s, 18H, CCH_3), 1.16 (broad s, 4H, CH_2CH_3O). ^{13}C-NMR (125 MHz, 298K, C_6D_6) δ (ppm): 172.72 (N=C), 164.42 (OC_6H_2), 139.29 (OC_6H_2), 138.14 (OC_6H_2), 131.03 (OC_6H_2), 130.03 (OC_6H_2), 122.99 (OC_6H_2), 110.76 (N-C), 69.17-66.97 (C_5H_4), 63.34 (OCH_2CH_2), 36.14 ($C(CH_3)_3$), 34.21 ($C(CH_3)_3$), 31.70 ($C(CH_3)_3$), 30.40 ($C(CH_3)_3$), 25.58 (OCH_2CH_2).

3.5 References

(1) Xu, X.; Luo, G.; Hou, Z.; Diaconescu, P. L.; Luo, Y. Theoretical insight into the redox-switchable activity of group 4 metal complexes for the ring-opening polymerization of ε-caprolactone. *Inorg. Chem. Front.* **2020**, *7* (4), 961-971.

(2) Lai, A.; Hern, Z. C.; Diaconescu, P. L. Switchable Ring-Opening Polymerization by a Ferrocene Supported Aluminum Complex. *ChemCatChem* **2019**, *11* (16), 4210-4218.

(3) Dai, R.; Diaconescu, P. L. Investigation of a zirconium compound for redox switchable ring opening polymerization. *Dalton Trans.* **2019**, *48* (9), 2996-3002.

(4) Abubekerov, M.; Wei, J.; Swartz, K. R.; Xie, Z.; Pei, Q.; Diaconescu, P. L. Preparation of multiblock copolymers via step-wise addition of l-lactide and trimethylene carbonate. *Chem. Sci.* **2018**, *9* (8), 2168-2178.

(5) Wei, J.; Riffel, M. N.; Diaconescu, P. L. Redox Control of Aluminum Ring-Opening Polymerization: A Combined Experimental and DFT Investigation. *Macromolecules* **2017**, *50* (5), 1847-1861.

(6) Quan, S. M.; Wei, J.; Diaconescu, P. L. Mechanistic Studies of Redox-Switchable Copolymerization of Lactide and Cyclohexene Oxide by a Zirconium Complex. *Organometallics* **2017**, *36* (22), 4451-4457.

(7) Lowe, M. Y.; Shu, S.; Quan, S. M.; Diaconescu, P. L. Investigation of redox switchable titanium and zirconium catalysts for the ring opening polymerization of cyclic esters and epoxides. *Inorg. Chem. Front.* **2017**, *4* (11), 1798-1805.

(8) Lai, A.; Clifton, J.; Diaconescu, P. L.; Fey, N. Computational mapping of redox-switchable metal complexes based on ferrocene derivatives. *Chem. Commun.* **2019**, *55* (49), 7021-7024.

(9) Sidou, L. S. F.; Borges, E. M. Teaching Principal Component Analysis Using a Free and Open Source Software Program and Exercises Applying PCA to Real-World Examples. *J. Chem. Educ.* **2020**, *97* (6), 1666-1676.

(10) Shafir, A.; Arnold, J. Stabilization of a Cationic Ti Center by a Ferrocene Moiety: A Remarkably Short Ti−Fe Interaction in the Diamide $\{[(\eta^5\text{-}C_5H_4NSiMe_3)_2Fe]TiCl\}_2^{2+}$. *J. Am. Chem. Soc.* **2001**, *123* (37), 9212-9213.

(11) Hansen, T. V.; Skattebøl, L. A high yielding one-pot method for the preparation of salen ligands. *Tetrahedron Lett.* **2005**, *46* (22), 3829-3830.

(12) Wang, X.; Thevenon, A.; Brosmer, J. L.; Yu, I.; Khan, S. I.; Mehrkhodavandi, P.; Diaconescu, P. L. Redox Control of Group 4 Metal Ring-Opening Polymerization Activity toward l-Lactide and ε-Caprolactone. *J. Am. Chem. Soc.* **2014**, *136* (32), 11264-11267.

(13) Deng, S.; Diaconescu, P. L. A switchable dimeric yttrium complex and its three catalytic states in ring opening polymerization. *Inorg. Chem. Front.* **2021**, *8* (8), 2088-2096.

(14) Carver, C. T.; Monreal, M. J.; Diaconescu, P. L. Scandium Alkyl Complexes Supported by a Ferrocene Diamide Ligand. *Organometallics* **2008**, *27* (3), 363-370.

(15) Meermann, C.; Sirsch, P.; Törnroos, K. W.; Anwander, R. Synthesis and structural characterization of scandium SALEN complexes. *Dalton Trans.* **2006**, (8), 1041-1050.

(16) Ma, H.; Spaniol, T. P.; Okuda, J. Highly Heteroselective Ring-Opening Polymerization ofrac-Lactide Initiated by Bis(phenolato)scandium Complexes. *Angew. Chem. Int. Ed.* **2006**, *45* (46), 7818-7821.

(17) Meermann, C.; Törnroos, K. W.; Anwander, R. Scandium SALEN Complexes Bearing Chloro, Aryloxo, and Hydroxo Ligands. *Inorg. Chem.* **2009**, *48* (6), 2561-2570.

(18) Anwander, R.; Runte, O.; Eppinger, J.; Gerstberger, G.; Herdtweck, E.; Spiegler, M. Synthesis and structural characterisation of rare-earth bis(dimethylsilyl)amides and their surface organometallic chemistry on mesoporous MCM-41†. *J. Chem. Soc., Dalton Trans.* **1998**, (5), 847-858.

(19) Spallek, T.; Heß, O.; Meermann-Zimmermann, M.; Meermann, C.; Klimpel, M. G.; Estler, F.; Schneider, D.; Scherer, W.; Tafipolsky, M.; Törnroos, K. W.; et al. Synthesis and structural diversity of trivalent rare-earth metal diisopropylamide complexes. *Dalton Trans.* **2016**, *45* (35), 13750-13765.

(20) Pangborn, A. B.; Giardello, M. A.; Grubbs, R. H.; Rosen, R. K.; Timmers, F. J. Safe and Convenient Procedure for Solvent Purification. *Organometallics* **1996**, *15* (5), 1518-1520.

Chapter 4. Slickwater chemistry - degradable friction reducers

4.1 Introduction

4.1.1 Hydraulic fracturing

Hydraulic fracturing techniques for stimulating oil-well production were first introduced in the 1860s when liquid and solidified nitroglycerin were used to stimulate shallow, hard rock wells.[1] At that time, nitroglycerin was detonated inside the well in order to break up the oil bearing formation to stimulate flow. However, this work was extremely hazardous, and by the 1930s, trials were going on for using pressurized acids to etch fractures and leave a flow channel instead. An in-depth study of this acid etching process by Floyd Farris – who was working for Standard Oil at the time – led to the conception of hydraulic fracturing for oil wells, instead of the environmentally damaging acid etching. A few years later in 1949, Joseph B. Clark formalized the methodology for hydraulic fracturing in his seminal work, coining the process "Hydrafrac".[2]

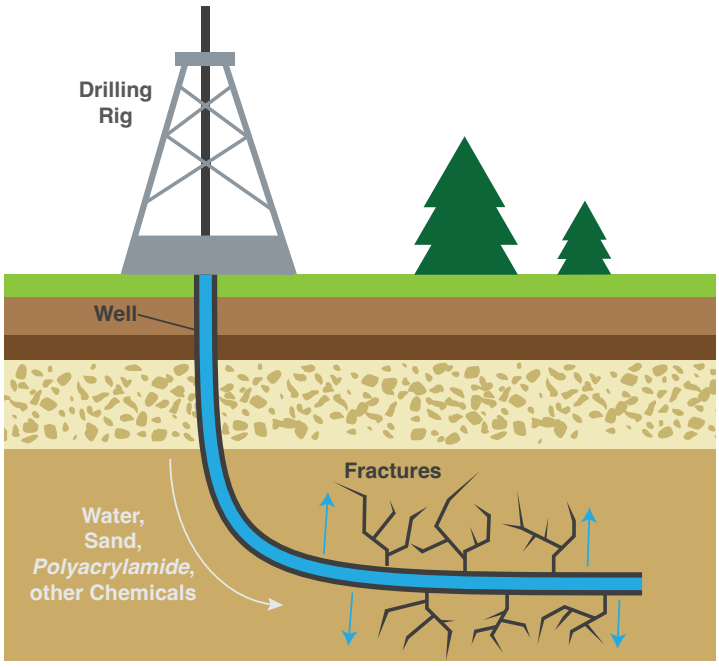

Figure 4.1 Schematic representation of hydraulic fracturing. Water, sand, friction reducers, and other chemicals are pumped into oil or gas rich layers of earth to create and maintain fractures.

Hydraulic fracturing consists of two main steps. The first step is to inject a viscous liquid containing a granular material (known as proppant, most often sand) into an oil bed under high hydraulic pressure (Figure 4.1).[2, 3] This causes the bed to fracture, and the viscous liquid to change from high to low viscosity. In the second stage this now non-viscous liquid is easily displaced from the oil bed. Hydraulic fracturing processes have greatly increased the productivity of oil wells[1] and have allowed access to new drilling locations not previously accessible such as coal beds and shale.[4, 5]

4.1.2 Friction reducers

Pumping proppant down a wellbore creates friction between the pipe wall and the fracking fluid.[6] Typical friction reducers are chemical compounds that can "slick-the-water" to minimize drag along the pipe wall while transporting proppant and thereby reduce surface treating pressures at the wellhead.[7, 8] Friction reducers are added to hydraulic fracturing fluid to reduce wear and tear on the pumps while still allowing proppant transport to occur at the high flow rates required (to 4200 gallons per minute), and they are the main chemical additives (most often polymers) used in Slickwater fluids.[7-9]

Physicists have spent an inordinate amount of time trying to elucidate the mechanism of friction reduction in high turbulent flow regimes. In 1833, Reynolds was the first to describe the transition from fluid moving in a steady linear pattern (laminar flow) to a dynamic and sinuous pattern (turbulent flow) as a function of increasing viscosity.[10] Dimensional analysis led to the conclusion that in any given flow set-up that transition from laminar to turbulent flow would occur at a single dimensionless quantity, later known as the Reynolds number.[10, 11] Polymer-induced friction reduction in high Reynolds number flows (i.e. highly turbulent flows) has been known since the 1940s, and was first observed by Toms using a small amount (10 wppm – weight parts

per million) of poly(methyl methacrylate) dissolved in monochlorobenzne.[12] Since the discovery of the friction reduction phenomenon, multiple models have been created to rationalize the fluid dynamics and polymer physics of these systems.[11]

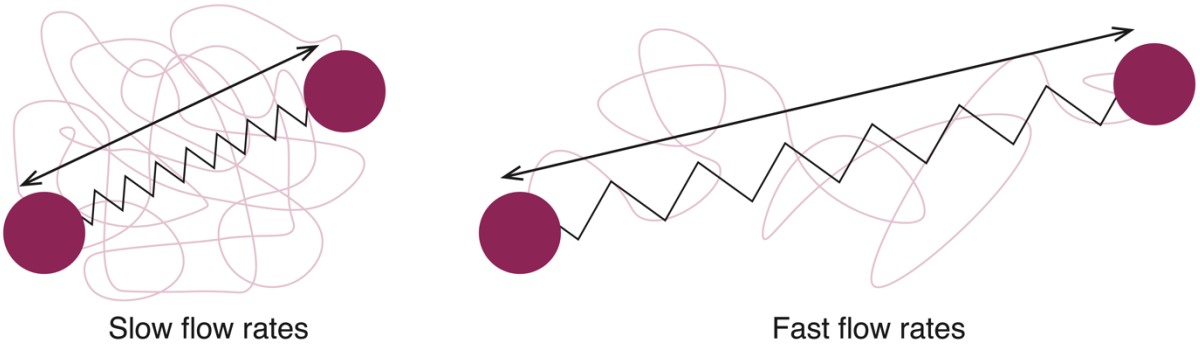

Figure 4.2 Representation of polymers as described by the finite extensible nonlinear elastic (FENE) model. At slow flow rates polymers exist as curled balls and at faster flow rates polymers exist as longer stretched out chains.

One of the more widely adopted theories to explain polymer behavior in dilute solutions is the finite extensible nonlinear elastic (FENE) model of a long-chained polymer (Figure 4.2).[11] Simplistically, a polymer chain can be modeled as a dumbbell. In a standing solution, the polymer takes its most entropically favored, coiled state. As the polymer is subject to more force, the ends of the dumbbell begin to stretch apart from each other. This stretching is mediated by some spring-force law, and it ultimately models the entropic resistance of the chain to stretching. Since the flow regimes used in hydraulic fracturing are extremely turbulent, most relevant models assume polymers to be at least partially elongated depending on the theory.

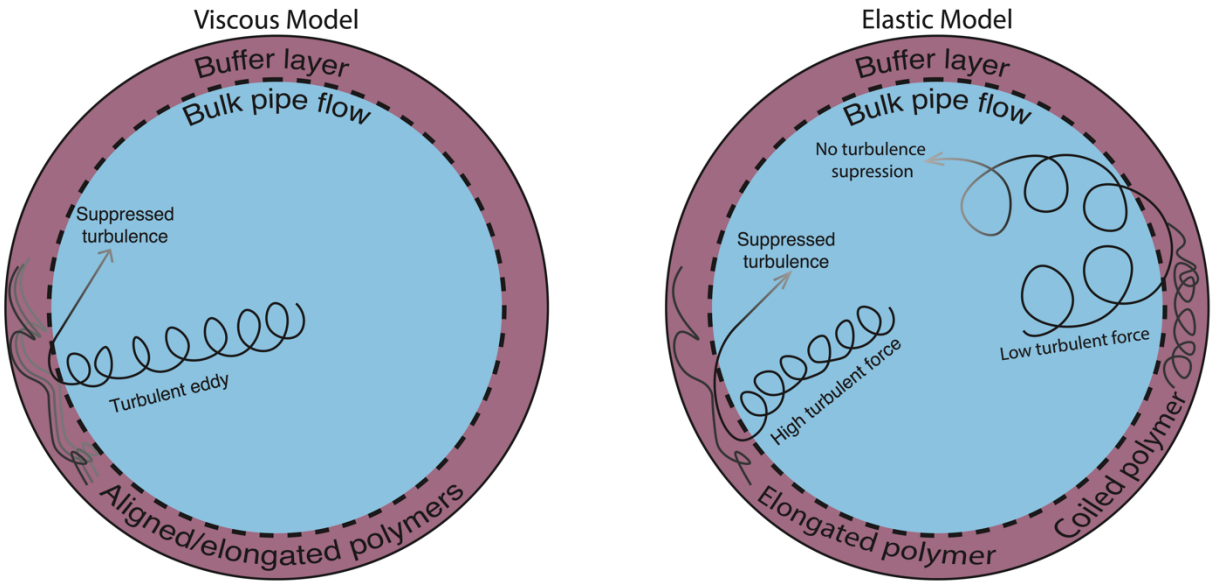

Figure 4.3 Cross-section of a pipe with friction reducers present.

Ultimately, to cause friction reduction, polymers have to suppress turbulent motion in the pipe (Figure 4.3).[11] Early experiments showed that drag reduction becomes substantial when polymers reach the near-wall regions of pipes.[13, 14] Because this reduction is different than the bulk pipe flow, it suggests the creation of a buffer layer between the pipe wall and the bulk fluid transport. There are historically two main theories of what happens at this buffer layer that translates into friction reduction. The viscous model, proposed by Lumley, states that strong extensional forces are created near vortices in turbulent flow.[15] Polymer molecules become elongated and locally aligned in the presence of the extensional forces. However, since this state is a highly entropically unfavorable, the polymers want to be coiled instead. This provides resistance to the extensional forces, and therefore, suppresses the overall turbulence of the flow. Essentially, a local increase in viscosity lessens the formation of eddies during turbulent flow. In contrast, the elastic model, first conceptualized by de Gennes and coworkers, does not assume a highly stretched polymer state.[16] Instead, the polymers are transiently elongated, and the elasticity is stored the in individual chains. When the elastic stress on the polymer is equal to or higher than

the Reynolds stress provided by the flow, drag reduction occurs to balance the forces. Unfortunately, while both the elastic and viscous models have found supporting evidence, they don't seem sufficient for an unequivocal conclusion.[11, 17] The current state of friction reduction mechanisms and the physics behind them have been reviewed recently by Xi, and the reader is directed there for a more in depth discussion.[11]

4.1.3 Polyacrylamide

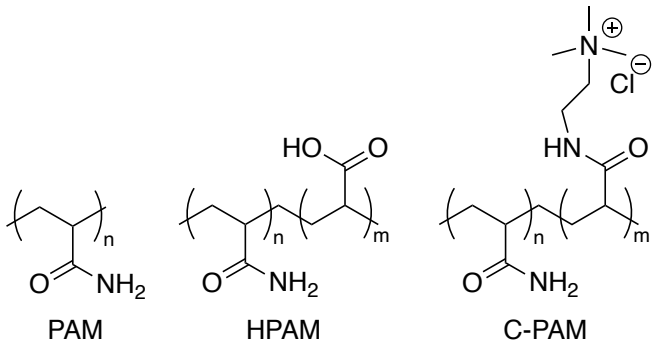

Figure 4.4 Drawing of PAM, HPAM, and C-PAM.

Friction reducers are the most widely used chemical additive in hydraulic fracturing.[8] Slickwater can normally contain 0.15% v/v friction reducer while the sum of other organic additives contributes less than 0.1% v/v.[18] Nowadays industry has shifted from gaur based friction reducers to polyacrylamide (PAM) based ones over volatility in the gaur market and concerns of biofouling (Figure 4.4).[19] Partially hydrolyzed PAM (HPAM) is a first generation PAM introduced in the 1970s for enhanced oil recovery processes. While still used today for Slickwater applications, the polymer is unstable in the presence of high total dissolved solids. Divalent calcium, Ca^{2+}, can cause undesirable crosslinking with the anionic charges in the polymer leading to inferior friction reduction capabilities.[20] For applications in high total dissolved solids environments, cationic polyacrylamide (C-PAM) that has pendant quaternary amines is used. Ester linkages in the side chains of these polymers are unstable and can easily hydrolyze in the presence

of low pH or >10ppm Fe^{2+}. Interestingly, current iterations of C-PAM have dealt with this hydrolysis issue by simply replacing the ester linkage with an amide.[20, 21]

While PAM itself is innocuous, its presence can potentially reduce the effectiveness of waste water treatments[22-25], and it can potentially decay into toxic monomers.[26] Most studies on PAM degradation in hydraulic fracturing are concerned with reduction in performance as a friction reducer due to a decreased molecular weight. [27, 28] However, these studies often fail to consider the end-of-life analysis for the (only partially) degraded PAM.[29] PAM will often degrade under the conditions necessary for hydraulic fracturing, reducing molecular weight by two orders of magnitude.[18] However, environmental conditions vary widely, and PAM requires high Fe^{2+} concentrations, acidic conditions, and elevated temperatures to induce thermal degradation. (As an aside: there is a historical distinction dating back to Muller in the 1980s in PAM degradation terminology.[28] Thermal degradation refers to cleavage of the hydrocarbon backbone and chemical degradation refers to hydrolyzing the pendant amides into carboxylic acids).[30, 31] Consequentially, some places such as Marcellus shale regions that operate in temperatures <50°C will not induce degradation of PAM.[18] Even in optimal conditions, the resulting molecular weight of degraded PAM can still be on the order of 10 MDa with resulting particle sizes of 350 nm for non-aggregated polymers. While the effects of nanoplastics on the environment are not as well studied as microplastics are, they certainly still pose an environmental concern.[32-34] Nanoparticles can readily agglomerate in water to form larger clusters, so it is naïve to assume that would not be the case in Slickwater fluids as well. Ultimately, there is a need for more fully degradable alternatives to polyacrylamide in Slickwater applications, and to continue the use of the current polymers could have drastic environmental consequences.

4.2 Results and discussion

4.2.1 Poly(ethylene glycol) quenching

While biodegradable, the polymers that our group has synthesized in the past decade are water insoluble. This obviously posits an issue considering friction reduction is run in various water brines. The main idea to try and rectify this problem was to quench polymerization reactions with a known water soluble polymer such as poly(ethylene glycol) (PEG) in order to impart some water solubility to the resulting polymers.

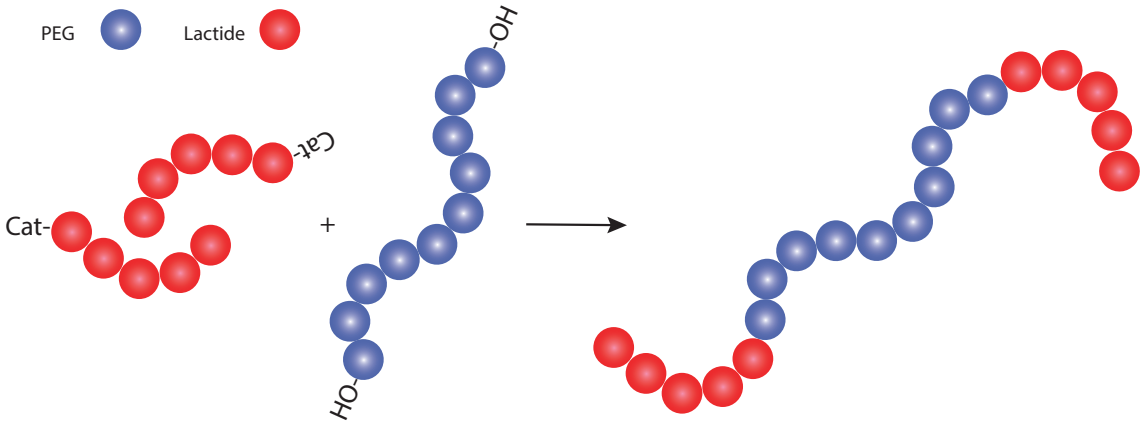

Figure 4.5 Schematic description of PEG-quenching experiments

As a proof-of-concept study, 30 equivalents of racemic lactide (LA) were polymerized with (salphen)Al^{i}OPr (salphen = [(3,5-^{t}Bu-1-OH-C_6H_2)CH=N]$_2$-C_6H_4) in toluene at 80°C in a J-Young NMR tube for 24 hours. Instead of quenching with methanol to leave methoxy end groups on the polymer chain as would be standard, the tube was transferred back into the glove box, and 0.5 equivalents of PEG4000 was added. The tube was then resealed and brought outside of the glovebox and heated at 80°C overnight with occasional shaking to fully solubilize the PEG, so quenching could occur (Figure 4.5).

Because PEG has two pendant alcohol groups, the goal was to quench one LA polymerization at each end of the PEG chain, and to end up with PLA-PEG-PLA triblock

copolymers. That way, this method could be applied to other monomers we commonly polymerize with aluminum-salen type compounds such as trimethylenecarbonate or cyclohexenoxide to impart water solubility. Unfortunately, after several attempts, the presence of PLA-PEG-PLA could not be confirmed by either size exclusion chromatography (SEC) (data not shown) nor diffusion ordered spectroscopy (DOSY) (Figure S59). Stejskal-Tanner plots indicated that a mixture of homopolymers was present and not the desired copolymer (Figure S60). Overall, PEG quenching was not going to be a facile route toward forming novel friction reducers, so we turned to different approaches.

4.2.2 Poly(succinimide) derivatives

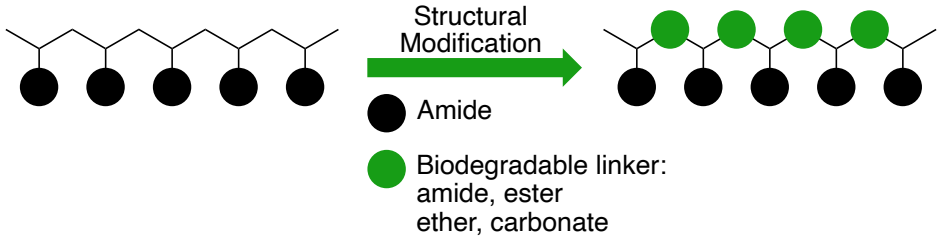

Figure 4.6 Overview of creating biodegradable polymers with pendant amide residues.

Intuitively, one of the easiest ways to increase the biodegradability of polymers is to include biodegradable functional groups such as ester or amide linkages in the polymer backbone (Figure 4.6). Given how problematic ester hydrolysis has been shown to be in Slickwater chemistry, amide groups are prefered.[20, 21] However, it should be noted that polyamides without pendant side chains (Nylons) are not water soluble. Therefore, it is important to create synthetic structures that have high fidelity with regards to PAM, namely ensuring pendant amide residues are present.

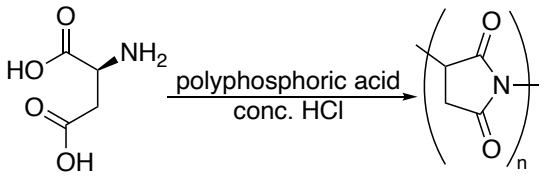

Figure 4.7 Synthesis of poly(succinimide) (PSI).

One of the most facile – and thus one of the most industrially viable – routes to achieving poly(amides) with amide side chains is through the thermal polycondensation of aspartic acid to form poly(succinimide) (Figure 4.7). Briefly, aspartic acid is dissolved in a minimal amount of concentrated HCl and poly(phosphoric acid) is added at 30 w/w% as the catalyst.[35] The mixture is evaporated to dryness with stirring at 80°C before being heated at 200°C under a dynamic vacuum for 2 hours for polymerization to occur. The resulting foamy solid is washed with deionized water and dried to afford poly(succinimide) (PSI) in nearly quantitative yield.

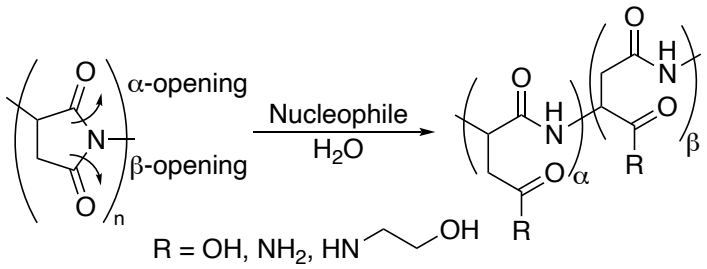

Figure 4.8 Different modes of hydrolysis or ammonolysis of PSI with the R groups studied here.

With PSI in hand, the polymer can be ring opened with any primary amine to form a plurality of pendant amides.[36] Nucleophilic attack can occur at both carbonyl groups, and a mixture of the alpha and beta ring opening products is typically obtained (Figure 4.8). With the goal of making structural analogues of PAM in mind, we first set out to synthesize poly(asparagine). Treatment of PSI with aqueous ammonia will result in a mixture of hydrolysis and ammonolysis products, preferentially forming poly(aspartic acid) over poly(asparagine).[37] When a large stoichiometric excess of NH_4OH is employed, it leads almost exclusively to poly(aspartic acid).

However, when a 1.5 molar ratio of NH_4OH to succinimide units is used, the resulting polymer has ~16% pendant amide residues corresponding to poly(asparagine) moieties as calculated by ^1H NMR spectroscopy (Figure S57). Unfortunately, liquid ammonia is needed to access poly(asparagine), and the synthesis of this polymer for its investigation as a friction reducer is currently underway.[38]

The ammonolysis of PSI with ethanolamine was also studied (Figure 4.8). Briefly, PSI was suspended in water and was stirred with 1.5 equivalents of ethanolamine to succinimide units overnight. Residual solvents were removed by vacuum distillation, and the resulting viscous oil was lyophilized to afford a glassy solid, poly[(2-hydroxyethyl)-DL-aspartamide] (PHEA). The ^1H NMR spectrum of PHEA shows the differences in alpha versus beta ring opening with clear separations observed in the methine peaks (Figure S58). A slight 3:2 preference for ring opening at the less sterically hindered beta position was observed.

4.2.3 Viscosity measurements

Typically, friction reduction measurements are conducted in flow loops at high pump rates to mimic pipeline conditions.[39] However, this testing method requires large quantities of polymer (on the order of 5-20 g per run). Fortunately, viscosity versus shear rate measurements require significantly less polymer (on the order of 1 mg per run) and offer a method to benchmark novel polymers against industry standards.

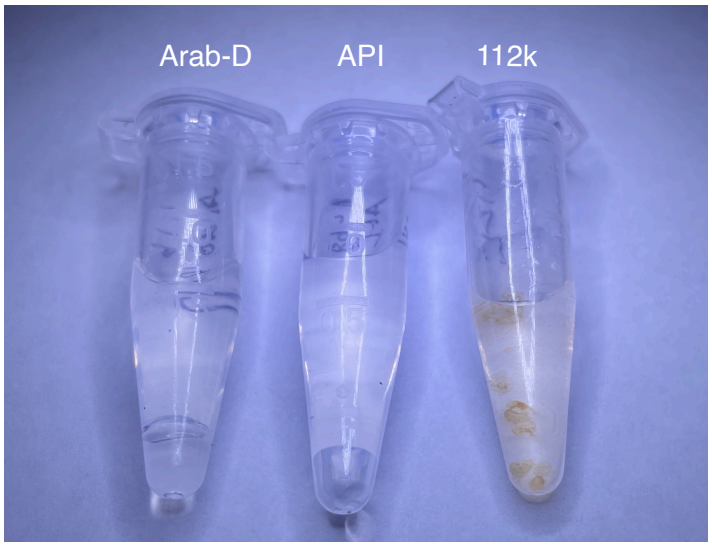

Figure 4.9 Industry standard PAM in three different brines. Note the flocculation in 112k brine.

The PAM standard (a proprietary acrylamide/acrylic acid copolymer) used for benchmarking was graciously provided by SNF Holding Company. In order to simulate real world applications, measurements were taken in 3 different brines as well as MilliQ water. The brines chosen were the American Petroleum Institute (API) brine as an example of a neutral brine with high total dissolved solids, Arab-D as an example of an alkaline brine, and 112k as an example of an acidic brine with high iron content. As expected (see discussion on polyacrylamide), viscosity is greatly reduced in the presence of high total dissolved solids, and the polymer flocculates in the presence of iron. Viscosity measurements are expected to be in the range of 1-10 centiPoise (cP) at a shear rate of 512 s^{-1} for friction reducers.[8] Both the API and Arab-D brines meet this metric for the industry PAM (112k brine was not run because of the flocculation issues, Figures 4.9-4.10), and this viscosity will be used as the benchmark measurements for comparison.

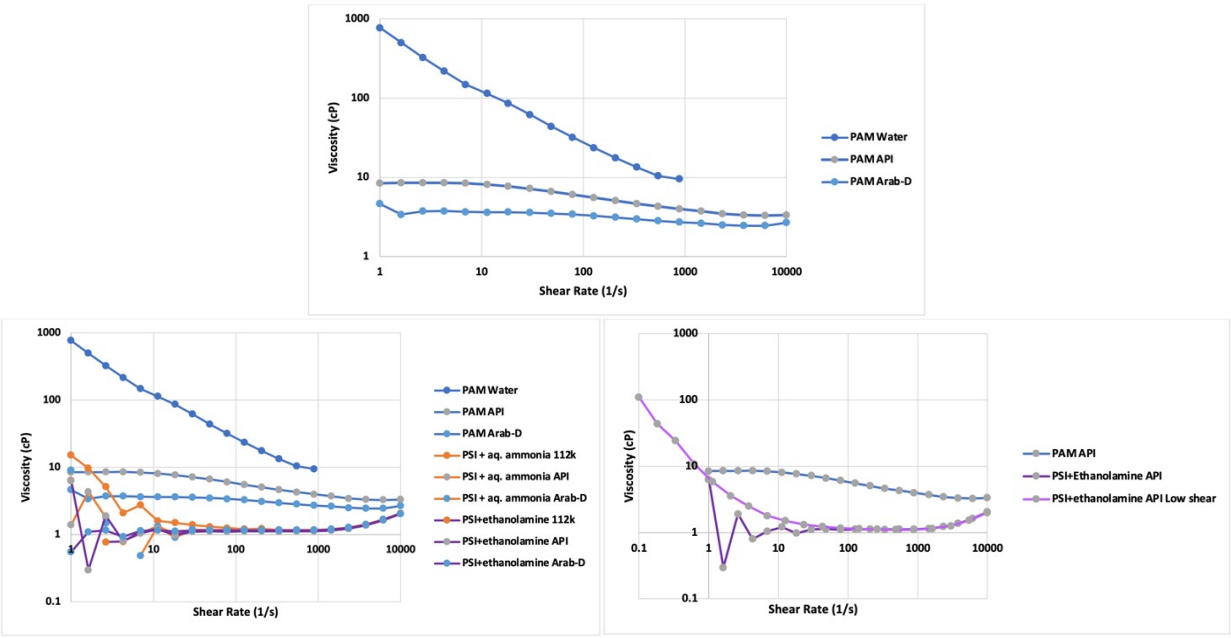

Figure 4.10 Viscosity versus shear rate measurements. *Top:* PAM standard. *Bottom left:* Comparison between PAM, poly(aspartic acid), and PHEA. *Bottom right:* PHEA measurement starting at 0.1 s^{-1} compared to PHEA and PAM measurements starting at 1 s^{-1}.

Poly(aspartic acid) and PHEA were also evaluated in API, Arab-D, and 112k brines. Excitingly, PHEA was stable in 112k brine while poly(aspartic acid) flocculated, likely owing to the ionic charges on the aspartate residues. At 512 s^{-1}, all conditions assayed have a viscosity of ~1cP (Figure 4.10). This falls within the acceptable range for viscosity imparted by a friction reducer, and the performance of these polymers, especially PHEA, in flow loops warrants further investigation. Noise at the start of measurements can likely be attributed to either thixotropic or rheopexic effects (i.e. a time delay before true viscosity at a given shear rate is met).[40] Starting measurements at lower shear rates appears to alleviate the issue, and future measurements will take this effect into account.

4.3 Conclusions and future directions

A project was started, and a workflow developed for finding biodegradable alternatives to PAM in friction reduction applications for hydraulic fracturing. PHEA was identified as a potential target for future investigations on the basis of viscosity versus shear rate measurements. Work still

needs to be done to ascertain the molecular weights of the polymers synthesized. Unfortunately, the polymers are not soluble in THF, so we are actively seeking out a size exclusion chromatogram (SEC) that has a DMSO, DMF, or water column. Different catalyst loadings need to be investigated to determine what effect that has on the final molecular weight of PSI. Ideally, once conditions for a PSI synthesis with the highest molecular weight are identified, the ammonolysis of PSI in the presence of various primary amines will be investigated, and the performance of the resulting polymers as friction reducers will be evaluated. Since the PSI synthesis utilized in this thesis is already running on a multigram scale, line of site for industrial scale application is established, and green chemistry principles are also employed.[41] This point is important for mitigating the environmental impact friction reducers have without sacrificing performance or cost. Overall, while further investigation is necessary, PSI derivatives may be a viable replacement for PAM based friction reducers in hydraulic fracturing.

4.4 Experimental

General considerations. PEG quenching experiments were performed under a dry nitrogen atmosphere in an MBraun glovebox or using standard Schlenk techniques. PSI experiments were performed in a fume hood without exclusion of air. Solvents for the glovebox chemistry were purified with a two-state solid-state purification system by the method of Grubbs[42] and transferred into a glovebox without exposure to air. All other solvents were used as received. NMR solvents were purchased from Cambridge Isotope Laboratories and used as received. ^{1}H NMR spectra were recorded on Bruker AV-300, Bruker AV-500, or Bruker AV-600 spectrometers at room temperature. Chemical shifts are reported with respect to the residual solvent peaks, 7.26 ppm ($CDCl_3$), 7.16 ppm (C_6D_6), 7.26 ppm ($CDCl_3$), 4.79 ppm (D_2O), 2.50 (d_6-DMSO) for ^{1}H NMR spectra. Racemic lactide was recrystallized from toluene at least twice before use. PEG was dried

using 3 Å molecular sieves in DCM. (*L*)-aspartic acid, concentrated HCl, polyphosphoric acid, NH_4OH, and ethanolamine were purchased from Fisher Scientific and used as received. (salphen)Al^{i}OPr was synthesized according to a previously published procedure.[43] Molar masses of THF soluble polymers were determined by size exclusion chromatography using a SEC-MALS instrument at UCLA. SEC-MALS uses a Shimadzu Prominence-i LC 2030C 3D equipped with an autosampler, two MZ Analysentechnik MZ-Gel SDplus LS 5 μm, 300 × 8 mm linear columns, a Wyatt DAWN HELEOS-II, and a Wyatt Optilab T-rEX. The column temperature was set at 40 °C. A flow rate of 0.70 mL min^{-1} was used and samples were dissolved in THF. The number average molar mass and dispersity values were determined using the d*n*/d*c* values which were calculated by 100% mass recovery method from the RI signal.

PEG Quenching. (salphen)Al^{i}OPr (3 mg, 4.8 μmol) was dissolved in toluene in a J-Young NMR tube and racemic lactide (20.7 mg, 144 μmol) was added. The tube was capped, brought out of the glovebox, and heated at 80°C for 24 hours before transferring back into the glovebox. Then PEG (4000 Da, 9.6 mg, 2.4 μmol) was added to the tube, and the reaction mixture was allowed to react for an additional 12 hours at 80°C. The reaction mixture was poured into CH_2Cl_2 and the polymer was crashed with cold Et_2O and isolated via centrifugation. Redissolving in CH_2Cl_2 and crashing from Et_2O was repeated until a white solid was obtained. Lactide-PEG-lactide copolymers could not be made in this manner.

PSI Synthesis. (L)-aspartic acid (5.1 g, 38 mmol) was suspended in 20 mL concentrated HCl and 30% w/w polyphosphoric acid (1.5 g) was added. This mixture is stirred at 105°C with a stream of air directed over the top until a semi-wet solid is obtained. The flask is then transferred to a Vacuum oven and the thermal polycondensation is induced at 200°C under dynamic vacuum for 2 hours. The resulting tough foam is torn into pieces and washed with water followed by ethanol

in a Buchner funnel to remove the acid catalyst. The solid is then re-dried at 100°C under dynamic vacuum for several hours to yield PSI as an off-white solid (3.2 g, 84%). ^{1}H NMR (300 MHz, 298K, D_6-DMSO) δ (ppm): 5.27 (br s, 1H, CH), 3.20 (br s, 1H CH_2), 2.69 (br s, 1H CH_2).

General Procedure for PSI derivatization. PSI (250 mg, 2.5 mmol by succinimide unit) is suspended in H_2O and the primary amide (3.8 mmol) is added. The mixture is allowed to stir until no precipitate remains, often overnight. The polymer can be isolated by vacuum distillation of water followed by lyophilization to yield either powders or glassy solids in quantitative yields.

Brines. The brines tested are API, Arab-D, and 112k. The recipes are as follows, and all percentages are presented as w/w. 112K is presented first as ppm in ion concentration then as concentration of compounds used.

API: 8%, 20 g, NaCl; 2%, 5 g, $CaCl_2$•$2H_2O$ in 225 mL MiliQ water.[44]

Arab-D: 7.5% NaCl (16.8 g), 5.0% $CaCl_2$•$2H_2O$ (11.2 g), 1.3% $MgCl_2$•$6H_2O$ (2.97 g), 0.006% Na_2SO_4 (0.135 g), 0.005% $NaHCO_3$ (0.117 g), 0.001% $BaCl_2$ (2.25 mg) in 225 mL MiliQ water.[44]

112k: 10.9 ppm Ba^{2+}, 1,503 ppm Sr^{2+}, 52.08 Fe^{2+}, 5,743 ppm Ca^{2+}, 709.9 ppm Mg^{2+}, 187.4 ppm SO_4^{2-}, 476 ppm HCO_3^-, 35,597 ppm Na^+, 68,000 ppm Cl^-. 0.015 g/L $BaCO_3$, 1.777 g/L SrO, 0.115 g/L $FeCl_2$•$4H_2O$, 21.06 g/L $CaCl_2$•$2H_2O$, 2.78 g/L $MgCl_2$, 0.276 g/L Na_2SO_4, 0.006 g/L $NaHCO_3$, 89.84 g/L NaCl, 5.66 mL/L concentrated HCl all in MiliQ water.

Rheology. Viscosity versus shear rate measurements were assessed by rheology experiments (Anton Paar MCR 302) using a cone and plate geometry (50 mm diameter, 2° cone angle). Samples were dissolved in the indicated brine to a final concentration of 1.2 mg/mL and transferred to the rheometer within an hour. A solvent trap was installed during measurements to minimize solvent evaporation, and the temperature was set to 25°C for measurements. Samples were allowed to equilibrate (2 minutes) and pre-sheared by subjecting them to an oscillatory strain with strain

amplitude (γ) of 0.5% and angular frequency (ω) of 1 rad s^{-1} for ~2 minutes. Samples were then subject to increasing shear rates from either 0.1 or 1 rad s^{-1} up to 10,000 rad s^{-1} over 20 steps at 30 second intervals and viscosity was recorded. All data were processed and plotted using Excel.

4.5 References

(1) Montgomery, C. T.; Smith, M. B. Hydraulic Fracturing: History of an Enduring Technology. *J. Pet. Technol.* **2010**, *62* (12), 26-40.

(2) Clark, J. B. A Hydraulic Process for Increasing the Productivity of Wells. *J. Pet. Technol.* **1949**, *1* (01), 1-8.

(3) Zheltov, A. K. Formation of Vertical Fractures by Means of Highly Viscous Liquid. In *4th World Petroleum Congress*, 1955; WPC-6132, Vol. All Days.

(4) Yuan, J.; Luo, D.; Feng, L. A review of the technical and economic evaluation techniques for shale gas development. *Applied Energy* **2015**, *148*, 49-65.

(5) Middleton, R. S.; Gupta, R.; Hyman, J. D.; Viswanathan, H. S. The shale gas revolution: Barriers, sustainability, and emerging opportunities. *Applied Energy* **2017**, *199*, 88-95.

(6) Ahmad, F. A.; Miskimins, J. L. An Experimental Investigation of Proppant Transport in High Loading Friction-Reduced Systems Utilizing a Horizontal Wellbore Apparatus. In *Unconventional Resources Technology Conference*, Denver, Colorado, 22–24 July 2019, pp 2502-2520.

(7) Nizamidin, N.; Matovic, G.; Kim, D. H.; Theriot, T.; Linnemeyer, H.; Han, S.; Malik, T. Universal Behavior of Polyacrylamide-Based Friction Reducers: Achieving Quantitative Lab Evaluation to Analytical Scale-up Model Development for Field Performance Prediction. In *Proceedings of the 9th Unconventional Resources Technology Conference*, 2021.

(8) Harry, D.; Horton, D.; Durham, D.; Constable, D. J. C.; Gaffney, S.; Moore, J.; Todd, B.; Martinez, I. Grand Challenges and Opportunities for Greener Chemical Alternatives in Hydraulic Fracturing: A Perspective from the ACS Green Chemistry Institute Oilfield Chemistry Roundtable. *Energy & Fuels* **2020**, *34* (7), 7837-7846.

(9) Wu, J. J. Role of Friction Reducers on Formation Fluid Flow. In *53rd U.S. Rock Mechanics/Geomechanics Symposium*, 2019; ARMA-2019-1550, Vol. All Days.

(10) Reynolds, O. An experimental investigation of the circumstances which determine whether the motion of water shall be direct or sinuous, and of the law of resistance in parallel channels. *Philos. Trans. R. Soc. London* **1883**, *174*, 935-982.

(11) Xi, L. Turbulent drag reduction by polymer additives: Fundamentals and recent advances. *Phys. Fluids* **2019**, *31* (12), 121302.

(12) Toms, B. A. Some Observations on the Flow of Linear Polymer Solutions Through Straight Tubes at Large Reynolds Numbers. In *Proc. 1st Inter. Rheol. Congr.*, Amsterdam, 1948; North Holland Publishing Co.

(13) McComb, W. D.; Rabie, L. H. Local drag reduction due to injection of polymer solutions into turbulent flow in a pipe. Part I: Dependence on local polymer concentration. *AlChE J.* **1982**, *28* (4), 547-557.

(14) McComb, W. D.; Rabie, L. H. Local drag reduction due to injection of polymer solutions into turbulent flow in a pipe. Part II: Laser-doppler measurements of turbulent structure. *AlChE J.* **1982**, *28* (4), 558-565.

(15) Lumley, J. L. Drag Reduction by Additives. *Annu. Rev. Fluid Mech.* **1969**, *1* (1), 367-384.

(16) Tabor, M.; Gennes, P. G. d. A Cascade Theory of Drag Reduction. *Europhys. Lett.* **1986**, *2* (7), 519-522.

(17) Virk, P. S. Drag reduction fundamentals. *AlChE J.* **1975**, *21* (4), 625-656.

(18) Xiong, B.; Miller, Z.; Roman-White, S.; Tasker, T.; Farina, B.; Piechowicz, B.; Burgos, W. D.; Joshi, P.; Zhu, L.; Gorski, C. A.; et al. Chemical Degradation of Polyacrylamide during Hydraulic Fracturing. *Environ. Sci. Technol.* **2018**, *52* (1), 327-336.

(19) Reynolds, M. A. A Technical Playbook for Chemicals and Additives Used in the Hydraulic Fracturing of Shales. *Energy & Fuels* **2020**, *34* (12), 15106-15125.

(20) Shen, L.; Khan, S.; Heller, D.; Fu, D. A Cationic Friction Reducer Fully Compatible with Produced Water. In *SPE/AAPG/SEG Unconventional Resources Technology Conference*, 2019; D013S022R002, Vol. Day 1 Mon, July 22, 2019.

(21) Hazra, S.; Van Domelen, M.; Cutrer, W.; Peregoy, N.; Okullo, P.; Darlington, B. Performance of Friction Reducers in Iron-Rich Environments. In *SPE/AAPG/SEG Unconventional Resources Technology Conference*, 2020; D033S062R001, Vol. Day 3 Wed, July 22, 2020.

(22) Xiong, B.; Zydney, A. L.; Kumar, M. Fouling of microfiltration membranes by flowback and produced waters from the Marcellus shale gas play. *Water Res.* **2016**, *99*, 162-170.

(23) Riley, S. M.; Oliveira, J. M. S.; Regnery, J.; Cath, T. Y. Hybrid membrane bio-systems for sustainable treatment of oil and gas produced water and fracturing flowback water. *Sep. Purif. Technol.* **2016**, *171*, 297-311.

(24) Kwon, S.; Sullivan, E. J.; Katz, L. E.; Bowman, R. S.; Kinney, K. A. Laboratory and Field Evaluation of a Pretreatment System for Removing Organics from Produced Water. *Water Environ. Res* **2011**, *83* (9), 843-854.

(25) Chellam, S.; Sari, M. A. Aluminum electrocoagulation as pretreatment during microfiltration of surface water containing NOM: A review of fouling, NOM, DBP, and virus control. *J. Hazard. Mater.* **2016**, *304*, 490-501.

(26) Elsner, M.; Hoelzer, K. Quantitative Survey and Structural Classification of Hydraulic Fracturing Chemicals Reported in Unconventional Gas Production. *Environ. Sci. Technol.* **2016**, *50* (7), 3290-3314.

(27) Gao, J.; Lin, T.; Wang, W.; Yu, J.; Yuan, S.; Wang, S. Accelerated chemical degradation of polyacrylamide. *Macromolecular Symposia* **1999**, *144* (1), 179-185.

(28) Levitt, D. B.; Slaughter, W.; Pope, G. A.; Jouenne, S. The Effect of Redox Potential and Metal Solubility on Oxidative Polymer Degradation. *SPE Reservoir Evaluation & Engineering* **2011**, *14* (03), 287-298.(acccessed 5/29/2022).

(29) Braun, O.; Coquery, C.; Kieffer, J.; Blondel, F.; Favero, C.; Besset, C.; Mesnager, J.; Voelker, F.; Delorme, C.; Matioszek, D. Spotlight on the Life Cycle of Acrylamide-Based Polymers Supporting Reductions in Environmental Footprint: Review and Recent Advances. *Molecules* **2021**, *27* (1), 42.

(30) Muller, G. Thermal stability of high-molecular-weight polyacrylamide aqueous solutions. *Polym. Bull.* **1981**, *5* (1), 31-37.

(31) Muller, G.; Fenyo, J. C.; Selegny, E. High molecular weight hydrolyzed polyacrylamides. III. Effect of temperature on chemical stability. *J. Appl. Polym. Sci.* **1980**, *25* (4), 627-633.

(32) Andrady, A. L. Microplastics in the marine environment. *Mar. Pollut. Bull.* **2011**, *62* (8), 1596-1605.

(33) Bhattacharya, P.; Lin, S.; Turner, J. P.; Ke, P. C. Physical Adsorption of Charged Plastic Nanoparticles Affects Algal Photosynthesis. *J. Chem. Phys. C* **2010**, *114* (39), 16556-16561.

(34) Brown, D. M.; Wilson, M. R.; MacNee, W.; Stone, V.; Donaldson, K. Size-Dependent Proinflammatory Effects of Ultrafine Polystyrene Particles: A Role for Surface Area and Oxidative Stress in the Enhanced Activity of Ultrafines. *Toxicol. Appl. Pharmacol.* **2001**, *175* (3), 191-199.

(35) Sikes, C. S. Preparation of High Molecular Weight Polysuccinimides. U.S. Patent US 007053170B2, May 30, 2006.

(36) Jalalvandi, E.; Shavandi, A. Polysuccinimide and its derivatives: Degradable and water soluble polymers (review). *Eur. Polym. J.* **2018**, *109*, 43-54.

(37) Groth, T.; Joentgen, W.; Jovcic, D.; Wagner, P.; Traenckner, H. J. Process for the preparation of polysuccinimide. U.S. Patenet 5493004, February 20, 1996.

(38) Ma, Z. A process for the production of polyasparagine and the high nitrogen content polymer formed thereby. U.S. Patent WO 2001098394A1, June 21, 2000.

(39) Khadom, A. A.; Abdul-Hadi, A. A. Performance of polyacrylamide as drag reduction polymer of crude petroleum flow. *Ain Shams Engineering Journal* **2014**, *5* (3), 861-865.

(40) Potanin, A. Thixotropy and rheopexy of aggregated dispersions with wetting polymer. *J. Rheol.* **2004**, *48* (6), 1279-1293.

(41) Anastas, P.; Eghbali, N. Green Chemistry: Principles and Practice. *Chem. Soc. Rev.* **2010**, *39* (1), 301-312, 10.1039/B918763B.

(42) Pangborn, A. B.; Giardello, M. A.; Grubbs, R. H.; Rosen, R. K.; Timmers, F. J. Safe and Convenient Procedure for Solvent Purification. *Organometallics* **1996**, *15* (5), 1518-1520.

(43) Hormnirun, P.; Marshall, E. L.; Gibson, V. C.; Pugh, R. I.; White, A. J. P. Study of ligand substituent effects on the rate and stereoselectivity of lactide polymerization using aluminum

salen-type initiators. *Proceedings of the National Academy of Sciences* **2006**, *103* (42), 15343-15348.

(44) Zuniga, C. A.; Goods, J. B.; Cox, J. R.; Swager, T. M. Compositions of and methods for making stable carbonaceous nanomaterials. U.S. Patent 20160348498A1, June 1, 2016.

Chapter 5: Ruminations on compartmentalization

5.1 Introduction

One of the goals of synthetic catalysis is to obtain a bio-like level of control over chemical transformations. Unfortunately, organometallic catalysts tend to fall short of their enzymatic counterparts in terms of reactivity, selectivity, and turnover number. The superiority of enzymatic catalysts can be attributed in part to their extreme control over the chemical environment of the catalytic pocket. From a reductionist viewpoint, the tertiary structure of an enzyme confines the active site from the protein's external environment. This confinement offers an additional level of chemical definition not often considered when designing traditional organometallic catalysts. Confining the active site contributes to the enhanced properties of enzymatic catalysis, and in return, offers additional methodology.

Intuitively, the easiest way to confine an organometallic catalyst is to place it inside of a "compartment". However, what defines a compartment is necessarily broad. As a starting point, we will consider a compartment to be any open system in which a chemical reaction takes place. Under this first iteration of the definition, a reaction taking place in an uncapped round bottom flask can be considered a reaction inside of a compartment -- the reaction inside is confined from mixing with its bulk external environment except through the opening at the top of the flask. This macroscopic example of a compartment exhibits how confinement is already well established in chemistry: compartments confine chemicals in an environment suited for us to study their reactivity. However, the more interesting frontiers of compartmentalization happen in nanoscopic systems. These types of compartments offer the same benefits as their macroscopic counterparts in terms of studying reactivity, but they also introduce novel opportunities to study molecular control.

The increased levels of control that nanoscale compartments offer are the next step toward achieving biomimetic systems. Confined systems have been reviewed extensively in the literature,[1-13] so instead we try to elucidate the main design principles at work in confinement chemistry. In this perspective, we will cover a set of representative examples in different types of confinement and make comments on how these systems are designed before providing suggestions regarding the utility of confinement.

5.1.1 A definitional example: cells & enzymes

Given that biomimetic catalysis is the ultimate goal, it's useful to take metalloenzymes as the exemplar case of organometallic confinement, and create a top-down model of what makes a nanoscopic compartment. When a hypothetical enzyme A is inside of a cell, the enzyme is naturally confined within the cell membrane. However, cells are still open systems, and molecules of certain types are allowed to flow in and out. If one of those molecules is a substrate for enzyme A, we can consider the enzyme to be confined within the open system of the cell with limited access to potential substrates. Therefore, the principal function of the cell, and thus of a compartment, is to control diffusion of substrates. Confinement is useful because it introduces a form of control by limiting what species the catalyst has access to.

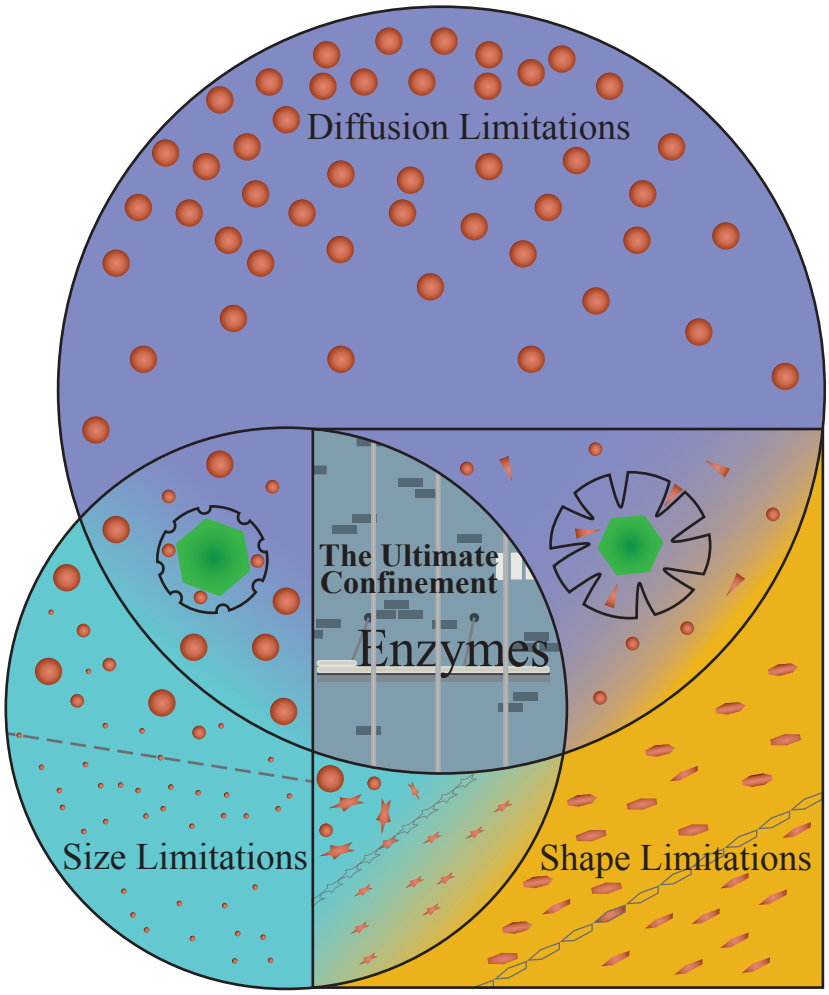

Figure 5.1 Venn diagram showing the three uses of confinement and how they overlap.

However, we must also consider why the active site of enzyme A is non-promiscuous even in the mixture of substrates it does have access to. Ultimately, structure dictates function. The folding of the protein creates a cavity that limits what substrates reach the active site based on the substrate's size and shape. This limitation is so good that it can even cause stereoselective reactions to occur. Consequently, the ultimate compartment for a catalyst is one that can control both diffusion of unwanted substrates and orient the correct ones. With this system in mind, we will categorize several examples found in literature working counterclockwise around Figure 5.1 in an attempt to identify design principles to consider when creating confined organometallic catalysts.

5.2 Guiding principles

5.2.1 Pure diffusion limitation

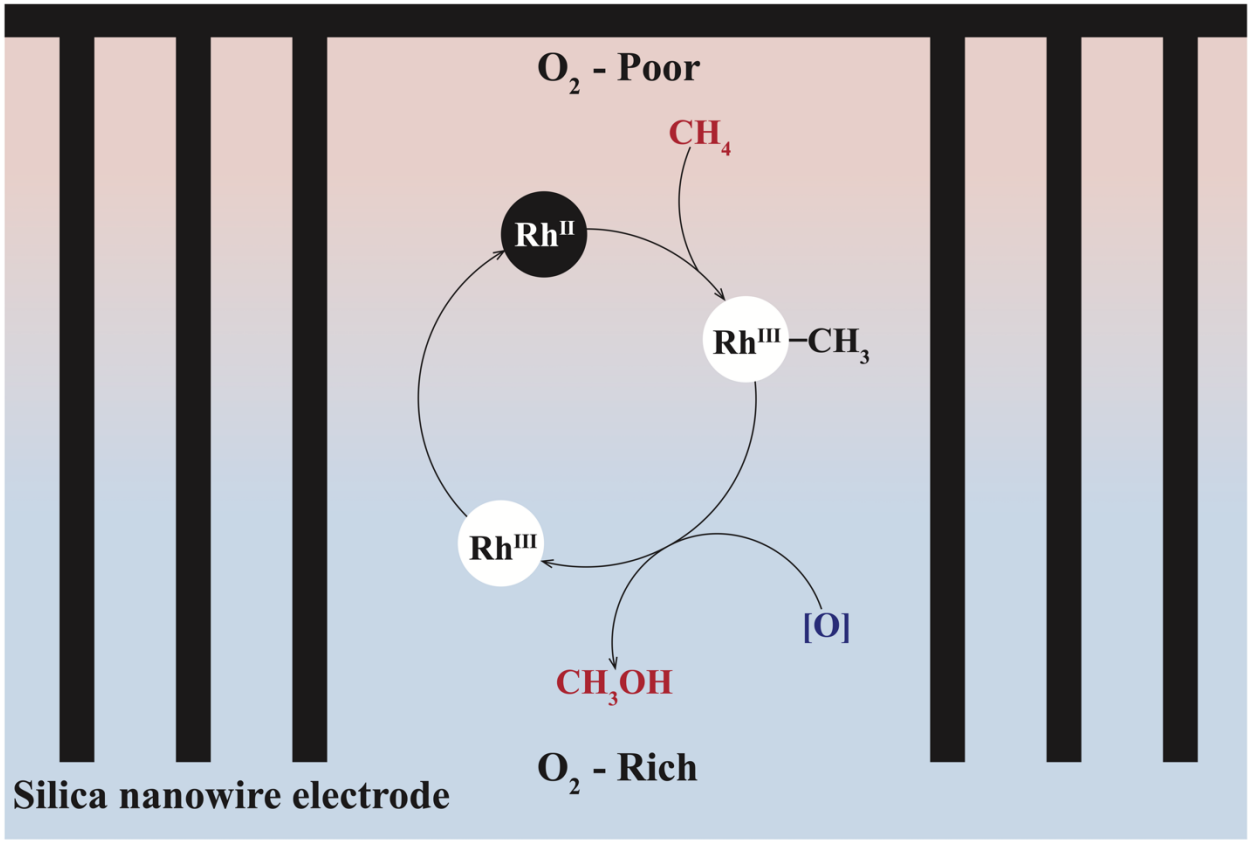

Figure 5.2 Silica nano-wire array exemplifying diffusion limiting control.

Much like the case of a single cell, the properties of a compartment can help to control the bulk diffusion of certain species. One practical use of controlling diffusion is the exclusion of potentially poisonous species from the reaction. In cases of catalytic poisoning, it is possible to design a compartment that allows for just that.[14] Liu and coworkers were able to create an anoxic microenvironment that prevents oxygen poisoning of their catalyst, yet still allowed O_2 to be used in the oxidation of methane to methanol (Figure 5.2).[15, 16] In the presence of O_2, the oxidation of their Rh^{II} tetramesityl porphyrin metalloradical ((TMP)Rh^{II}) catalyst to form a Rh^{III} superoxo species is kinetically faster than the CH activation step to form (TMP)Rh^{III}-CH_3. However, by

applying a voltage to eliminate oxygen from the bottom of their compartment, (TMP)Rh^{III}-CH_3 is allowed to form and can react with the superoxo species to produce CH_3OH. Since oxygen is being consumed in the reaction, a gradient is created where there is less O_2 at the base of the array than at the top. This gradient allows the conversion of methane to methanol to proceed without complete formation of the kinetically favored Rh^{III} superoxo species. In this sense, (TMP)Rh^{II} is confined to the anoxic environment created by that array, and it's allowed to diffuse from the O_2-free to the O_2-rich environment as mechanistically necessary. By introducing diffusion limitations, they are able to manipulate kinetic factors that would not be possible to do in non-confined systems, and in this instance, changing kinetic factors ultimately led to enhanced reaction rates and turnover numbers for their catalyst.[17]

Pure diffusion limited systems are harder to find examples of in literature because they are almost exclusively engineering issues. Diffusion is a bulk process, so there is a necessary level of abstraction from a chemical model to a physical one where you no longer consider substrate approach to the catalyst. Consequently, most diffusion limiting cases have greater emphasis on reactor design. In order to utilize diffusion limitations in confinement chemistry, the system ultimately needs to be thought of in physical terms – a point that most confinement literature misses.

5.2.2 Diffusion & size limitations

Diffusion and size are inherently linked concepts, classically related via the Stokes-Einstein equation.[37] As a result, a lot of diffusion limited confinement relies on bigger molecules diffusing at slower rates than smaller ones. However, diffusion limitations can also be based on the hydrophilicity of compounds.

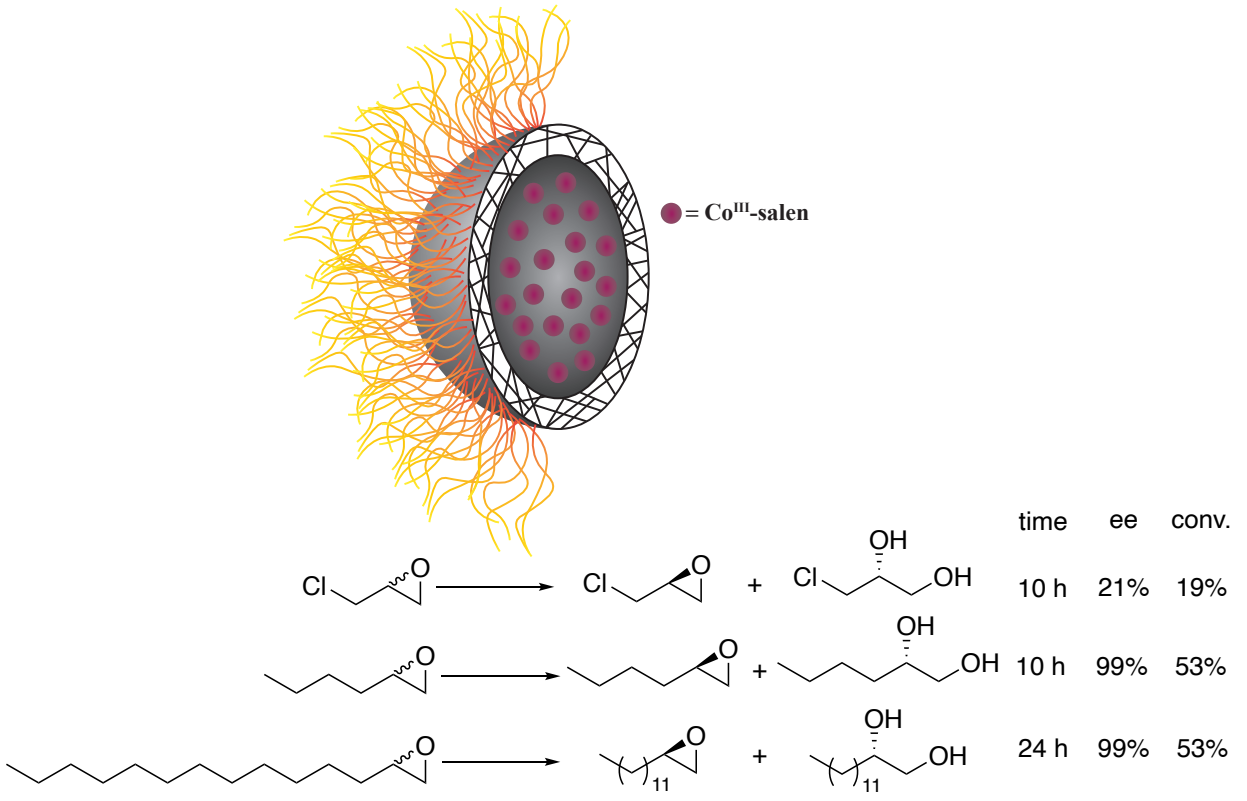

Figure 5.3 Micelle with a cross-linked inner core capable of discriminating between compounds based on both size and hydrophilicity.

Micelles are an interesting case study for diffusion limited systems as they closely mimic the ability of the cell membrane to dictate what molecules can and cannot cross them. Weck and coworkers created a shell crosslinked micelle with a cobalt(III)-salen core that can selectively hydrolyze hydrophobic epoxides over hydrophilic ones (Figure 5.3).[18] Therefore, by confining the catalyst inside of the micelle, the compartment introduces diffusion limitations on the basis of hydrophilicity. Additionally, within the scope of the hydrophobic epoxides they screened, smaller epoxides tended to hydrolyze faster than larger ones. This phenomena was not observed in the non-crosslinked version of the micelle and shows size discrimination due to the presence of crosslinks.[19] As a result, their micelle is dual purpose in how it can discriminate between substrates on the basis of both diffusion and size.

5.2.3 Size limitations

While diffusion is mainly based on size, systems exploiting size differences do not have to rely on diffusion, but they can instead introduce physical blockages to restrict the flow of larger molecules. Much of the current literature on confinement is based on substrate discrimination. From a research chemist's perspective, it's rare to deal with mixtures of undesirable substrates as the starting point for a reaction. Consequently, discrimination is only empirically useful when a mixture of those materials naturally exists. However, keeping the biomimetic goal in mind, the ability of enzymes to discriminate between substrates is essential for their function. Therefore, in order to obtain biomimetic catalysis, organometallic catalysts should be able to mimic substrate discrimination as closely as enzymes can.

One of the most common starting places in studying discrimination is to limit the size of what substrates can reach a catalytic active site. This type of chemistry is generally based on filtering substrates through a pore where only the smaller of two species can pass. As a result, the majority of examples of size limitations rely on the larger of substrates not being able to fit through the porous container due to steric constraints.[12] Substrate size filtering is fairly easy to implement and there are plenty of examples in cyclodextrin/cavitand chemistry, supramolecular host-guest chemistry, and ligand templating approaches.[1]

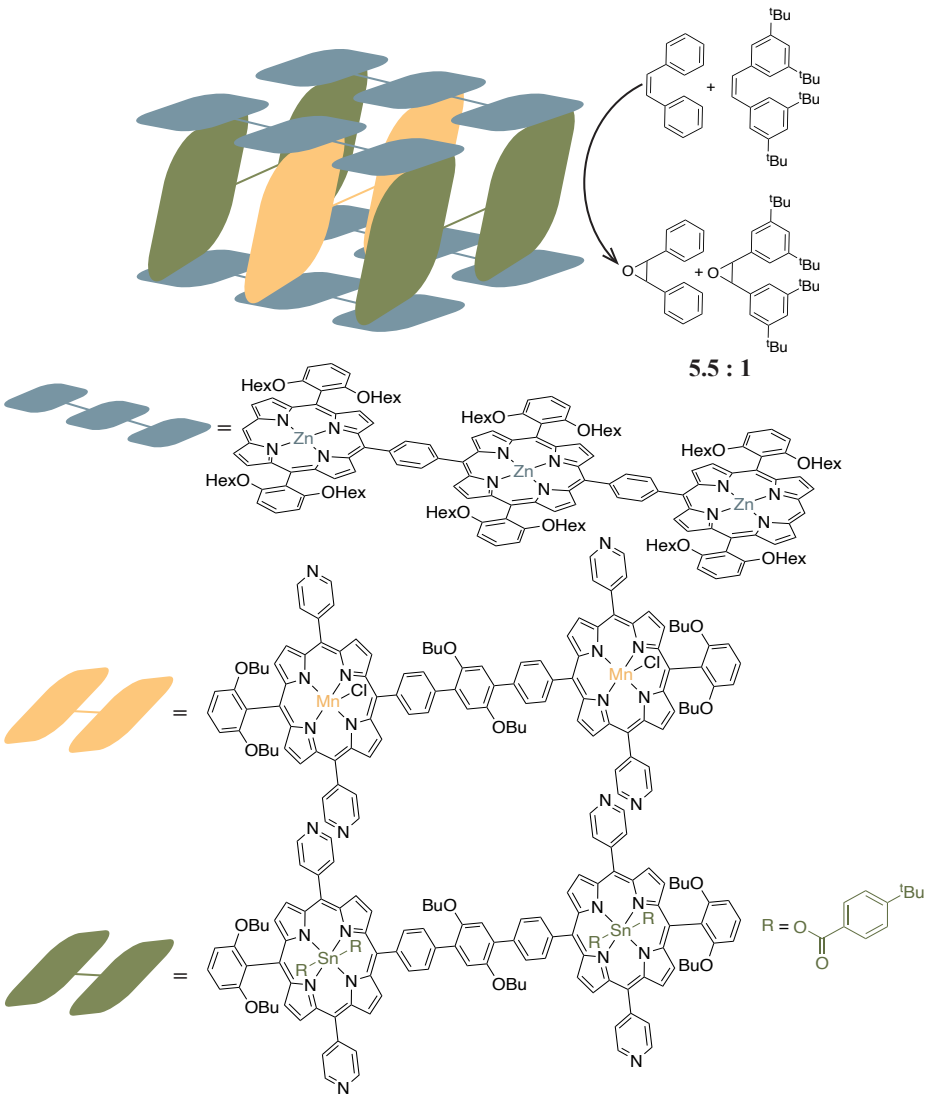

Figure 5.4 Ligand templated porphyrin box capable of discriminating based on size.

In a typical example of size filtering, a manganese porphyrin catalyst is constrained inside of a box comprised of zinc porphyrin complexes on the top and bottom and tin porphyrin complexes on the facial sides (Figure 5.4).[20] Epoxidation of a less sterically bulky alkene occurs preferentially to the epoxidation of a more sterically bulky alkene due to the accessibility of the manganese face. The main point being that the catalytically active metal must necessarily be protected on all sides to achieve discrimination. Regardless, confinement based on size limitations can be intuitively thought of as simple pore filtration. Size discrimination ultimately becomes a

two-dimensional problem because these systems have no ability to distinguish between the depth of the molecule. All that matters at any given angle of approach is the size of the projection of the substrates shape onto a two-dimensional plane. The catalyst sits far enough away from the pore that the substrate's shape becomes inconsequential to the filtration. In pure size limitation cases, the size of the entrance to the compartment plays an essential role in the effects of confinement.

5.2.4 Shape & size limitations

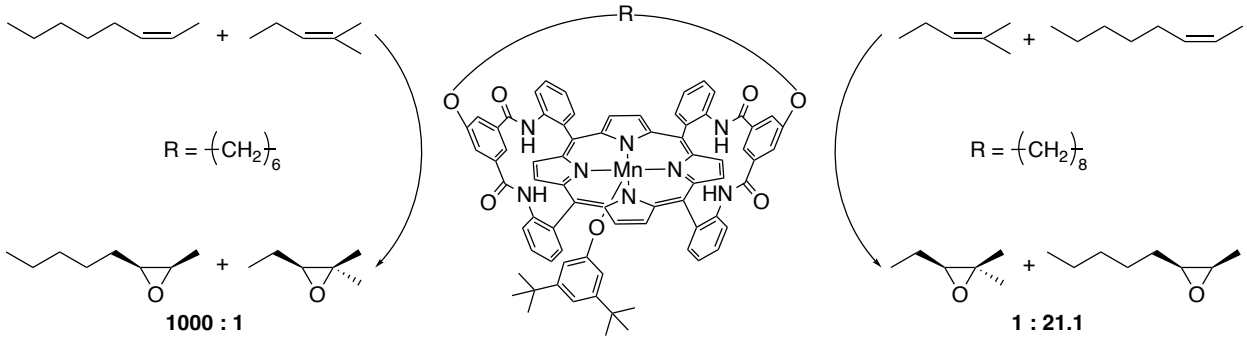

Figure 5.5 Porphyrin picnic basket compound showing shape and size discrimination.

Shape discrimination introduces increased selectivity into a confined system because the substrate now needs to approach the active site with a specified orientation. While shape discrimination alone can lead to stereo- or enantioselective reactions, incorporating a size component can further alter selectivities.[21, 22] One of the earliest successful examples that combines size discrimination between substrates is a preferential large substrate catalyst produced by Brauman and coworkers in 1990.[23] Using Mn(TTPPP(OAr)) ((5,10,15,20-tetrakis(2',4',6'-triphenylphenyl)porphyrinato)manganese(III), OAr = 3,5-di-*tert*-butyl-phenoxide) as a catalyst and iodosylbenzene as a stoichiometric oxidant in dry acetonitrile, they were able to achieve a >1000:1 preference for the epoxidation of large disubstituted alkenes over smaller trisubstituted alkenes, exclusively forming the (S,R) stereoisomer from internal alkenes (Figure 5.5). Importantly, when the X-type axial ligand was replaced with an L-type ligand like a 3,5-

disubstitued imidazole, this selectivity disappeared suggesting that reactivity in the X-type ligand case proceeds inside the cavity and not at the open face.[24] These results suggest that confinement based on both shape and size limitations can alter the orientation of approach of substrates toward a catalyst lending itself to selective reactivities.

One of the great things about size and shape limited systems is their ability to alter catalytic pathways by changing transition state barriers.[25] These systems can give access to different catalytic outcomes that would not be accessible without confinement just by altering substrate approach. However, *de novo* construction of a confined system for a specific synthetic problem is rarely worth the effort, and the best bet is probably an *ab initio* guided design from known synthetic systems.[26] Nevertheless, all design of shape and size limited systems need to consider the space within the cavity and think critically about the effects different spaces will have. By altering the type and amount of space a catalyst is confined within, control in both substrate approach and substrate release can be introduced, and this is even more useful if the desired product is an intermediate in a catalytic cycle.[27-29] Controlling the space inside a compartment is an important aspect of confinement design.

5.2.5 Shape limitations

In general, shape limitations can refer to either the overall physical shape of the substrate from a steric viewpoint or the shape of the molecular orbitals interacting with the catalyst. Consequently, shape selectivity is one of the main ways enzymes are able to discriminate between different substrates. Molecular recognition is a key aspect to consider when trying to design biomimetic systems. Enzymes are able to achieve molecular recognition through a variety of ways such as modifying pocket size, or introducing new hydrogen bonding or salt bridge interactions.[30] However, engineering these moieties into catalytic containers is time consuming and costly, and

as a result, most examples of shape discrimination in organometallic compartments are fairly rudimentary, with slightly wider substrate scope.

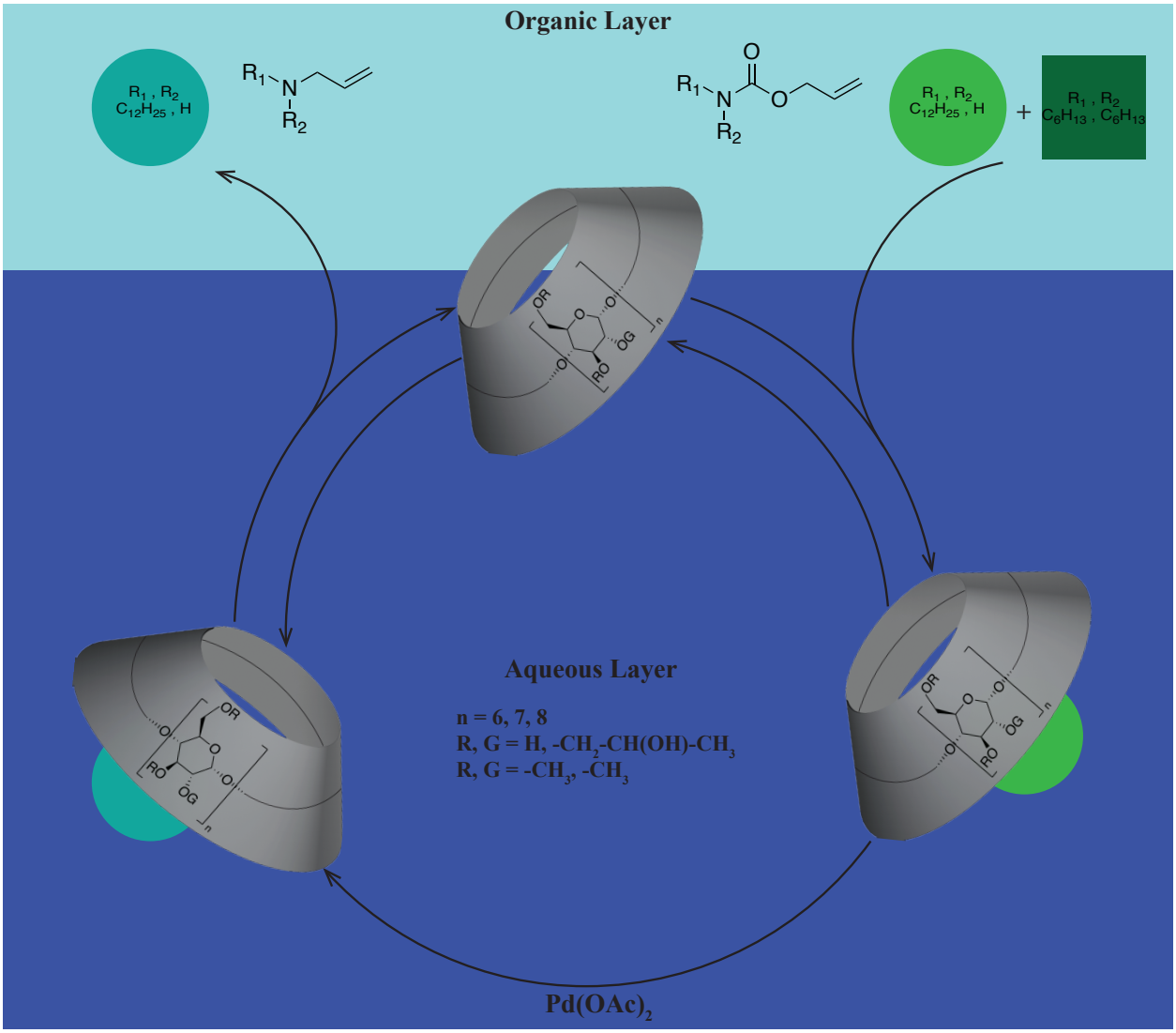

Figure 5.6 Cyclodextrins transporters selecting based on substrate shape.

One good example of a shape discrimination system was reported in 2005 by Monflier and coworkers. Various cyclodextrins were used as phase transfer reagents to preferentially transport *N*-dodecyl-*O*-allylurethane over *N*,*N*-dihexyl-*O*-allylurethane from an organic phase to a water soluble organometallic catalyst resulting in decarboxylation.[31] In the absence of cyclodextrins, catalytic activity was relatively slow at only 0.03 h^{-1}. However, the catalytic activity could be

increased by over 150-fold in the presence of methyl-α-cyclodextrin with a 7:1 preference for *N*-dodecyl-*O*-allylurethane, and the preference could be increased to 20:1 if small amines such as diethyl amine was added. Interestingly, both shape and size of the cyclodextrin was important for discriminating between the urethanes. Larger cyclodextrins and those containing 2-hydroxylpropyl R-groups instead of methyl R-groups showed decreases in selectivity with only around a 4:1 preference for *N*-dodecyl-*O*-allylurethane. This difference in selectivity implies that the cyclodextrins are capable of discriminating between the two molecules based on shape, and that some optimum cavity design exists for facilitating the discrimination.

In reality, cyclodextrins are frequently used to discriminate based on shape in confinement issues although the catalyst is normally confined inside the cavity of the cyclodextrin.[32, 33] While they don't necessarily provide well defined shape recognition, cyclodextrins introduce a three-dimensional argument in confinement. Unlike confinement that limits the size of molecules through pores, confinement that limits shape must consider the depth of the compartment as a fundamental tool in shape recognition. Molecules need to be thought of in more realistic manners than just their two-dimensional projection in order to recognize subtle difference in substrates. While current shape limitation systems are not as sophisticated as enzymatic regulation, compartment depth is an important design element to consider in confinement.

5.2.6 Diffusion & shape limitations

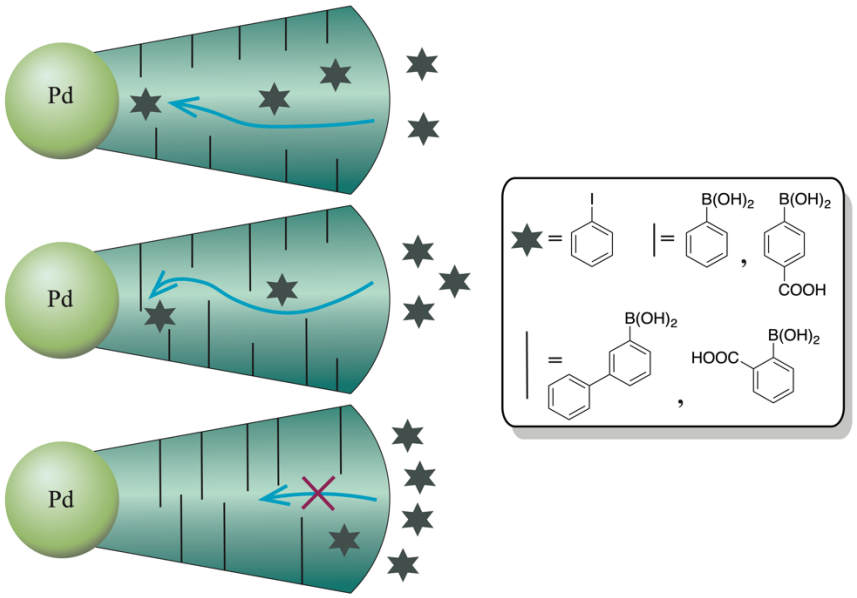

Figure 5.7 Pores of mesoporous silica nanoparticles with different phenyl boronic acids adsorped as a way to tune substrate accessibility to the Pd catalyst.

Considering compartment depth on a larger scale than just the microenvironment the catalyst occupies allows for the incorporation of diffusion limitations along with shape limitations. In 2012, Song and coworkers reported a diffusion-induced shape-selective Suzuki coupling reaction inside the pores of a mesoporous Pd@meso-SiO_2 nanoreactor (Figure 5.7).[34] In their system, Pd nanoparticles sit at the bottom of silica pores, and various phenylboronic acids adsorp to the silica walls, effectively creating tunable pore diameters. When larger phenylboronic acids are used, iodobenzne is not able to reach the Pd surface through the pore and only trace conversion is seen. However, upon the combination of a smaller phenyl boronic acid with a larger phenyl boronic acid, conversion of both acids to the coupled product is seen, implying that a type of diffusion mechanism is at work rather than simple size limitations. Shape selectivity of their catalyst is also observed with *ortho* substituted carboxyphenylboronic acid after only achieving trace conversion to the coupled product after 3 hours of residence time but *para* and *meta*

substituted carboxyphenylboronic acids achieving around 60% conversion only 3 minutes. This difference was not observed in their Pd/C model system, and therefore, it must be an emergent property resulting from the confinement.[35]

The mesoporous silica nanoparticles used are a good example of a system capable of regulating both shape and diffusion. The cavity depth employed is longer than what is used in shape limiting cases alone and allows for diffusion aspects to be incorporated into the confinement. While the mechanism for the shape limitation observed is unknown, it is not unreasonable to assume it stems from an orientation issue. Overall, even though this example is relatively complicated, it offers proof of concept that diffusion and shape limitations can exist in smaller and slightly more defined systems.

5.3 Design aspects

Up to this point we've covered a silica nanowire array, micelles, porphyrin boxes, basket handle compounds, cyclodextrins, and nanoparticles as examples of different categories of confined catalysts, and some clear trends are apparent. In order to design a successful compartment, the two biggest aspects to consider are the physical structure and space within. Here we break down how to think about those two aspects when designing compartments (Figure 5.8).

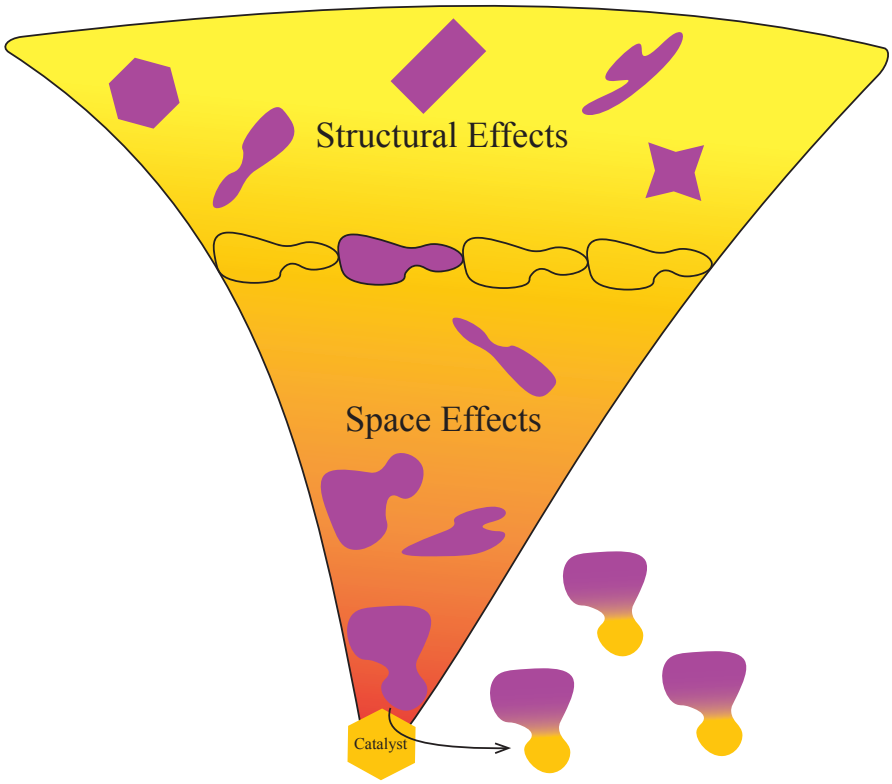

Figure 5.8 Design of compartments must take structural and space effects into account.

Most physical structures do not need to have strict chemically defined components since the main role that structure plays is limiting *what* has access to the catalytic active site. This lack of strict definition can be beneficial since it prevents catalysts from having too narrow of a reaction scope. Structural aspects can be applied to both diffusion and size problems. For diffusion issues, the material the structure is made from can have a profound impact on what can and cannot access the catalyst such as was seen with micelles selecting for hydrophobic molecules. Size problems are even easier to consider since all they necessitate is a tuning of pore size. However, it needs to be stressed that physicality is a compartment construction problem, and it needs to be thought of separately from the space it creates. Multiple components need to be present in a system, but if they are not arranged the right way, the compartment won't have the desired effects. The best structures have additional layers of modification that can be woven into their construction (i.e.

passing a current through the nanowire array or crosslinking the micelles) to increase the amount of control over chemical transformations. However, construction aspects will only ever be able to modulate bulk properties owing to their lack of atomistic definition.

Space, on the other hand, deals with *how* a substrate has access to a catalyst. Space is considered on much smaller terms than physical aspects are because with proper space control, you can also control orientation of substrate approach. Space can be easily affected by minor chemical changes, such as substituting a methyl group with a tert-butyl to force substrate orientation into a different direction. Space mainly encompasses shape limitations and is necessarily atomistic. In that way, space becomes very good for altering catalytic pathways by forcing alternate orientations.[25] Space is ultimately a fine tuning issue, and likely will require some aspect of trial and error for figuring out how to trim cavities, and what contributions small changes have on the final reaction outcome.

The one thing nature has been able to do quite well that humans haven't quite been able to match is combining structure and space effects in their catalysts. The scaffold of the cell membrane and the scaffold of the enzyme work synergistically to ensure only certain substrates have access to the active site. Cell membranes help with bulk diffusion and amino acids control the space around the active site. Active site control is so important that mutations in amino acid sequence rarely occurs close to the active site without detriment as those mutations would alter the space too much.[36] Future work in compartments needs to start taking a more critical look at how to incorporate both of structure and space together to closer mimic enzymatic catalysis.

5.4 Conclusion

True atomistic control over compartment space as is seen in enzymatic reactions has yet to be achieved, but that begs the question of if it ever needs to be. Enzymes are hyper specific in their

substrate scope which historically has not been important in chemistry. What has been important is gaining a basic understanding of reactivities of and how certain substrates can be manipulated. Since the molecular chemist can afford to employ much harsher conditions than nature can, the need for control over certain transformations doesn't exist. However, there is a green chemistry argument to be made in favor of compartmentalization. Namely, being able to create the same harsh condition – anoxic and water free environments – but on the nanoscale would lessen the amount of energy and environmental taxation required.

However, the barrier to entry for creating widely accessible synthetic systems that operate at the nanoscale are currently too high. As a consequence of how much effort needs to be put into creating a compartment, confinement chemistry currently only has two practical uses: altering reactivities and niche industrial applications. For the synthetic research chemist, being able to alter the energetics of catalytic pathways to reach different products will always be inherently interesting. But unfortunately, the vast portion of confinement research only considers discrimination between substrates and not changing catalytic pathways. Steric properties that alter pathways exist on the angstrom scale, but when the space of a compartment has to be designed to that precision, substrate scope becomes limited. Therefore, as a grand solution, we ultimately only see confinement as an answer to large industrial problems. A lot of effort needs to be put into designing compartments for catalytic problems, yet as long as fabrication techniques aren't that harsh, confinement can introduce new or greener ways to make certain compounds. If research efforts are going to be placed on creating novel confined systems, the systems made need to be designed with specific end goals in mind rather than mere investigations of the effects small changes have.

Going back to the premise that this perspective as well as many other catalyst papers start with (and often fail to mention again), our collective goal is to achieve biomimetic systems. At some point, biomimicry is a buzz word. If that's the true goal, the papers that mention achieving bio-like levels of catalysis would be enzyme papers. The real goal shouldn't be to mimic biology, but rather to create something that biology can't even come close to achieving. Confinement of catalysts needs to be done with a purpose. Hopefully, we have been able to shed some light on what to think about when creating compartments such as their physical structure and the space the catalyst sits in and are able to provide some directionality to the field on where the chemistry should go in the future.

5.5 References

(1) Leenders, S. H. A. M.; Gramage-Doria, R.; De Bruin, B.; Reek, J. N. H. Transition metal catalysis in confined spaces. *Chem. Soc. Rev.* **2015**, *44* (2), 433-448.

(2) Fang, Y.; Powell, J. A.; Li, E. R.; Wang, Q.; Perry, Z.; Kirchon, A.; Yang, X. Y.; Xiao, Z. F.; Zhu, C. F.; Zhang, L. L.; et al. Catalytic reactions within the cavity of coordination cages. *Chem. Soc. Rev.* **2019**, *48* (17), 4707-4730.

(3) Catti, L.; Zhang, Q.; Tiefenbacher, K. Advantages of Catalysis in Self-Assembled Molecular Capsules. *Chem. Eur. J.* **2016**, *22* (27), 9060-9066.

(4) Grommet, A. B.; Feller, M.; Klajn, R. Chemical reactivity under nanoconfinement. *Nat. Nanotechnol.* **2020**, *15* (4), 256-271.

(5) Kumar, B. S.; Pitchumani, K. Chemistry in Confinement: Copper and Palladium Catalyzed Ecofriendly Organic Transformations within Porous Frameworks. *Chem. Rec.* **2018**, *18* (5), 506-526.

(6) Fei, X. Q.; Wang, P. L.; Zhang, D. S.; Wang, H. Q.; Wu, Z. B. Confined Catalysts Application in Environmental Catalysis: Current Research Progress and Future Prospects. *Chemcatchem* **2021**, *13* (10), 2313-2336.

(7) Liu, W. Q.; Stoddart, J. F. Emergent behavior in nanoconfined molecular containers. *Chem* **2021**, *7* (4), 919-947.

(8) Jongkind, L. J.; Caumes, X.; Hartendorp, A. P. T.; Reek, J. N. H. Ligand Template Strategies for Catalyst Encapsulation. *Acc. Chem. Res.* **2018**, *51* (9), 2115-2128.

(9) Nemethova, I.; Syntrivanis, L. D.; Tiefenbacher, K. Molecular Capsule Catalysis: Ready to Address Current Challenges in Synthetic Organic Chemistry? *Chimia* **2020**, *74* (7-8), 561-568.

(10) De Martino, M. T.; Abdelmohsen, L.; Rutjes, F.; van Hest, J. C. M. Nanoreactors for green catalysis. *Beilstein J. Org. Chem.* **2018**, *14*, 716-733.

(11) Poli, R. *Site Isolation for Non-orthogonal Tandem Catalysis in Confined Nanospaces*; 2017. DOI: 10.1007/978-3-319-50207-6_9.

(12) Otte, M. Size-Selective Molecular Flasks. *ACS Catal.* **2016**, *6* (10), 6491-6510.

(13) Gaeta, C.; La Manna, P.; De Rosa, M.; Soriente, A.; Talotta, C.; Neri, P. Supramolecular Catalysis with Self-Assembled Capsules and Cages: What Happens in Confined Spaces. *Chemcatchem* **2021**, *13* (7), 1638-1658.

(14) Jolly, B. J.; Co, N. H.; Davis, A. R.; Diaconescu, P. L.; Liu, C. A generalized kinetic model for compartmentalization of organometallic catalysis. *Chem. Sci.* **2022**, *13* (4), 1101-1110.

(15) Natinsky, B. S.; Lu, S.; Copeland, E. D.; Quintana, J. C.; Liu, C. Solution Catalytic Cycle of Incompatible Steps for Ambient Air Oxidation of Methane to Methanol. *ACS Cent. Sci.* **2019**, *5* (9), 1584-1590.

(16) Natinsky, B. S.; Jolly, B. J.; Dumas, D. M.; Liu, C. Efficacy analysis of compartmentalization for ambient CH4 activation mediated by a RhII metalloradical in a nanowire array electrode. *Chem. Sci.* **2021**, *12* (5), 1818-1825.

(17) Jolly, B. J.; Co, N. H.; Davis, A. R.; Diaconescu, P. L.; Liu, C. A generalized kinetic model for compartmentalization of organometallic catalysis. *Chem. Sci.* **2022**.

(18) Liu, Y.; Wang, Y.; Wang, Y.; Lu, J.; Piñón, V.; Weck, M. Shell Cross-Linked Micelle-Based Nanoreactors for the Substrate-Selective Hydrolytic Kinetic Resolution of Epoxides. *J. Am. Chem. Soc.* **2011**, *133* (36), 14260-14263.

(19) Rossbach, B. M.; Leopold, K.; Weberskirch, R. Self-Assembled Nanoreactors as Highly Active Catalysts in the Hydrolytic Kinetic Resolution (HKR) of Epoxides in Water. *Angew. Chem. Int. Ed.* **2006**, *45* (8), 1309-1312.

(20) Lee, S. J.; Cho, S.-H.; Mulfort, K. L.; Tiede, D. M.; Hupp, J. T.; Nguyen, S. T. Cavity-Tailored, Self-Sorting Supramolecular Catalytic Boxes for Selective Oxidation. *J. Am. Chem. Soc.* **2008**, *130* (50), 16828-16829.

(21) Tugny, C.; del Rio, N.; Koohgard, M.; Vanthuyne, N.; Lesage, D.; Bijouard, K.; Zhang, P. L.; Suarez, J. M.; Roland, S.; Derat, E.; et al. beta-Cyclodextrin-NHC-Gold(I) Complex (beta-ICyD)AuCl: A Chiral Nanoreactor for Enantioselective and Substrate-Selective Alkoxycyclization Reactions. *ACS Catal.* **2020**, *10* (11), 5964-5972.

(22) Zhang, P. L.; Suarez, J. M.; Driant, T.; Derat, E.; Zhang, Y. M.; Menand, M.; Roland, S.; Sollogoub, M. Cyclodextrin Cavity-Induced Mechanistic Switch in Copper-Catalyzed Hydroboration. *Angew. Chem. Int. Ed.* **2017**, *56* (36), 10821-10825.

(23) Collman, J. P.; Zhang, X.; Hembre, R. T.; Brauman, J. I. Shape-selective olefin epoxidation catalyzed by manganese picnic basket porphyrins. *J. Am. Chem. Soc.* **1990**, *112* (13), 5356-5357.

(24) Collman, J. P.; Brauman, J. I.; Fitzgerald, J. P.; Hampton, P. D.; Naruta, Y.; Michida, T. Manganese “Picnic Basket” Porphyrins: Cytochrome P-450 Active Site Analogues. *Bull. Chem. Soc. Jpn.* **1988**, *61* (1), 47-57.

(25) Bocokić, V.; Kalkan, A.; Lutz, M.; Spek, A. L.; Gryko, D. T.; Reek, J. N. H. Capsule-controlled selectivity of a rhodium hydroformylation catalyst. *Nat. Commun.* **2013**, *4* (1).

(26) Gallego, E. M.; Portilla, M. T.; Paris, C.; León-Escamilla, A.; Boronat, M.; Moliner, M.; Corma, A. Ab initio synthesis of zeolites for preestablished catalytic reactions. *Science* **2017**, *355* (6329), 1051-1054.

(27) Chen, L.; Jiang, Y.; Huo, H.; Liu, J.; Li, Y.; Li, C.; Zhang, N.; Wang, J. Metal-organic framework-based composite Ni@MOF as Heterogenous catalyst for ethylene trimerization. *Applied Catalysis A: General* **2020**, *594*, 117457.

(28) Liu, J.; Ye, J.; Li, Z.; Otake, K.-I.; Liao, Y.; Peters, A. W.; Noh, H.; Truhlar, D. G.; Gagliardi, L.; Cramer, C. J.; et al. Beyond the Active Site: Tuning the Activity and Selectivity of a Metal–Organic Framework-Supported Ni Catalyst for Ethylene Dimerization. *J. Am. Chem. Soc.* **2018**, *140* (36), 11174-11178.

(29) Freund, R.; Zaremba, O.; Arnauts, G.; Ameloot, R.; Skorupskii, G.; Dincă, M.; Bavykina, A.; Gascon, J.; Ejsmont, A.; Goscianska, J.; et al. The Current Status of MOF and COF Applications. *Angew. Chem. Int. Ed.* **2021**, *60* (45), 23975-24001.

(30) Windle, C. L.; Simmons, K. J.; Ault, J. R.; Trinh, C. H.; Nelson, A.; Pearson, A. R.; Berry, A. Extending enzyme molecular recognition with an expanded amino acid alphabet. *Proceedings of the National Academy of Sciences* **2017**, *114* (10), 2610-2615.

(31) Torque, C.; Sueur, B.; Cabou, J.; Bricout, H.; Hapiot, F.; Monflier, E. Substrate-selective aqueous organometallic catalysis. How small water-soluble organic molecules enhance the supramolecular discrimination. *Tetrahedron* **2005**, *61* (20), 4811-4817.

(32) Zhang, P. L.; Tugny, C.; Suarez, J. M.; Guitet, M.; Derat, E.; Vanthuyne, N.; Zhang, Y. M.; Bistri, O.; Mouries-Mansuy, V.; Menand, M.; et al. Artificial Chiral Metallo-pockets Including a Single Metal Serving as Structural Probe and Catalytic Center. *Chem* **2017**, *3* (1), 174-191.

(33) Molnar, A. Synthetic Application of Cyclodextrins in Combination with Metal Ions, Complexes, and Metal Particles. *Chemcatchem* **2021**, *13* (6), 1424-1474.

(34) Chen, Z.; Cui, Z.-M.; Li, P.; Cao, C.-Y.; Hong, Y.-L.; Wu, Z.-Y.; Song, W.-G. Diffusion Induced Reactant Shape Selectivity Inside Mesoporous Pores of Pd@meso-SiO2 Nanoreactor in Suzuki Coupling Reactions. *J. Chem. Phys. C* **2012**, *116* (28), 14986-14991.

(35) Chen, Z.; Cui, Z.-M.; Niu, F.; Jiang, L.; Song, W.-G. Pd nanoparticles in silica hollow spheres with mesoporous walls: a nanoreactor with extremely high activity. *Chem. Commun.* **2010**, *46* (35), 6524.

(36) Valencia, A.; Chardin, P.; Wittinghofer, A.; Sander, C. The ras protein family: evolutionary tree and role of conserved amino acids. *Biochemistry* **1991**, *30* (19), 4637-4648.

APPENDIX: SUPPLEMENTARY INFORMATION

Chapter 2

Tables

Table S1. Control homopolymerization reactions.

Entry	Condition[a]	Monomer[b]	Time (h)	T (°C)	Conv. (%)	$M\text{n}_{calc}$ (kg/mol)[c]	$M\text{n}_{exp}$ (kg/mol)[d]	$Đ$[d]
1	**red**	styrene	24	80	26	N/D[e]	N/D[e]	N/D[e]
2	**ox**	styrene	0.1	RT	98	N/D[e]	N/D[e]	N/D[e]
3	**red**	*p*-CS	24	80	87	N/D[e]	N/D[e]	N/D[e]
4	**ox**	*p*-CS	24	RT	>99	N/D[e]	N/D[e]	N/D[e]
5	**red**	MMA	24	80	NR	-	-	-
6	**ox**	MMA	24	RT	NR	-	-	-
7	**red**	*n*-BuMA	24	80	NR	-	-	-
8	**ox**	*n*-BuMA	24	RT	NR	-	-	-
9	**red**	acrylonitrile	24	80	NR	-	-	-
10	**ox**	acrylonitrile	24	RT	NR	-	-	-
11	**oxi**	styrene	24	RT	NR	-	-	-
12	**oxi**	*p*-CS	24	RT	NR	-	-	-
13	**oxi**	MMA	24	RT	NR	-	-	-
14	**oxi**	*n*-BuMA	24	RT	NR	-	-	-

Conditions: monomer (1.05 mmol), 1, 3, 5-trimethoxybenzene (TMB) as an internal standard (0.1167 mmol), $FcBAr^F$ as the oxidant (0.0111 mmol), and C_6D_6 and *o*-difluorobenzene as the solvent (a total volume of 0.5 mL); [a] "**red**" and "**ox**" refer to the reduced and *in situ* generated oxidized compound ($fc^{P,B}$)NiBr (0.0111 mmol) in the absence of ethyl 2-bromoisobutyrate, "**oxi**" refers to experiments with $FcBAr^F$ and ethyl 2-bromoisobutyrate (0.0111 mmol) but no ($fc^{P,B}$)NiBr. [b] *p*-CS = *p*-chlorostyrene, MMA = methyl methacrylate, *n*-BuMA = *n*-butyl methacrylate. [c] Determined by ^{1}H NMR spectroscopy. [d] Determined by SEC. [e] Not determined, polymer could not be isolated suggesting formation of oligomers.

Table S2. Failed copolymerization attempts using ($fc^{P,B}$)NiBr and its oxidized counterpart.

Entry	Monomer 1[a]	Monomer 2	Monomer 3	Catalyst[b]	Time (h)	Conv. (%)
1	styrene	*n*-BuMA	/	**ox-red**	0.2-42	99-62
2	*n*-BuMA	styrene	/	**red-ox**	22-2.5	86-99
3	*p*-CS	MMA	/	**red-ox**	46-22	96-0
4	*n*-BuMA	MMA	/	**red-ox**	22-28	86-75
5	styrene	*p*-CS	styrene	**ox-red-ox**	0.2-46-24	99-18-92

Conditions: monomer (1.05 mmol), ethyl 2-bromoisobutyrate (0.0111 mmol), ($fc^{P,B}$)NiBr (0.0111 mmol), (1, 3, 5-trimethoxybenzene (TMB) as an internal standard (0.1167 mmol), $FcBAr^F$ as oxidant (0.0111 mmol), $CoCp_2$ as reductant (0.0111 mmol), and C_6D_6 and difluorobenzene as solvent. Reaction temperatures were based on homopolymer studies, unless otherwise mentioned. [a] *n*-BuMA = *n*-butyl methacrylate, MMA = methyl methacrylate, *p*-CS = *p*-chlorostyrene [b] "**red**" and "**ox**" refer to the reduced and *in situ* generated oxidized compound.

Conversion plots

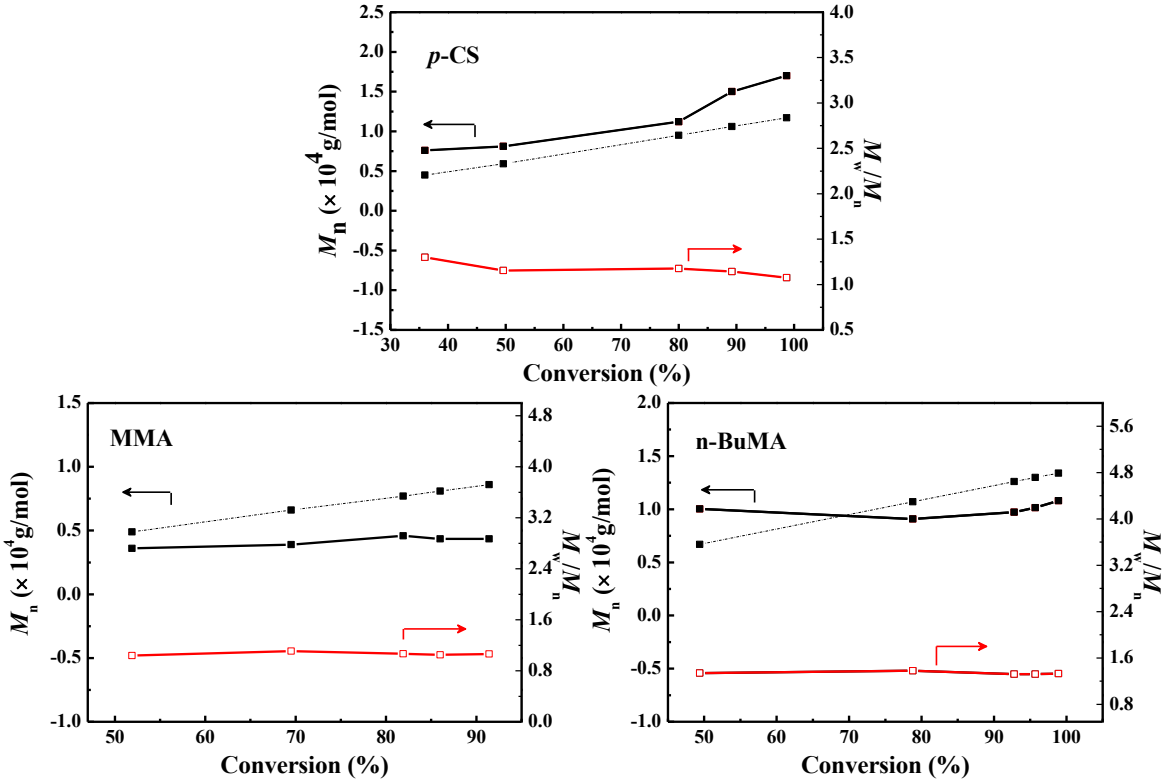

Figure S1. Conversion dependence of M_n and M_w/M_n for *p*-CS, MMA, and *n*-BuMA polymerization with ($fc^{P,B}$)NiBr or [($fc^{P,B}$)NiBr][BAr^F]. The black lines use the y axis at left and red line with right, as the arrows indicate; the dotted line is for the theoretical M_n.

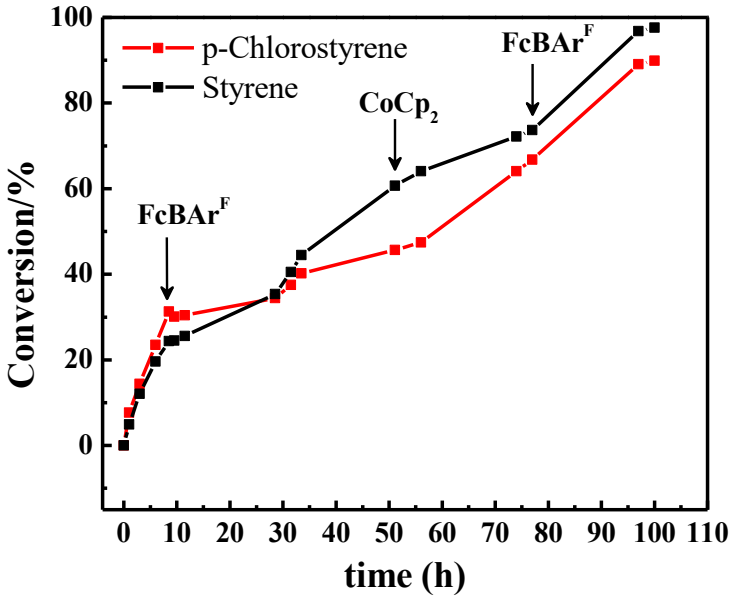

Figure S2. Plot of conversion (%) vs time for the polymerization of styrene and p-CS by one-pot with ($fc^{P,B}$)NiBr using *in situ* oxidation and reduction with $FcBAr^F$ and $CoCp_2$, respectively.

DOSY

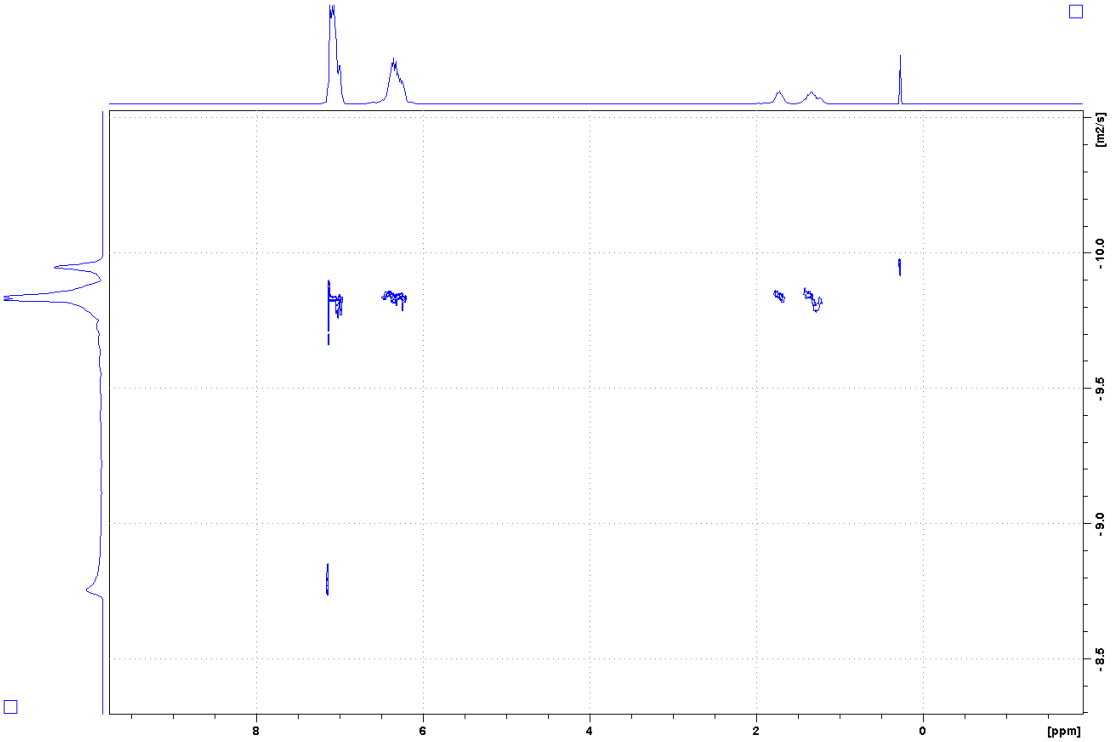

Figure S3. DOSY (500 MHz, 25°C, $CDCl_3$) of PCS-PS copolymer (Table 2, entry 2).

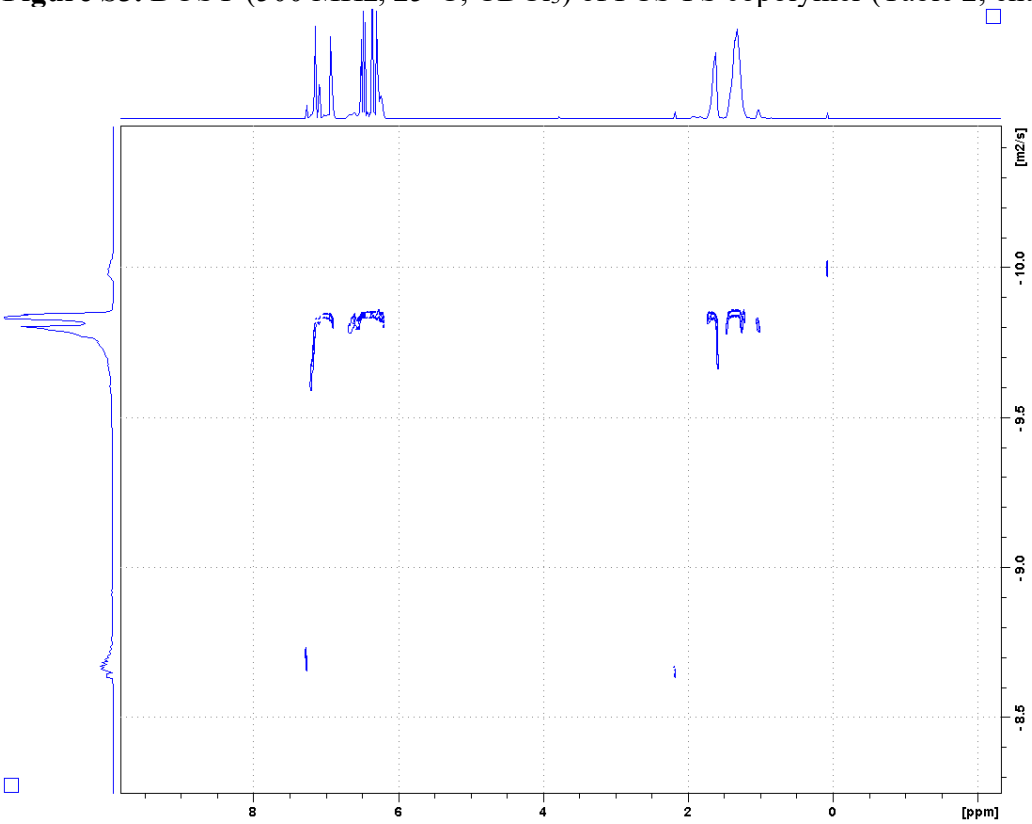

Figure S4. DOSY (500 MHz, 25°C, $CDCl_3$) of PS-PCS copolymer (Table 2, entry 4).

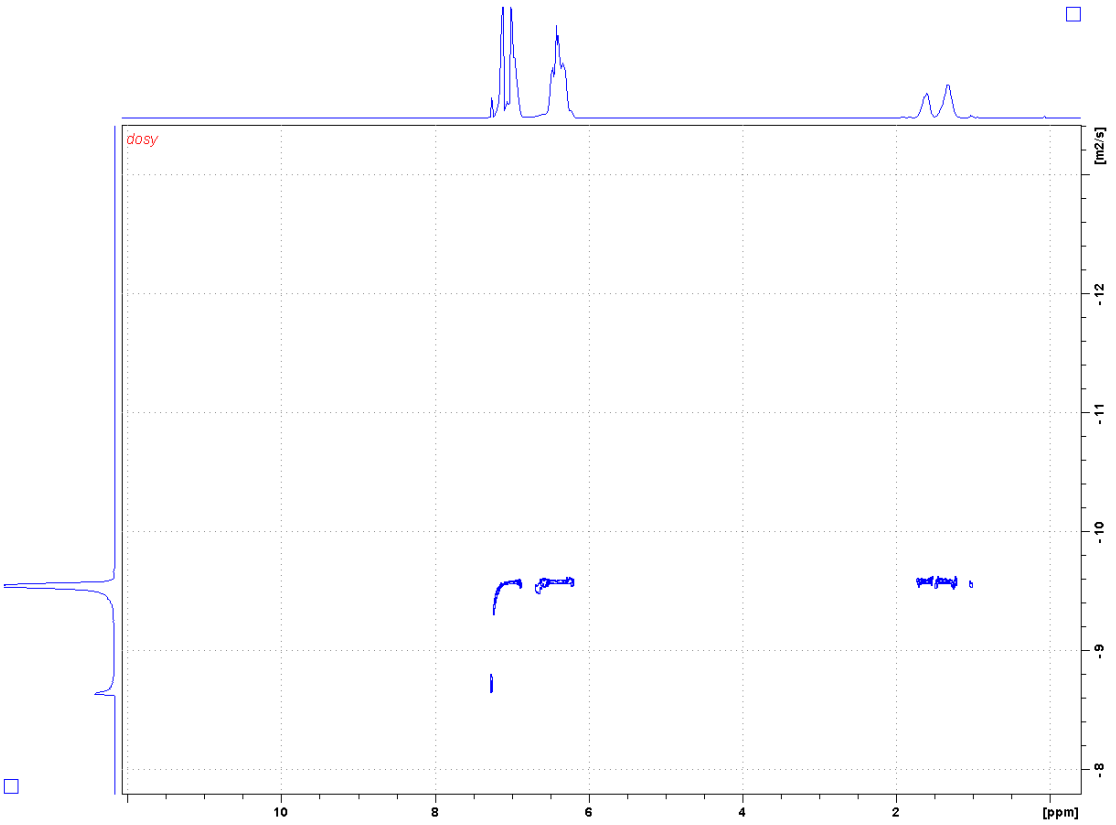

Figure S5. DOSY (500 MHz, 25°C, $CDCl_3$) of PCS-PS-PCS copolymer (Table 2, entry 5).

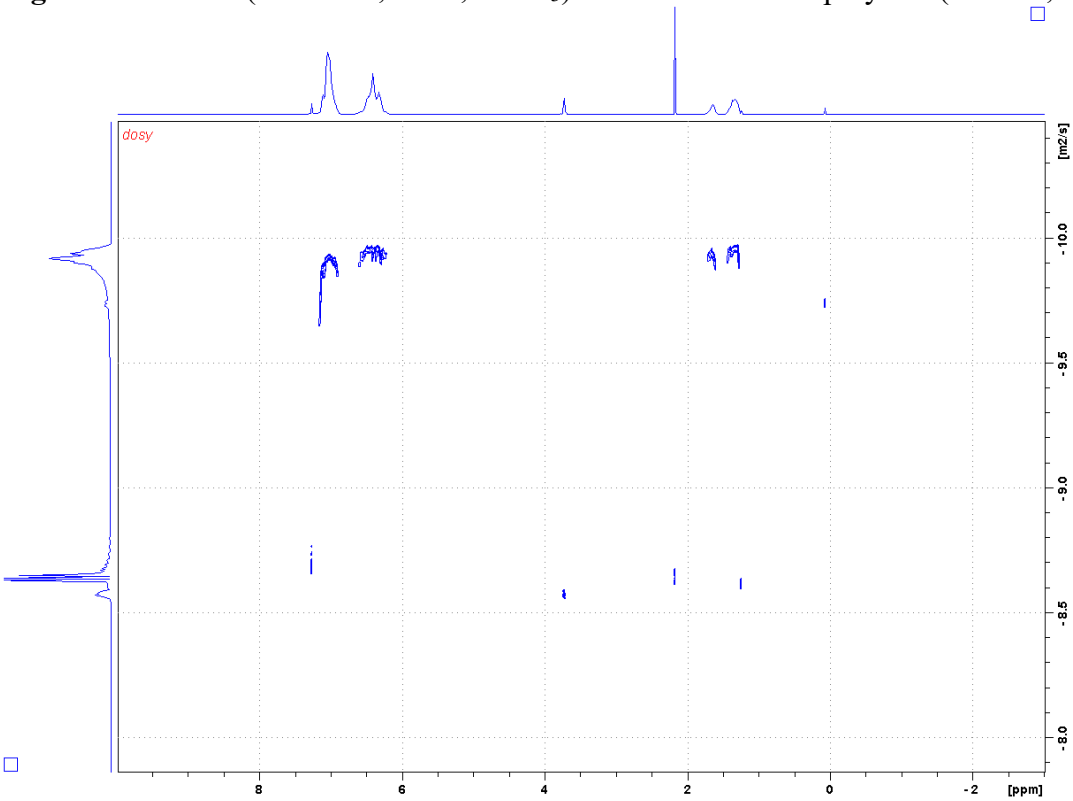

Figure S6. DOSY (500 MHz, 25°C, $CDCl_3$) of PS-PCS-PS copolymer (Table S2, entry 5).

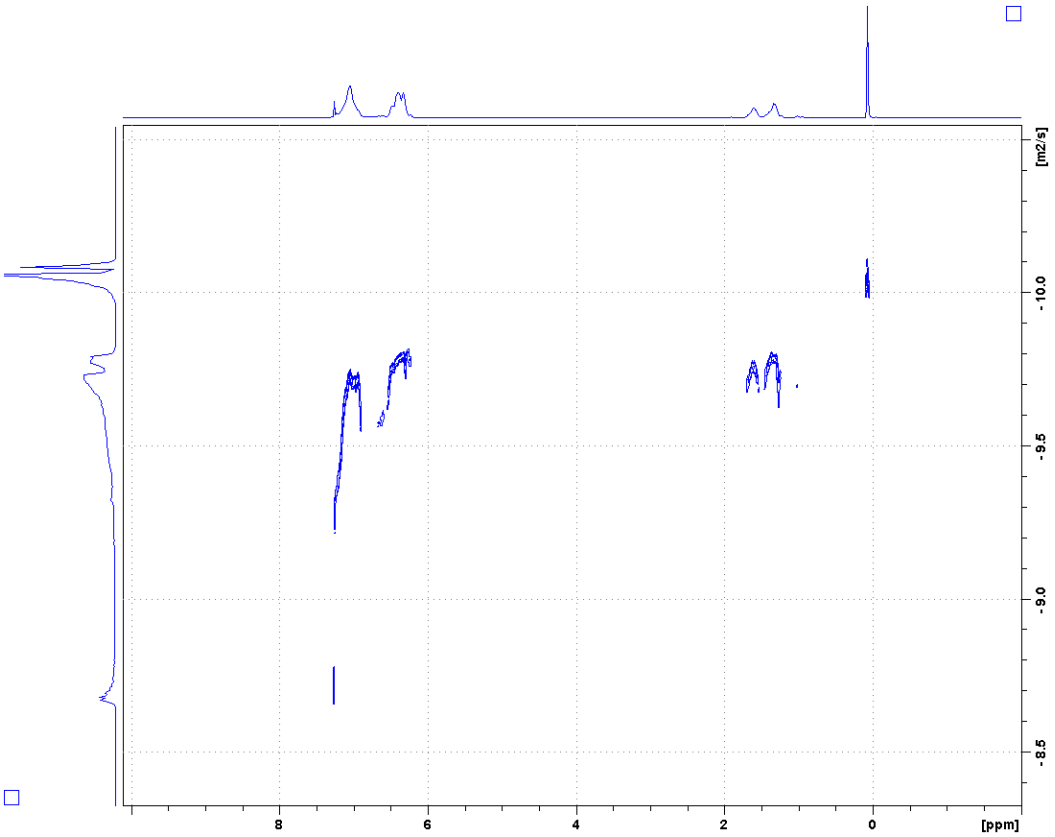

Figure S7. DOSY (500 MHz, 25°C, $CDCl_3$) of a mixture of PCS and PS homopolymers.

Stejskal-Tanner plots

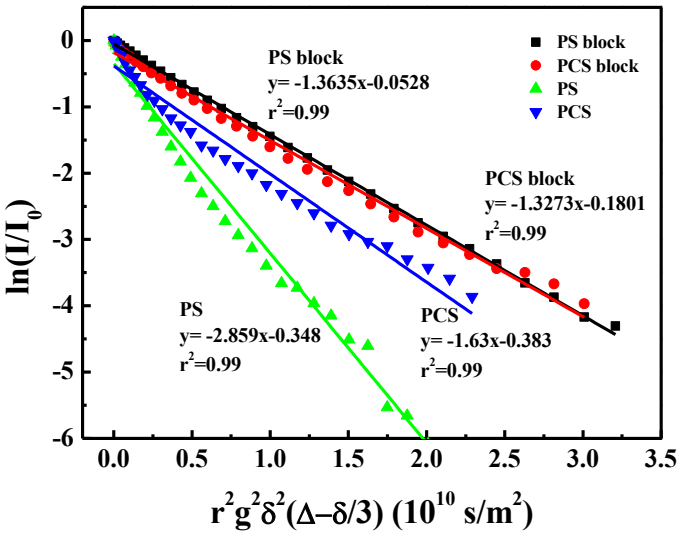

Figure S8. Stejskal-Tanner plot of the diffusion activity of the PS and PCS blocks in PS-PCS copolymer compared to the PS and PCS homopolymers (Table 2, entries 1-3).

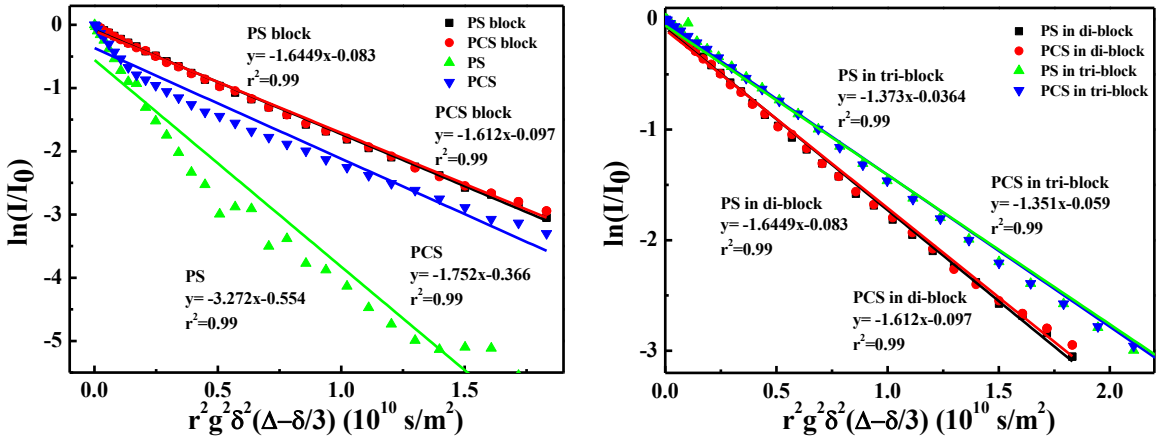

Figure S9. Stejskal-Tanner plot of the diffusion activity of the PCS and PS blocks in a PCS-PS copolymer compared to PCS and PS homopolymers (left) and of the diffusion activity of the PCS and PS blocks in PCS-PS-PCS compared to those blocks in PCS-PS (right).

NMR spectra

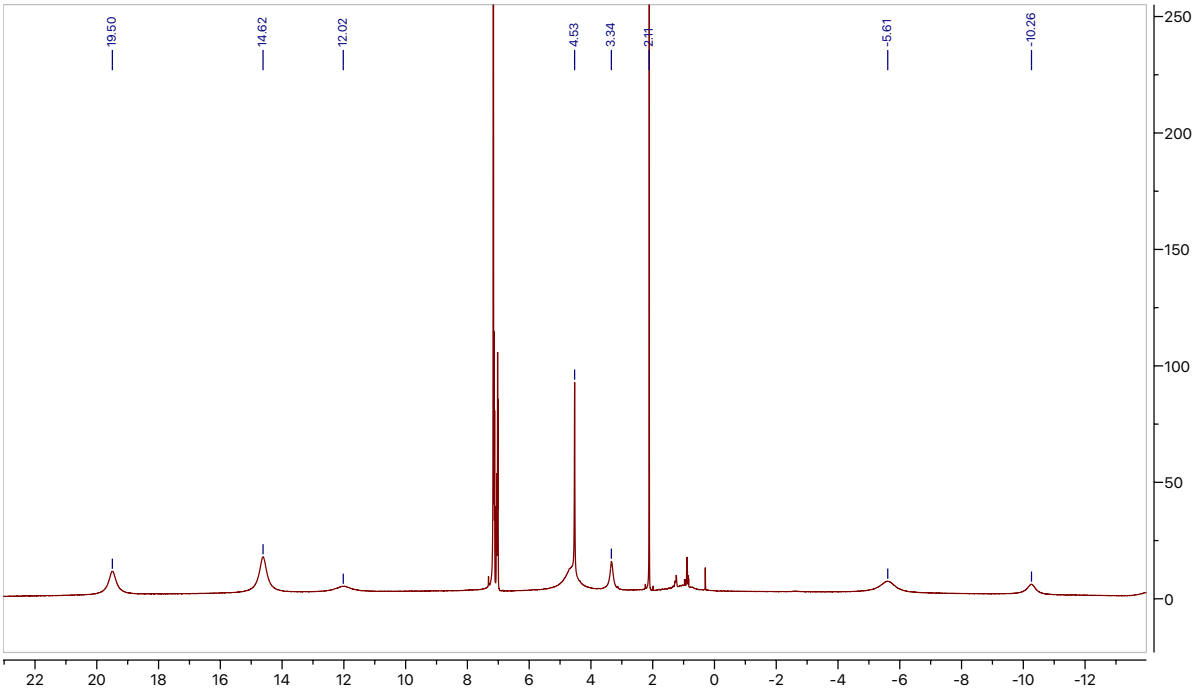

Figure S10. ^{1}H NMR (500 MHz, 25 °C, C_6D_6) spectrum of ($fc^{P,B}$)NiBr·(C_7H_8). δ (ppm): 19.50 (s,br), 14.62 (s, br), 12.02 (s, br), 4.53(s), 3.34 (s, br), -5.61 (s, br), -10.26 (s, br). Peaks at 7.13 ppm, 7.02 ppm, and 2.11 ppm are attributed to residual toluene.

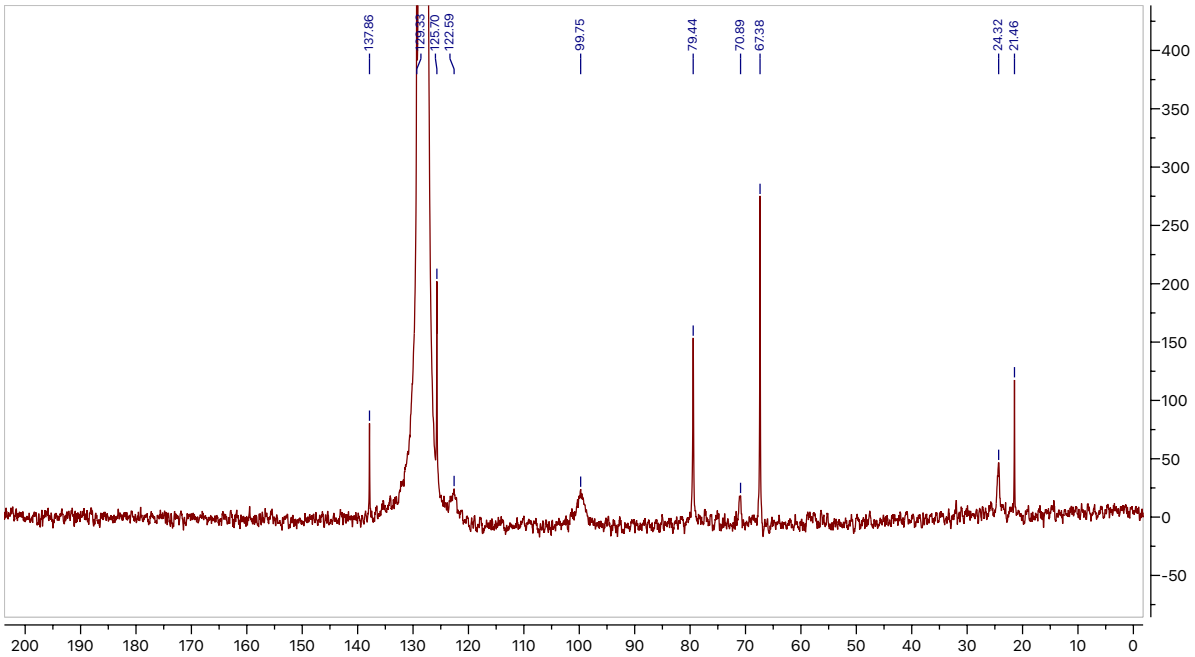

Figure S11. ^{13}C NMR spectrum (126 MHz, 25 °C, C_6D_6) of ($fc^{P,B}$)NiBr: δ (ppm) 125.70 (s, aromatic) 122.59 (s, br, aromatic), 99.75(s, br, CH), 79.44 (s, Cp-*C*), 70.89 (s, br, Cp-*C*), 67.38 (s, Cp-*C*), 24.32 (s, br, C*C*H$_3$). Peaks at 137.86 ppm, 129.33 ppm, 125.70, and 21.46 ppm are attributed to residual toluene.

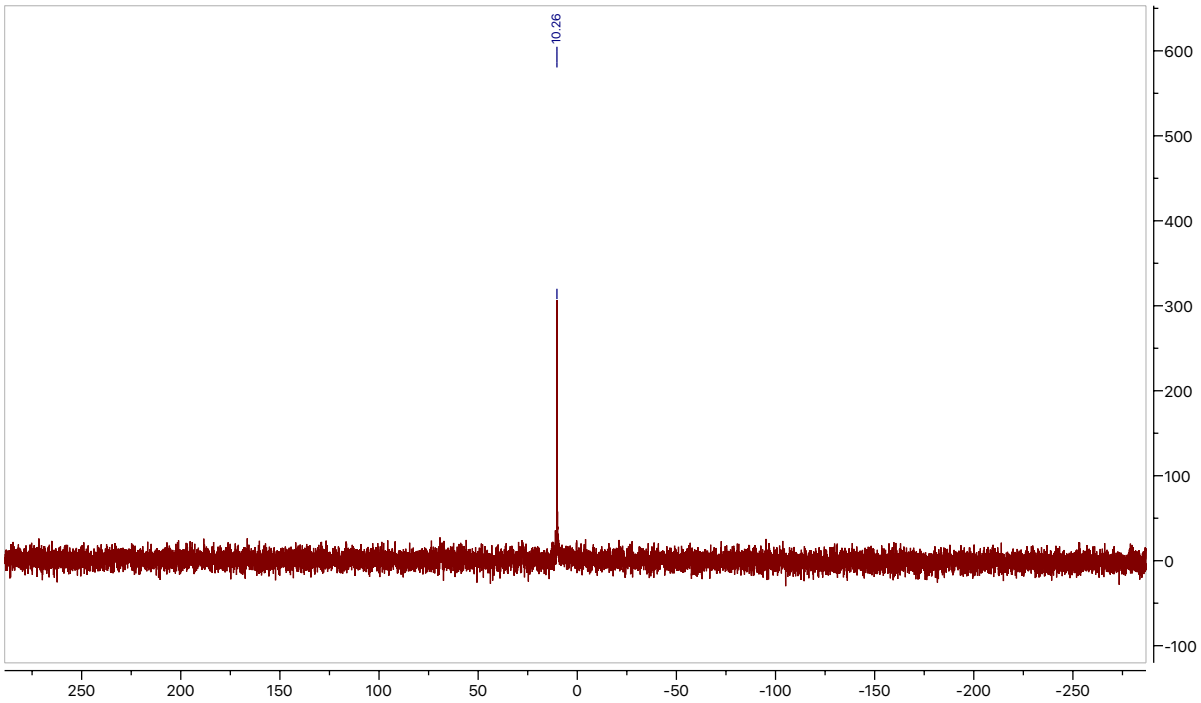

Figure S12. ^{31}P NMR spectrum (121 MHz, 25 °C, C_6D_6) spectrum of ($fc^{P,B}$)NiBr: δ (ppm) 10.26 (s).

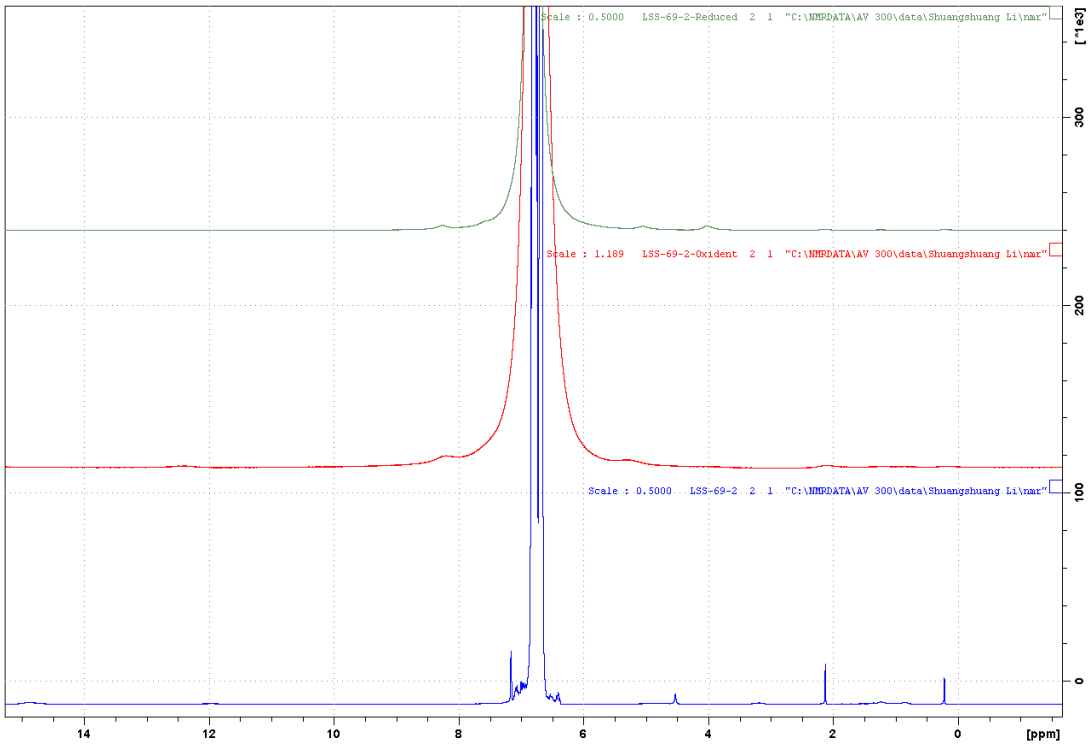

Figure S13. ^1H NMR (300 MHz, 25 °C, C_6D_6) spectrum of *in situ* redox switching of ($fc^{P,B}$)NiBr. We have ($fc^{P,B}$)NiBr (bottom), [($fc^{P,B}$)NiBr][BAr^F] after adding oxidant $FcBAr^F$ (middle), and regenerated ($fc^{P,B}$)NiBr after adding reductant $CoCp_2$ (top).

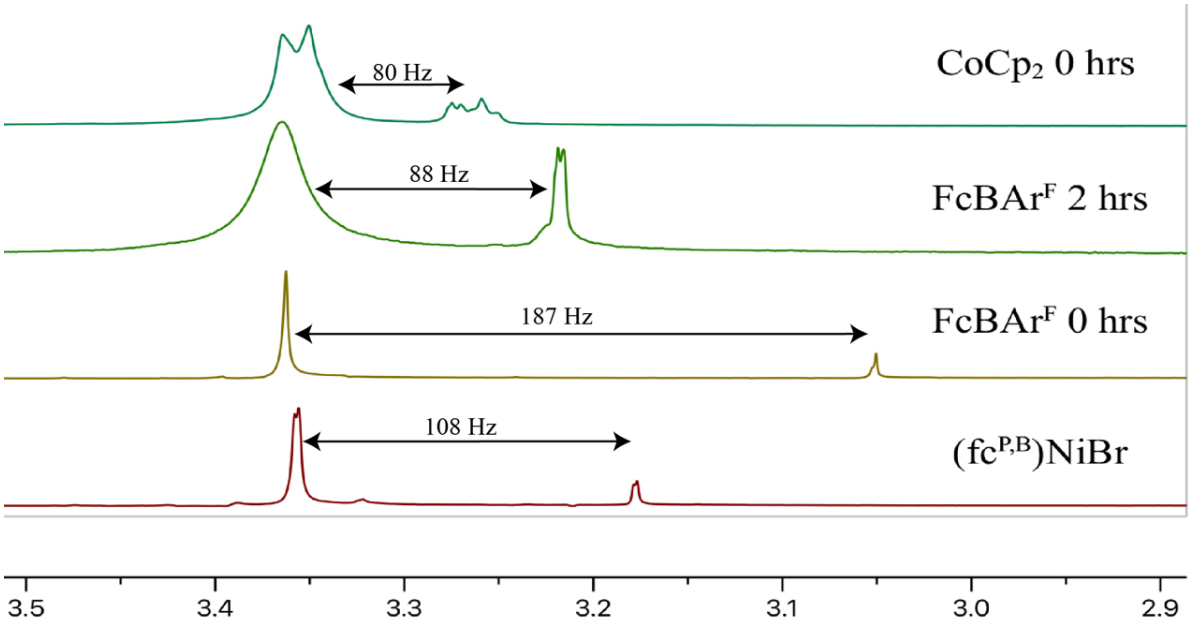

Figure S14. ^{1}H NMR (600 MHz, 25°C, 1:1 DFB:C_6D_6) solution state magnetic susceptibility study of *in situ* redox switching of ($fc^{P,B}$)NiBr. Referenced using 5% (w/v) TMB solution in 1:1 DFB:C_6D_6. δ (ppm): 3.36 (s, 3H, OCH_3, TMB inside sealed capillary) 3.25-3.04 (s, 3H, OCH_3, TMB in solution with ($fc^{P,B}$)NiBr).

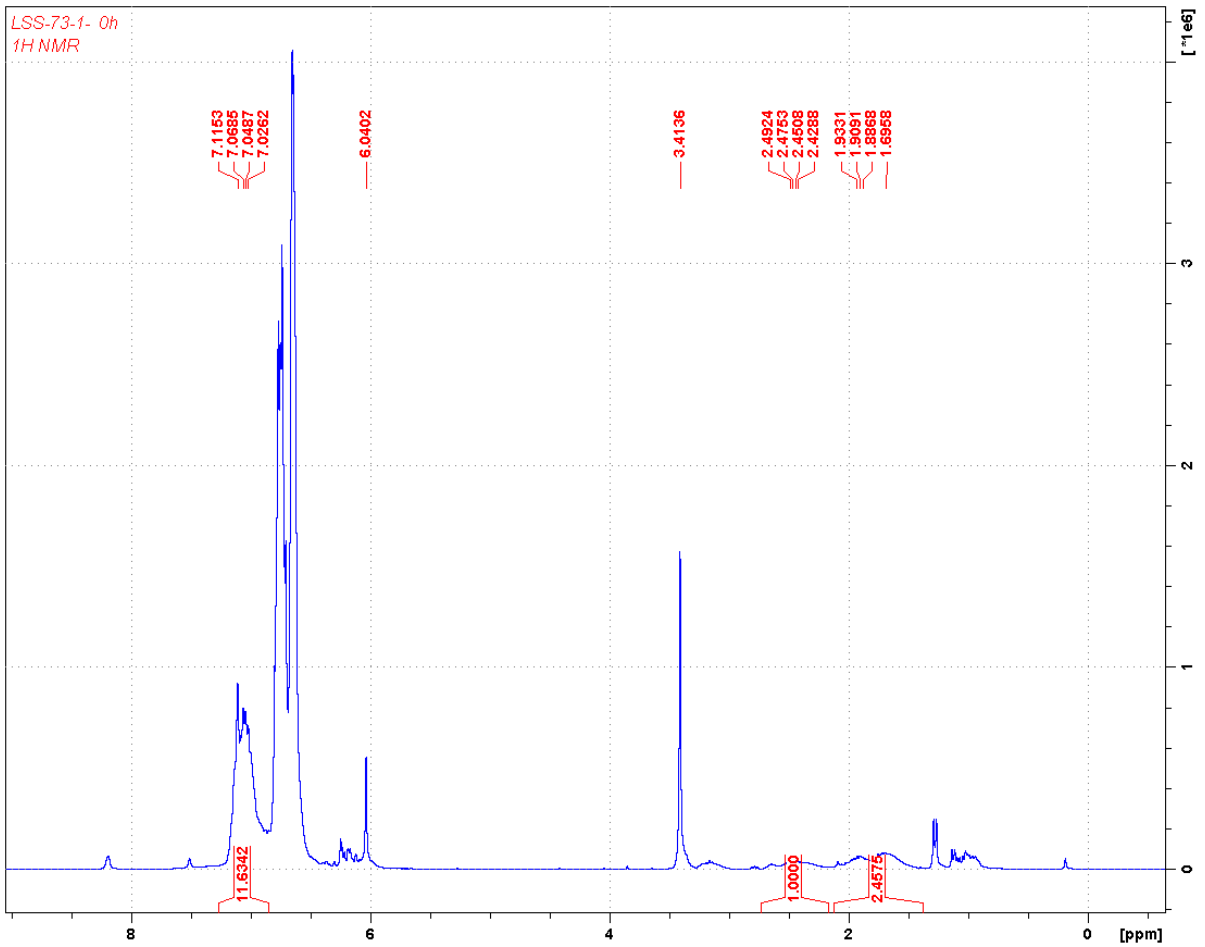

Figure S15. ^{1}H NMR (500 MHz, 25°C, C_6D_6) spectrum of 100 equivalents of styrene polymerization by [($fc^{P,B}$)NiBr][BAr^{F}] (Table 1, entry 2). δ (ppm): 7.02 (m, 5H, ArH, PS), 6.46-6.85 (m, 4H, 1,2-difluorobenzene), 6.04 (s, 3H, TMB), 3.41 (s, 9H, OCH_3, TMB), 2.45 (br t, 1H, C*H*CH_2, PS), 1.88 (br d, 2H, CHC*H*$_2$, PS).

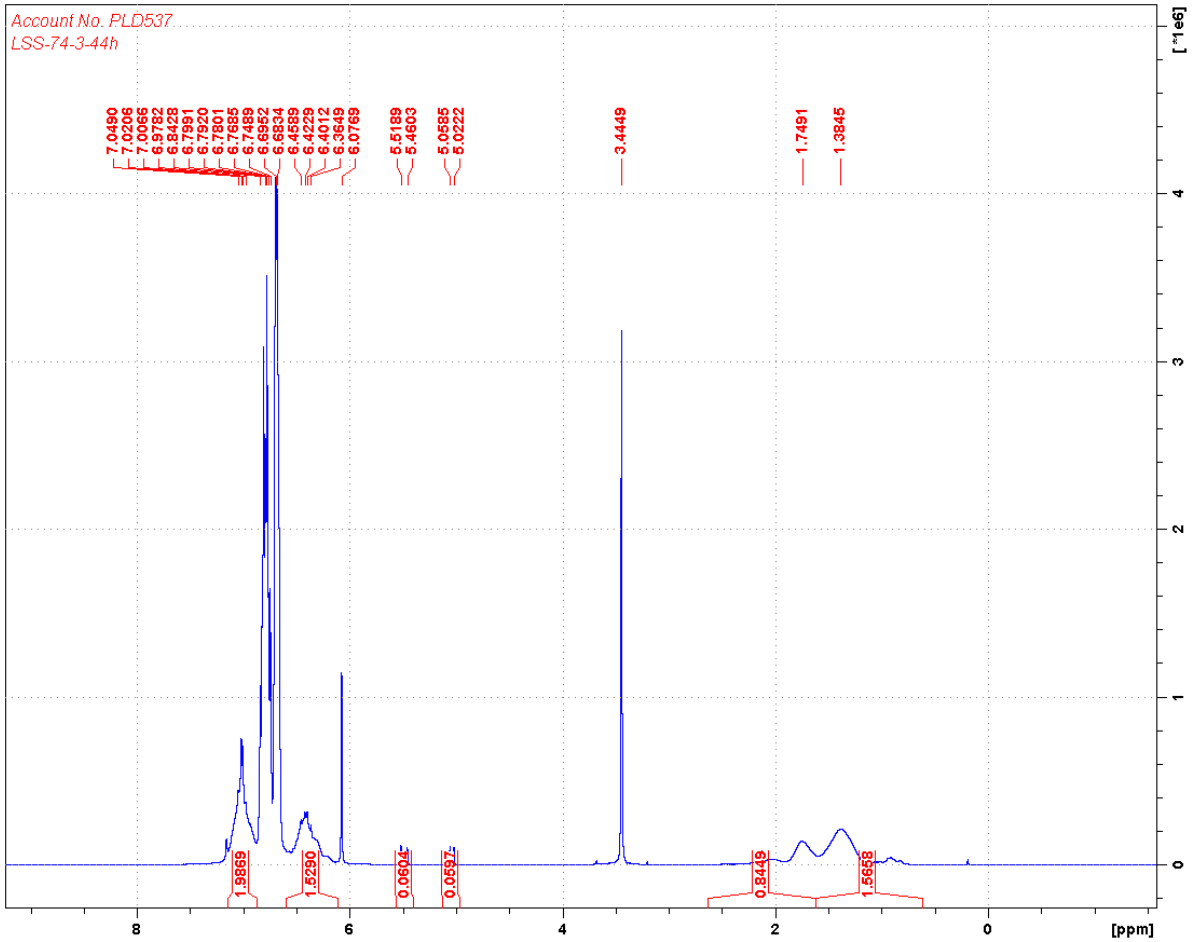

Figure S16. ^{1}H NMR (500 MHz, 25°C, C_6D_6) spectrum of 100 equivalents of *p*-chlorostyrene polymerization by ($fc^{P,B}$)NiBr (Table 1, entry 4). δ (ppm): 7.02 (m, 2H, ArH, PCS), 6.58-6.89 (m, 4H, 1,2-difluorobenzene), 6.42 (m, 2H, ArH, PCS), 6.07 (s, 3H, TMB), 5.50 (d, 1H, CHC*H*$_2$, p-CS), 5.05 (d, 1H, CHC*H*$_2$, p-CS), 3.44 (s, 9H, OCH_3, TMB), 1.75 (br t, 1H, C*H*CH_2, PCS), 1.38 (br d, 2H, CHC*H*$_2$, PCS).

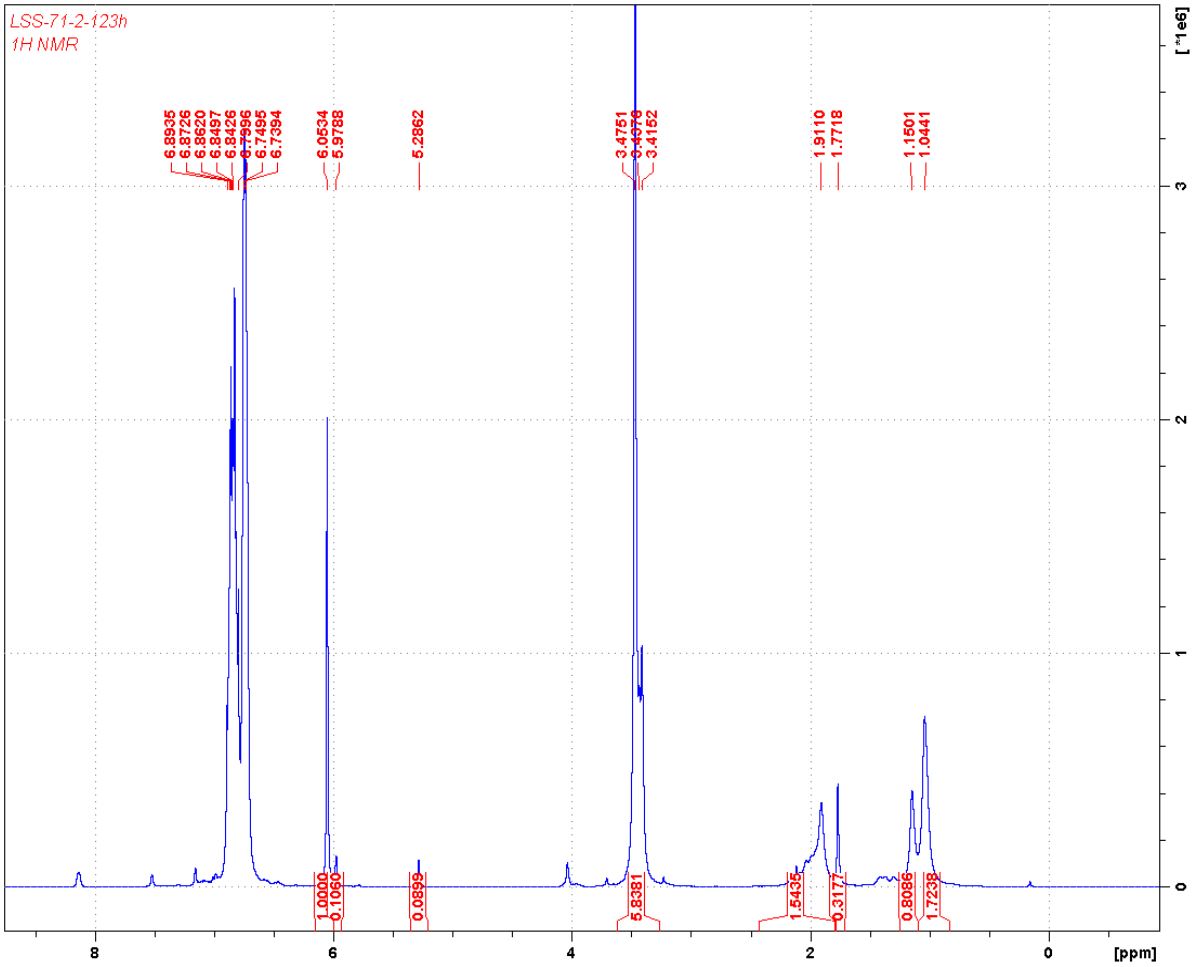

Figure S17. ^{1}H NMR (500 MHz, 25°C, C_6D_6) spectrum of 100 equivalents of methyl methacrylate polymerization by [(fc^{P,B})NiBr][BAr^{F}] (Table 1, entry 6). δ (ppm): 6.53-6.89 (m, 4H, 1,2-difluorobenzene), 6.05 (s, 3H, TMB), 5.98 (s, 1H, C*H*$_2$CCH$_3$, MMA), 5.29 (s, 1H, C*H*$_2$CCH$_3$, MMA), 3.47 (s, 9H, OCH$_3$, TMB), 3.44 (s, 3H, OCH$_3$, MMA), 3.42 (br s, 3H, OCH$_3$, PMMA), 1.91 (br s, 3H, CCH$_3$, PMMA), 1.77 (s, 3H, CH$_2$CC*H*$_3$, MMA), 1.04 (br s, 2H, CCH$_2$, PMMA).

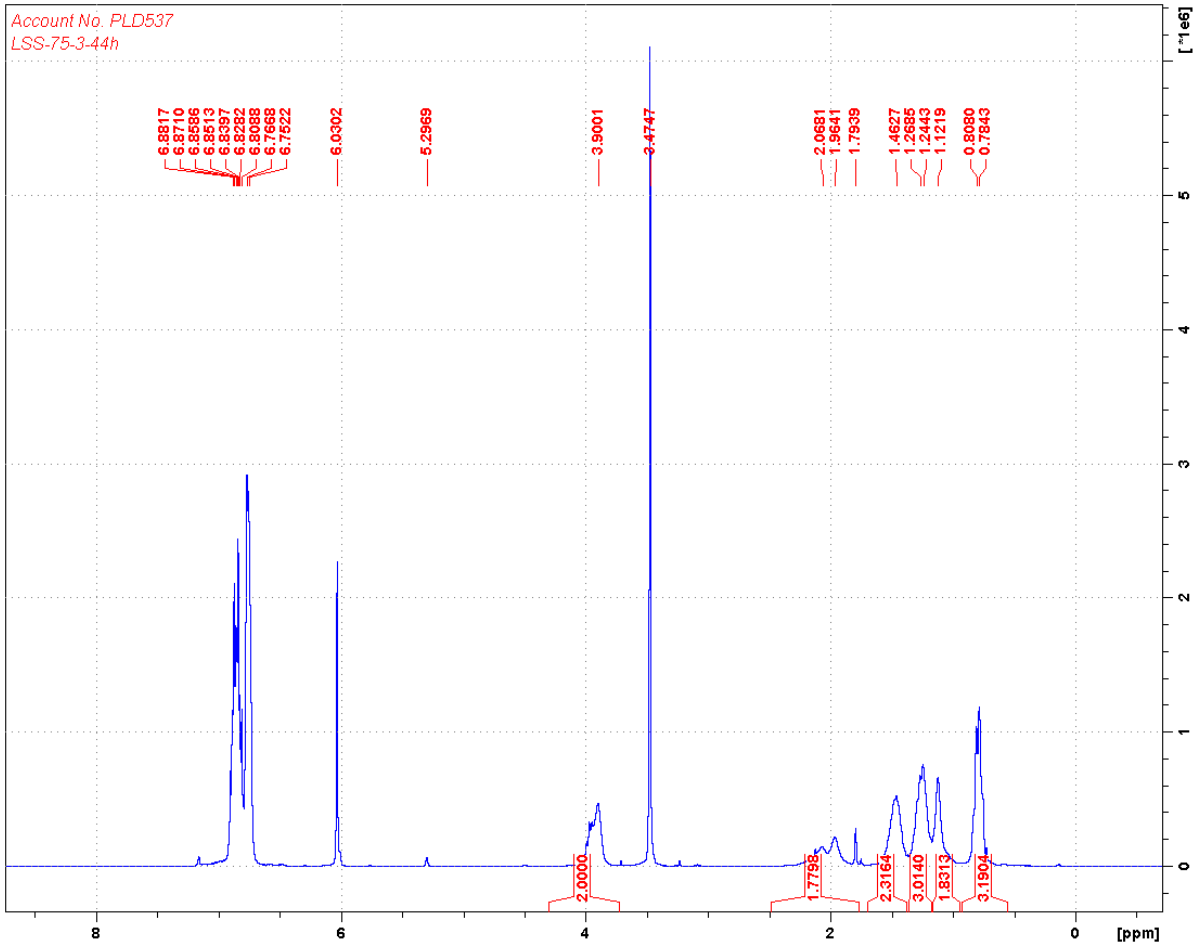

Figure S18. ^{1}H NMR (500 MHz, 25°C, C_6D_6) spectrum of 100 equivalents of *n*-BuMA polymerization by ($fc^{P,B}$)NiBr (Table 1, entry 7). δ (ppm): 6.66-6.97 (m, 4H, 1,2-difluorobenzene), 6.03 (s, 3H, TMB), 5.29 (s, 1H, C*H*$_2$CCH$_3$, *n*-BuMA), 3.90 (br t, 2H, OC*H*$_2$CH$_2$CH$_2$CH$_3$, P*n*-BuMA), 3.47 (s, 9H, OCH$_3$, TMB), 1.96 (m, 2H, OCH$_2$C*H*$_2$CH$_2$CH$_3$, P*n*-BuMA), 1.46 (m, 2H, OCH$_2$CH$_2$C*H*$_2$CH$_3$, P*n*-BuMA), 1.24 (br s, 3H, CCH$_3$, P*n*-BuMA), 1.12 (br s, 2H, CCH$_2$, P*n*-BuMA), 0.78 (br t, 3H, CH$_2$C*H*$_3$, P*n*-BuMA).

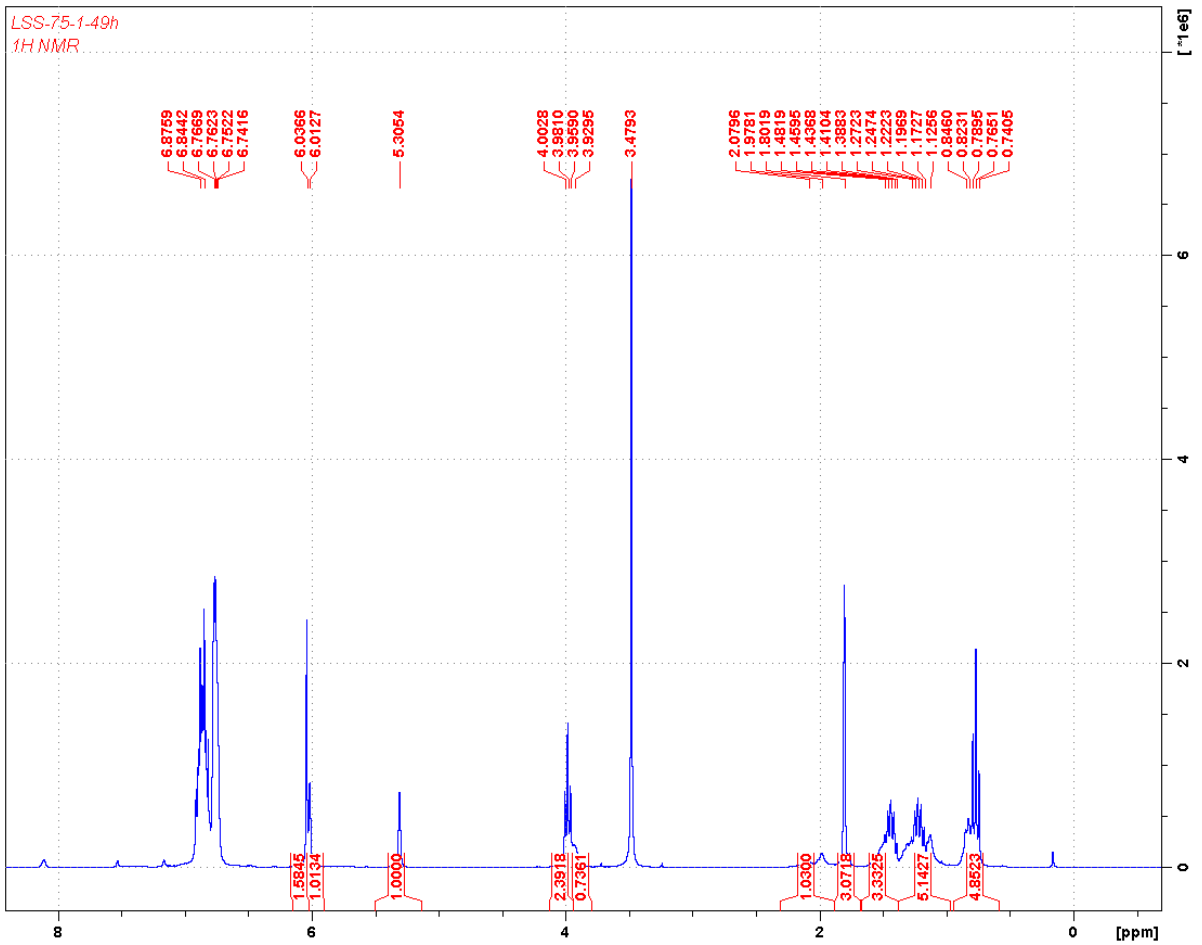

Figure S19. ^{1}H NMR (500 MHz, 25°C, C_6D_6) spectrum of 100 equivalents of *n*-BuMA polymerization by [(fc^{P,B})NiBr][BAr^{F}] (Table 1, entry 8). δ (ppm): 6.54-6.99 (m, 4H, 1,2-difluorobenzene), 6.04 (s, 3H, TMB), 6.01 (s, 1H, C*H*$_2$CCH$_3$, *n*-BuMA), 5.31 (s, 1H, C*H*$_2$CCH$_3$, *n*-BuMA), 3.96 (t, 2H, OC*H*$_2$CH$_2$, *n*-BuMA), 3.93 (br t, 2H, OC*H*$_2$CH$_2$, P*n*-BuMA), 3.48 (s, 9H, OCH$_3$, TMB), 1.98 (m, 2H, OCH$_2$C*H*$_2$CH$_2$CH$_3$, P*n*-BuMA), 1.80 (s, 3H, CCH$_3$, *n*-BuMA), 1.44 (m, 2H, OCH$_2$CH$_2$C*H*$_2$CH$_3$, P*n*-BuMA), 1.22 (m, 2H, OCH$_2$CH$_2$C*H*$_2$CH$_3$, *n*-BuMA), 1.13 (br s, 2H, CCH$_2$, P*n*-BuMA), 0.77 (br t, 3H, CH$_2$C*H*$_3$, *n*-BuMA and P*n*-BuMA).

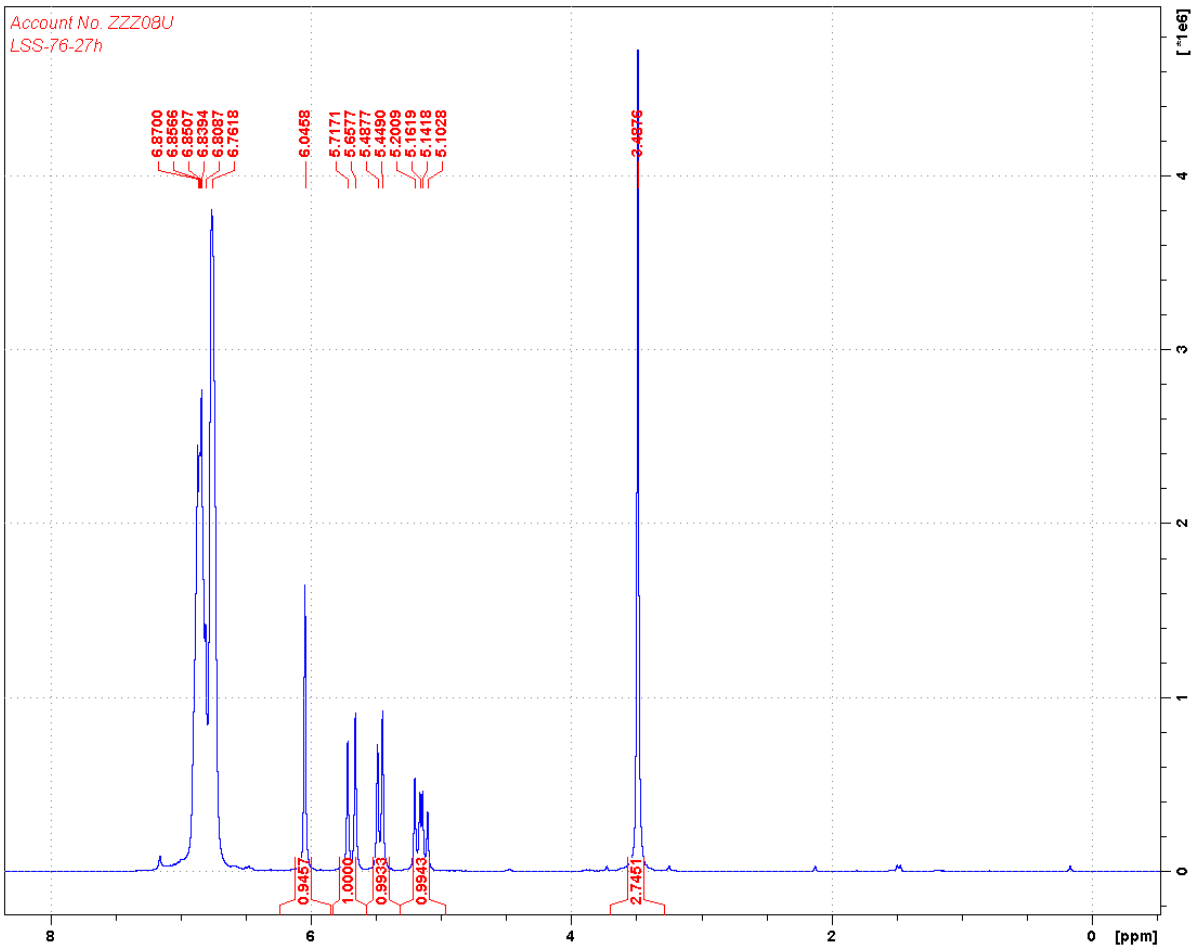

Figure S20. ^{1}H NMR (500 MHz, 25°C, C_6D_6) spectrum of 100 equivalents of acrylonitrile polymerization by ($fc^{P,B}$)NiBr (Table 1, entry 9). δ (ppm): 6.54-7.05 (m, 4H, 1,2-difluorobenzene), 6.05 (s, 3H, TMB), 5.66 (dd, 1H, C*H*$_2$CHC, acrylonitrile), 5.45 (dd, 1H, C*H*$_2$CHC, acrylonitrile), 5.10 (dd, 1H, CH$_2$C*H*C, acrylonitrile), 3.49 (s, 9H, OCH$_3$, TMB).

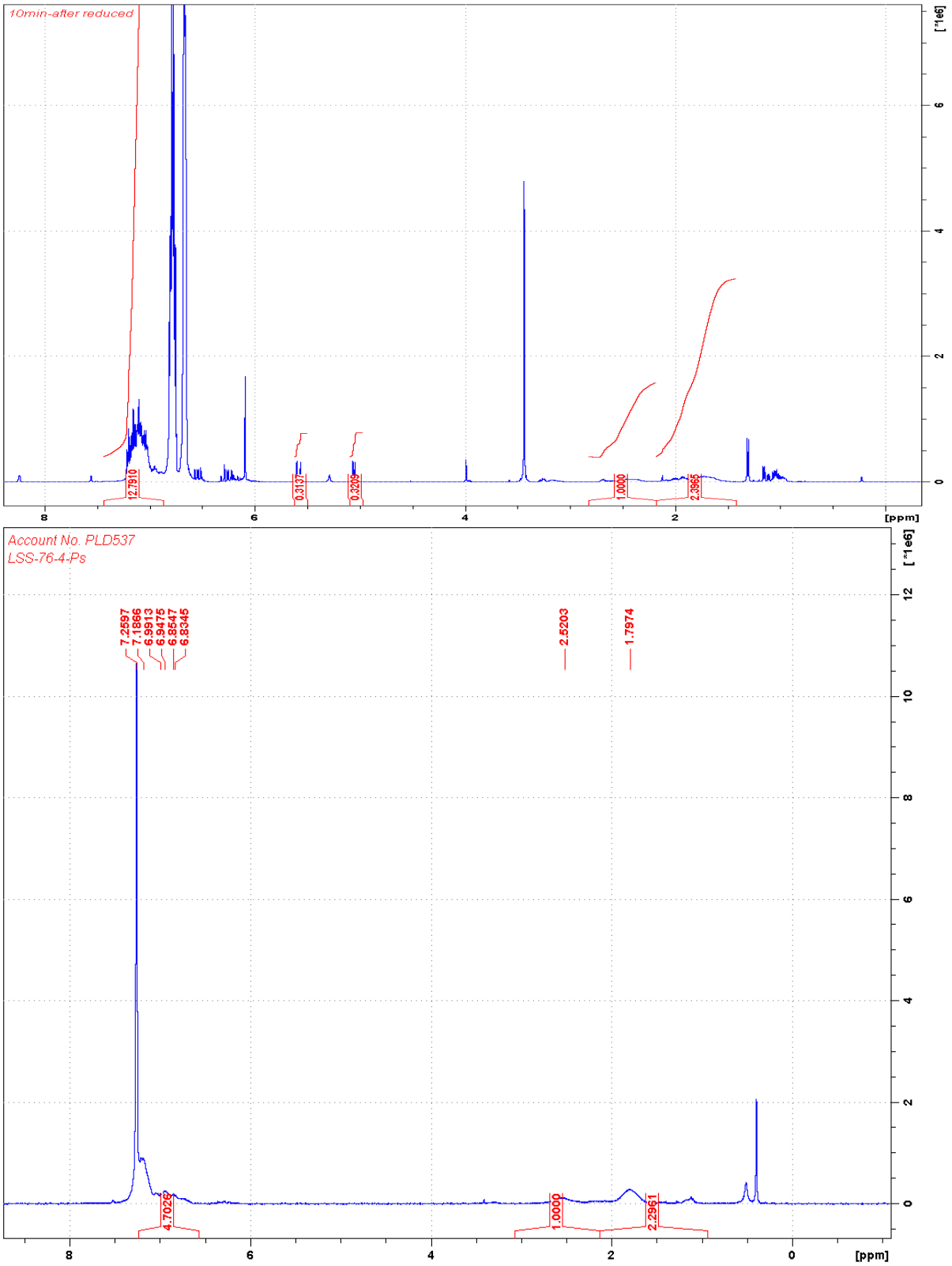

Figure S21. ^{1}H NMR (300 MHz, 25°C) spectra of PS polymerization reaction in C_6D_6 (top) and the isolated polymer of PS in $CDCl_3$ (bottom, Table 2, entry 1). δ (ppm): 7.19 (m, 5H, ArH, PS), 2.52 (br t, 1H, C*H*CH_2, PS), 1.79 (br d, 2H, CHC*H*$_2$, PS).

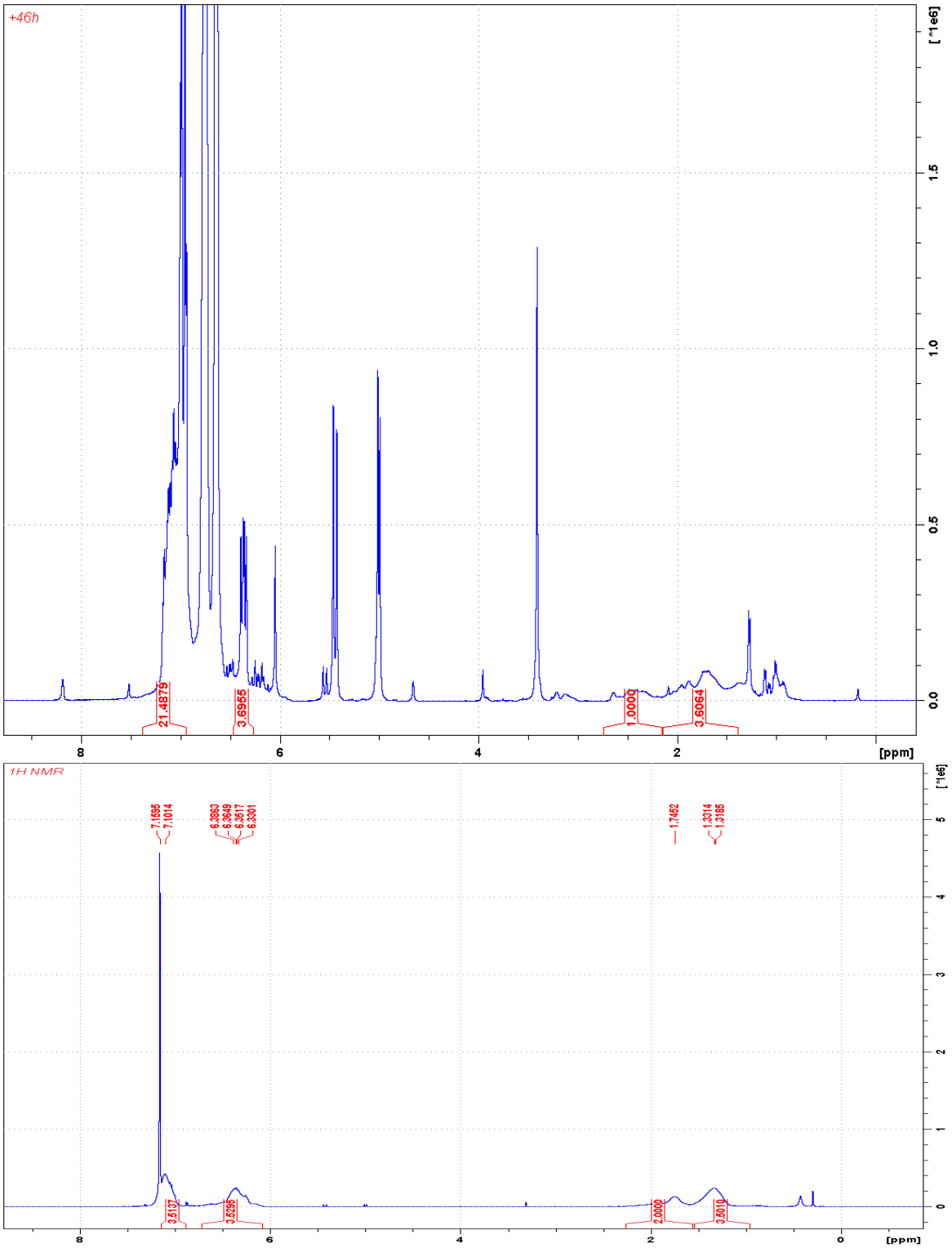

Figure S22. ^{1}H NMR (500 MHz, 25°C) spectra of PS-PCS copolymerization reaction after adding p-CS sequentially in C_6D_6 (top) and the isolated copolymer of PS-PCS in C_6D_6 (bottom, Table 2, entry 2). δ (ppm): 7.10 (m, 2H, ArH, PS and PCS), 6.33 (m, 2H, ArH, PCS), 1.75 (br t, 1H, C*H*CH_2, PS and PCS), 1.32 (br d, 2H, CHC*H*$_2$, PS and PCS).

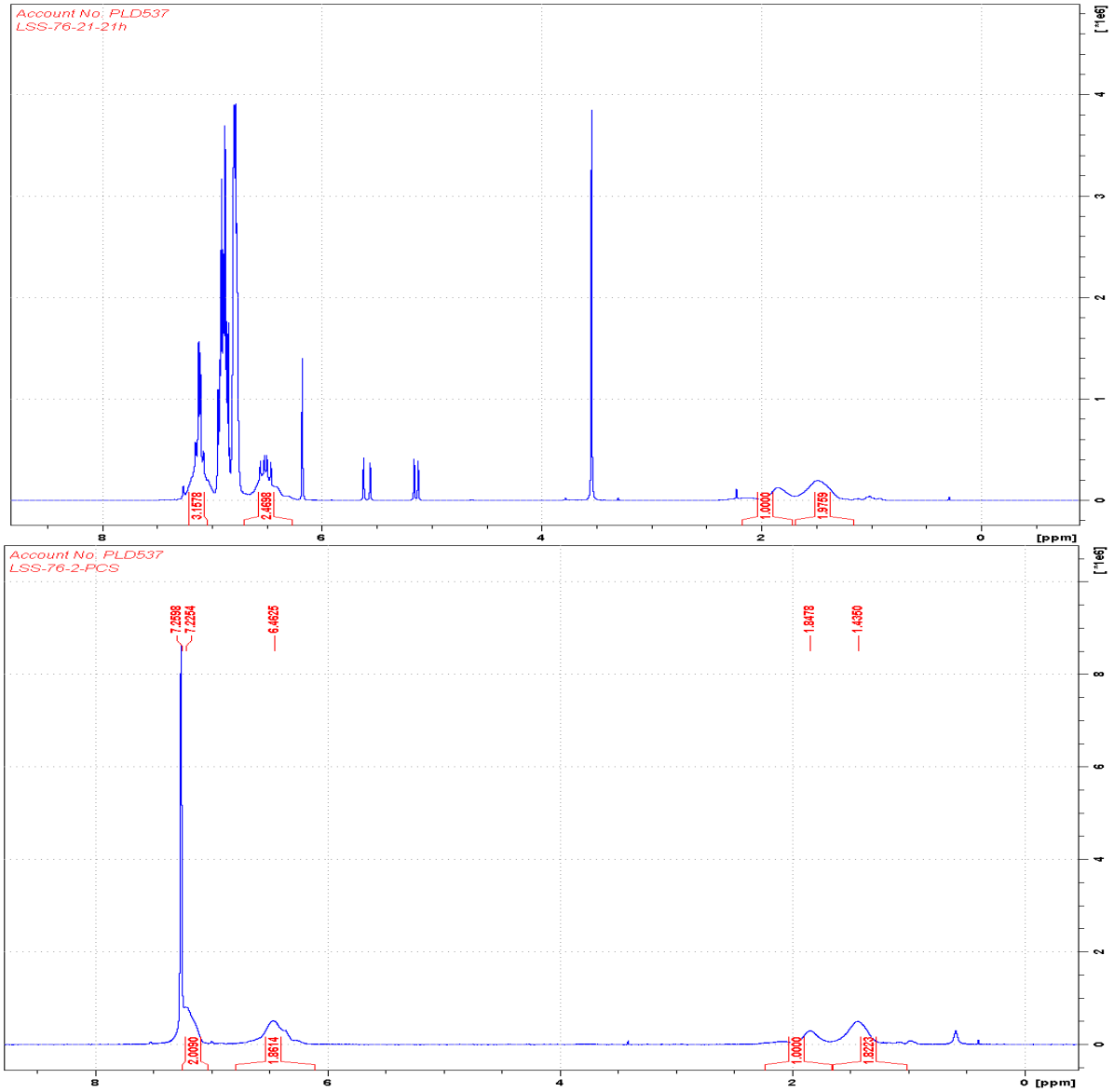

Figure S23. ^{1}H NMR (300 MHz, 25°C) spectra of *p*-CS polymerization reaction in C_6D_6 (top) and the isolated polymer of PCS in $CDCl_3$ (bottom, Table 2, entry 3). δ (ppm): 7.22 (m, 2H, ArH, PCS), 6.46 (m, 2H, ArH, PCS), 1.85 (br t, 1H, C*H*CH_2, PCS), 1.43 (br d, 2H, CHC*H*$_2$, PCS).

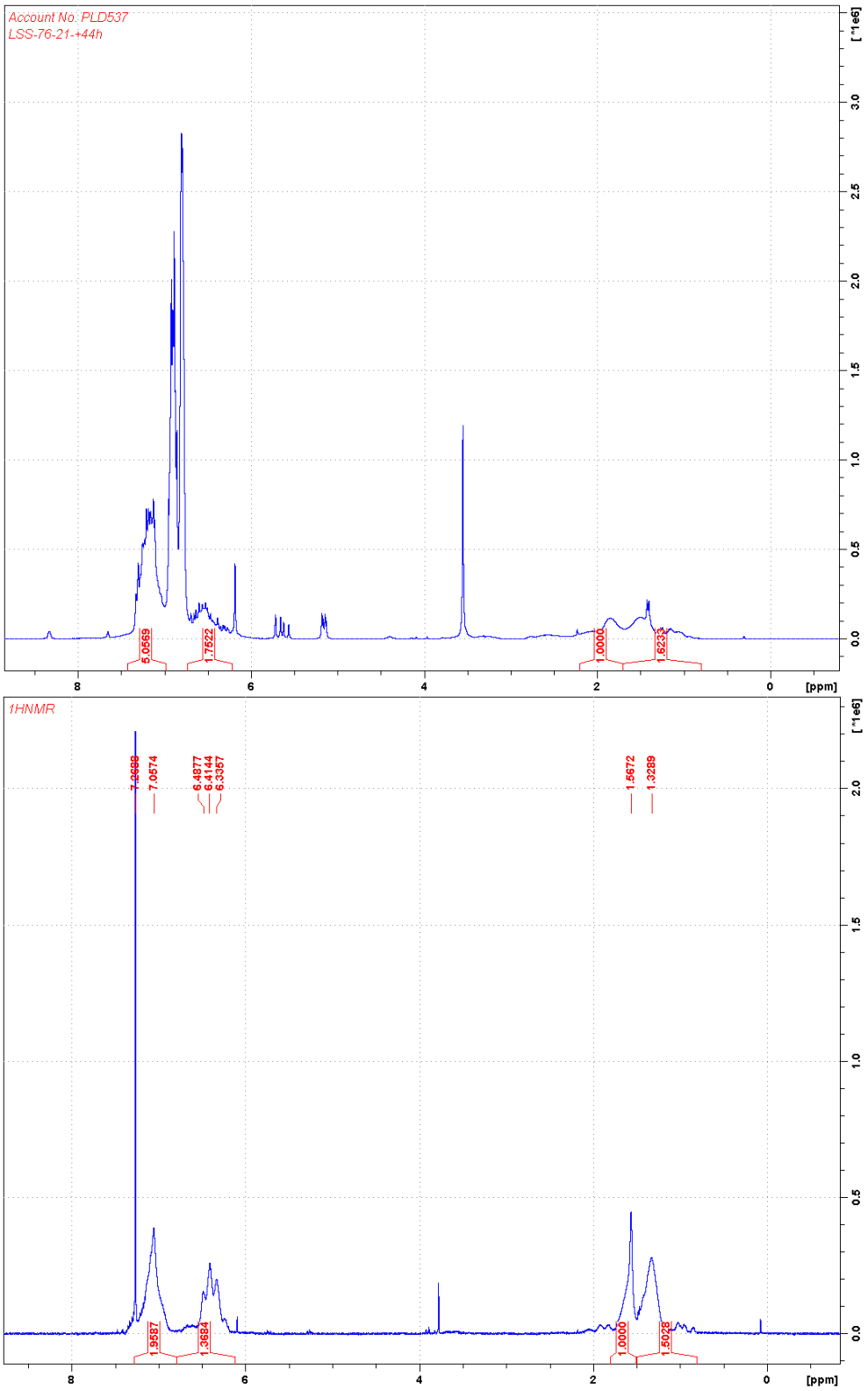

Figure S24. ^{1}H NMR (300 MHz, 25°C) spectra of PCS-PS copolymerization reaction in C_6D_6 (top) after adding styrene sequentially and the isolated polymer of PCS-PS in $CDCl_3$ (bottom, Table 2, entry 4). δ (ppm): 7.06 (m, 2H, ArH, PS and PCS), 6.33 (m, 2H, ArH, PCS), 1.57 (br t, 1H, C*H*CH_2, PS and PCS), 1.33 (br d, 2H, CHC*H*$_2$, PS and PCS).

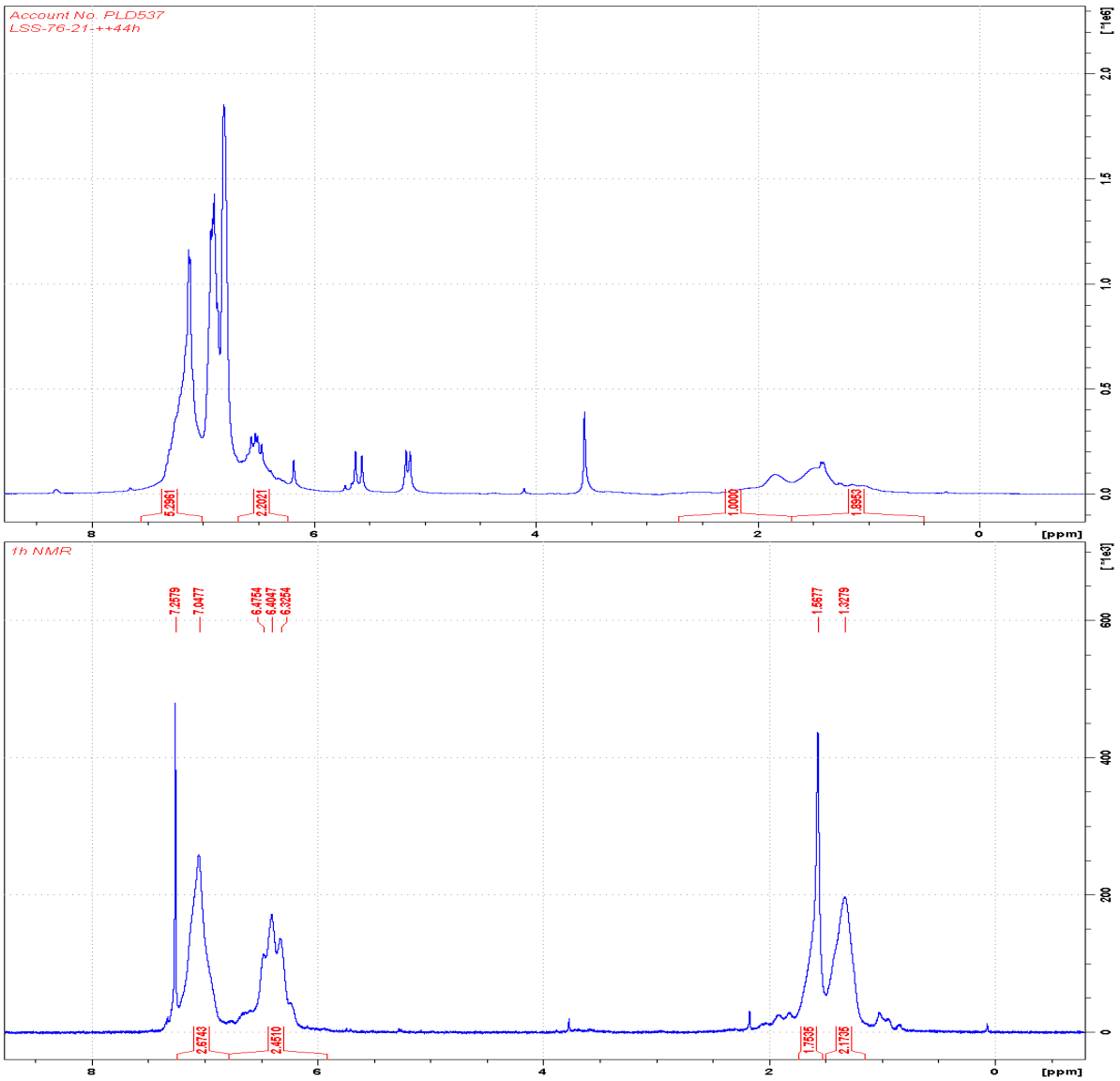

Figure S25. ^{1}H NMR (300 MHz, 25°C) spectra of PCS-PS-PCS copolymerization reaction after adding p-CS again in C_6D_6 (top) and the isolated polymer of PCS-PS-PCS in $CDCl_3$ (bottom, Table 2, entry 5). δ (ppm): 7.05 (m, 2H, ArH, PS and PCS), 6.33 (m, 2H, ArH, PCS), 1.57 (br t, 1H, C*H*CH_2, PS and PCS), 1.33 (br d, 2H, CHC*H*$_2$, PS and PCS).

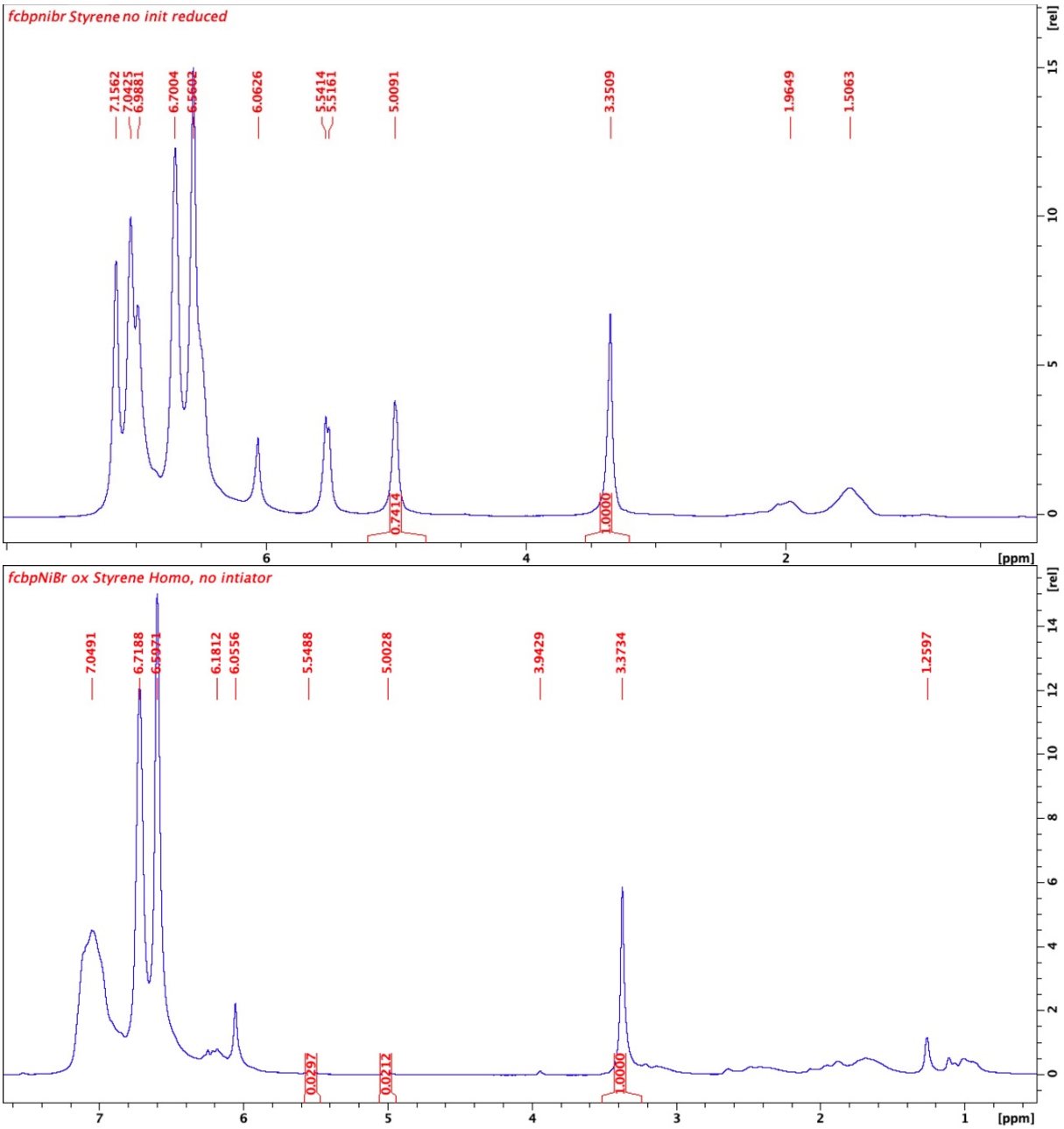

Figure S26. ^{1}H NMR (600 MHz, 25°C, C_6D_6) spectra of 100 equivalents of styrene polymerization by ($fc^{P,B}$)NiBr (top) and [($fc^{P,B}$)NiBr][BAr^{F}] (bottom) in the absence of a radical initiator (Table S1, entries 1 & 2). δ (ppm): 7.02 (m, 5H, ArH, PS), 6.46-6.85 (m, 4H, 1,2-difluorobenzene), 6.04 (s, 3H, TMB), 3.41 (s, 9H, OCH_3, TMB), 2.45 (br t, 1H, C*H*CH_2, PS), 1.88 (br d, 2H, CHC*H*$_2$, PS).

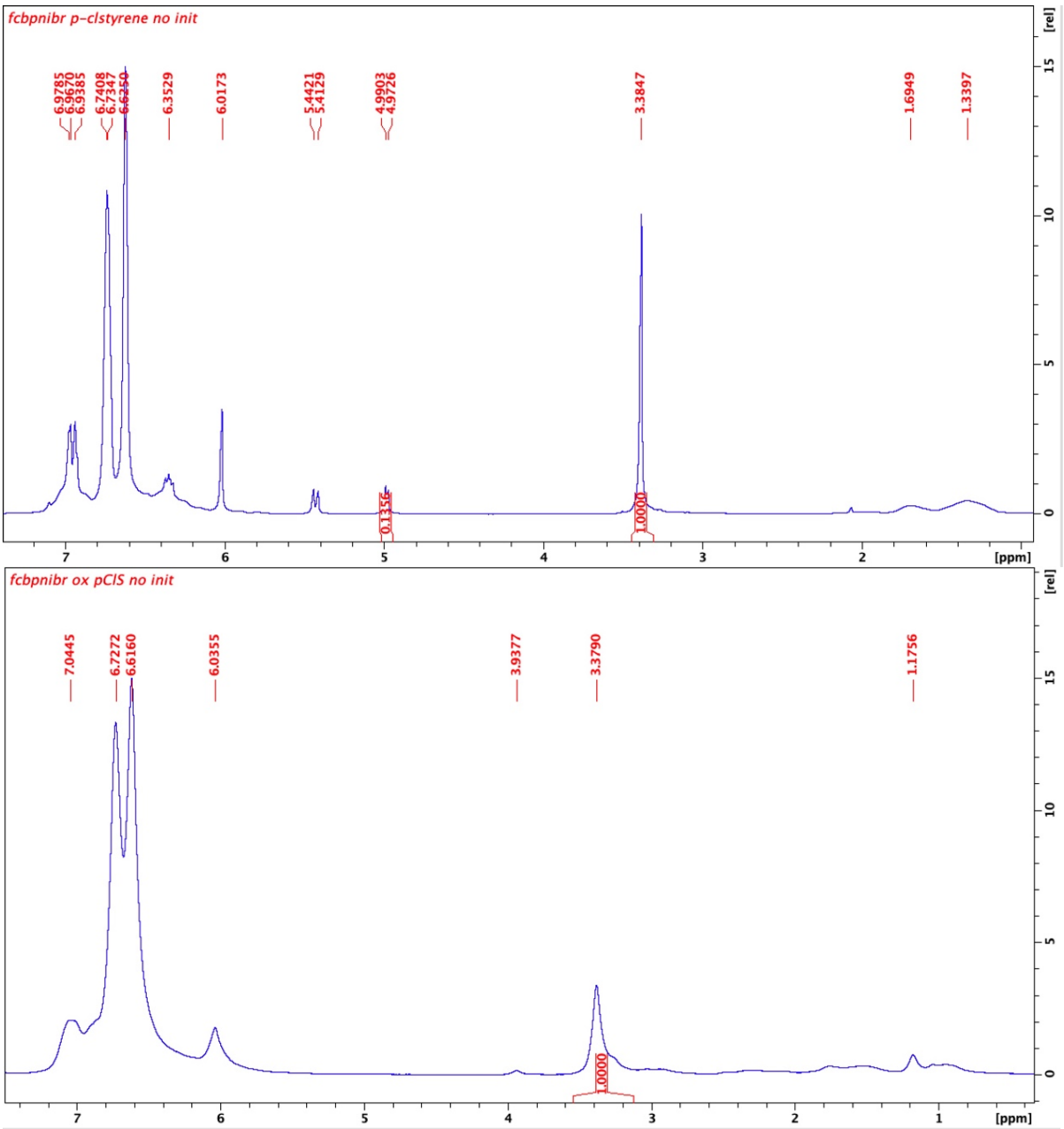

Figure S27. ^{1}H NMR (600 MHz, 25°C, C_6D_6) spectra of 100 equivalents of *p*-chlorostyrene polymerization by ($fc^{P,B}$)NiBr (top) and [($fc^{P,B}$)NiBr][BAr^{F}] (bottom) in the absence of a radical initiator (Table S1, entries 3 & 4). δ (ppm): 7.02 (m, 2H, ArH, PCS), 6.58-6.89 (m, 4H, 1,2-difluorobenzene), 6.42 (m, 2H, ArH, PCS), 6.07 (s, 3H, TMB), 5.50 (br dd, 1H, CHC*H*$_2$, p-CS), 5.05 (br dd, 1H, CHC*H*$_2$, p-CS), 3.44 (s, 9H, OCH_3, TMB), 1.75 (br t, 1H, C*H*CH_2, PCS), 1.38 (br d, 2H, CHC*H*$_2$, PCS).

SEC data

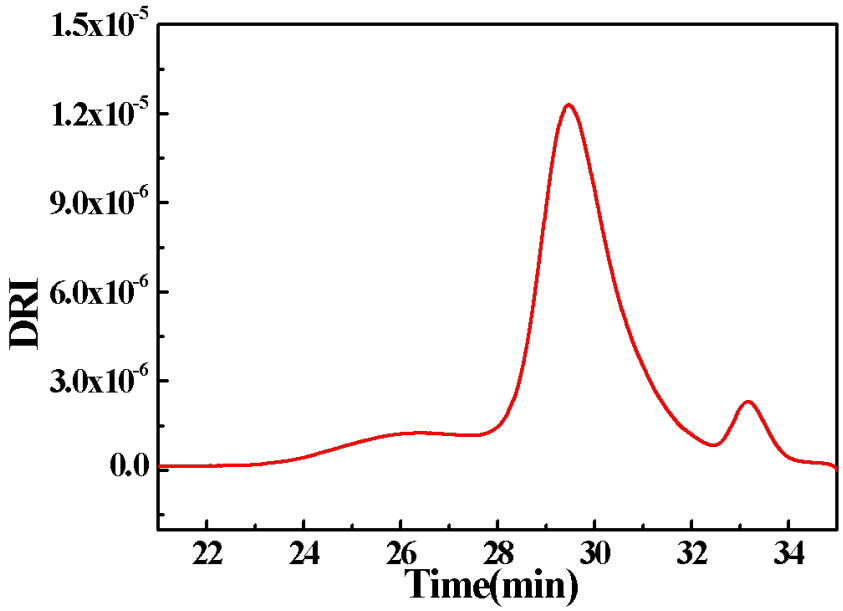

Figure S28. SEC trace for polymerization of 100 equivalents of styrene using [($fc^{P,B}$)NiBr][BAr^F] at 25 °C (Table 1, entry 2).

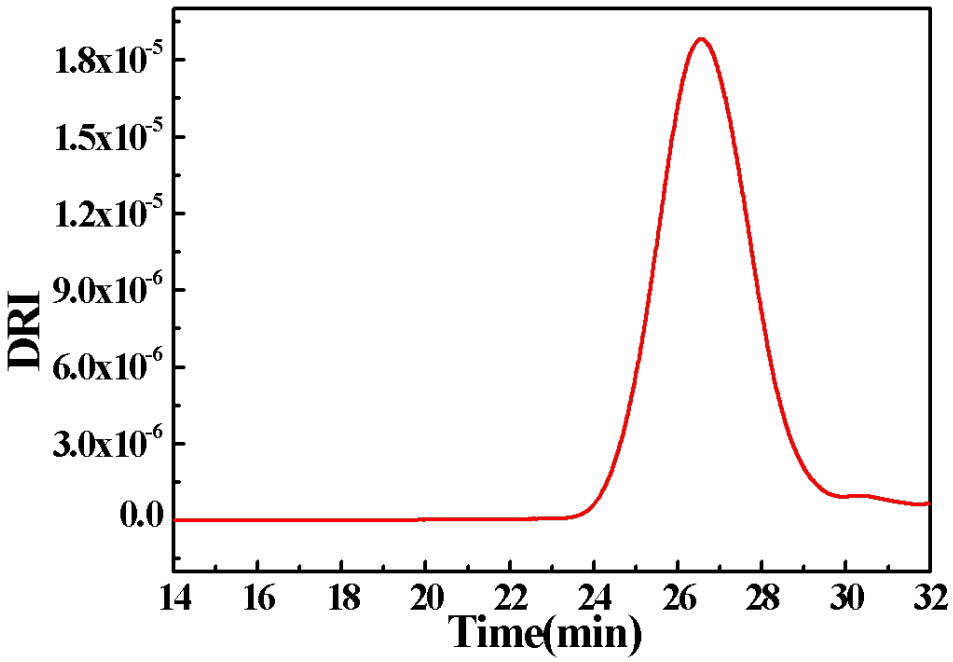

Figure S29. SEC trace for polymerization of 100 equivalents of *p*-CS using ($fc^{P,B}$)NiBr at 80 °C (Table 1, entry 4).

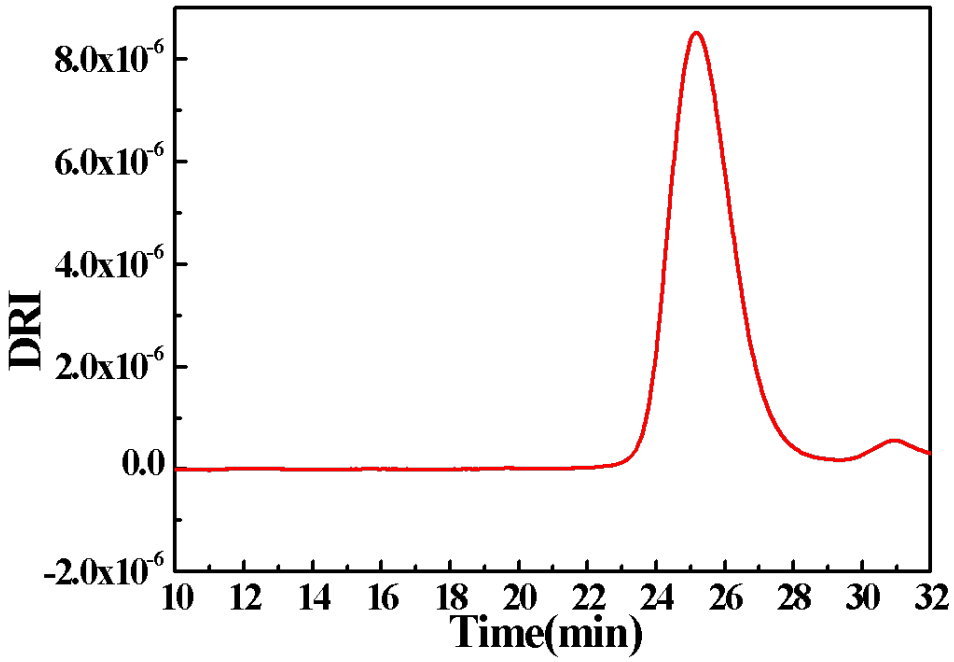

Figure S30. SEC trace for polymerization of 100 equivalents of MMA using [($fc^{P,B}$)NiBr][BAr^F] at 25 °C (Table 1, entry 6).

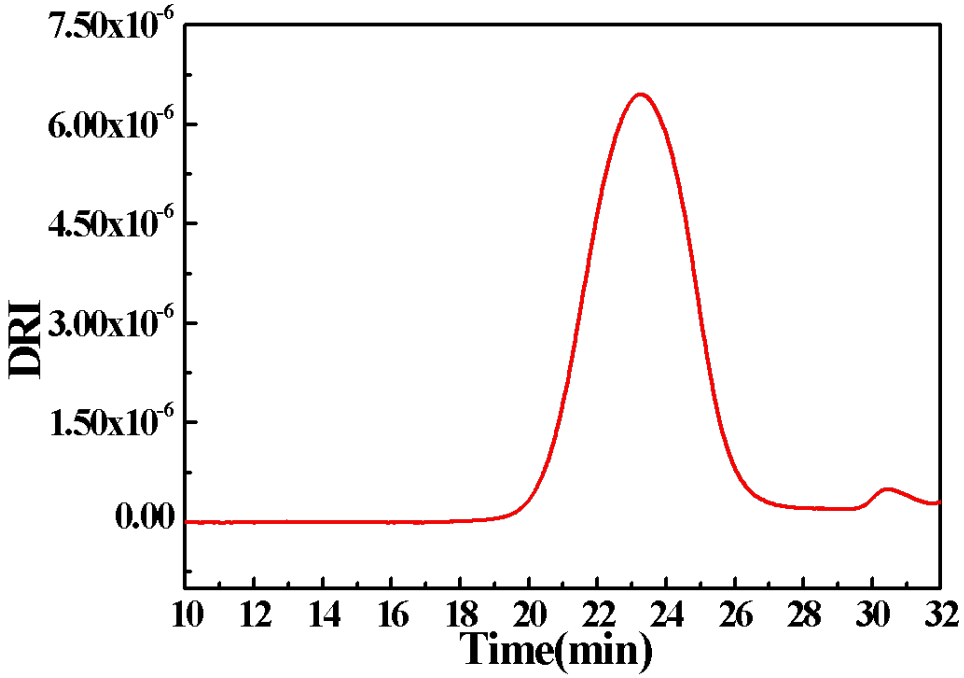

Figure S32. SEC trace for polymerization of 100 equivalents of *n*-BuMA using ($fc^{P,B}$)NiBr at 80 °C (Table 1, entry 7).

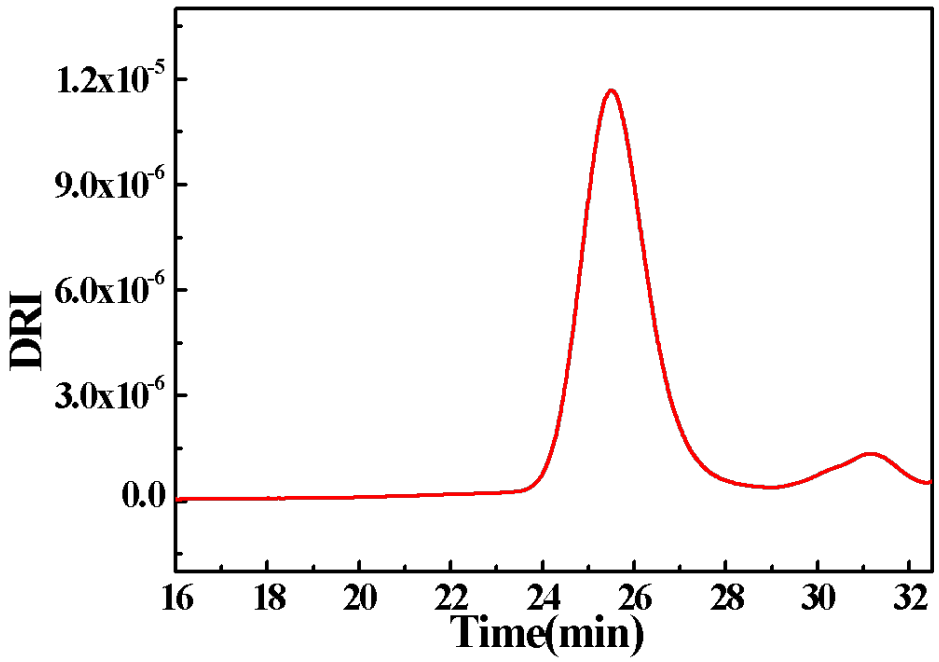

Figure S33. SEC trace for polymerization of 100 equivalents of *n*-BuMA using [(fc^{P,B})NiBr][BAr^{F}] at 25 °C (Table 1, entry 8).

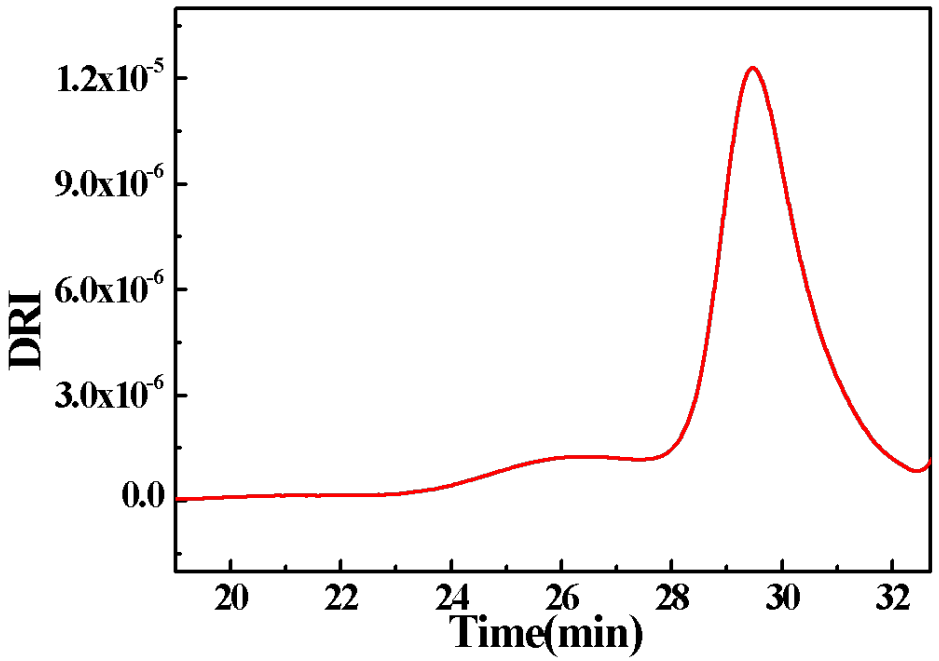

Figure S34. SEC trace of PS homopolymer using [(fc^{P,B})NiBr][BAr^{F}] at 25 °C (Table 2, entry 1).

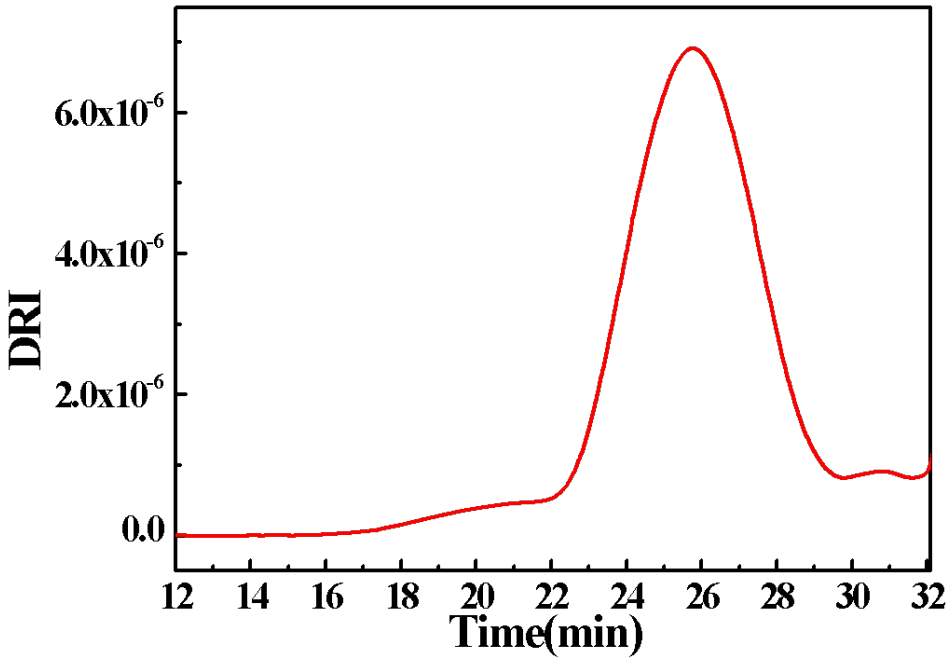

Figure S35. SEC trace of PS-PCS di-block copolymer using ($fc^{P,B}$)NiBr and [($fc^{P,B}$)NiBr][BAr^F] (Table 2, entry 2).

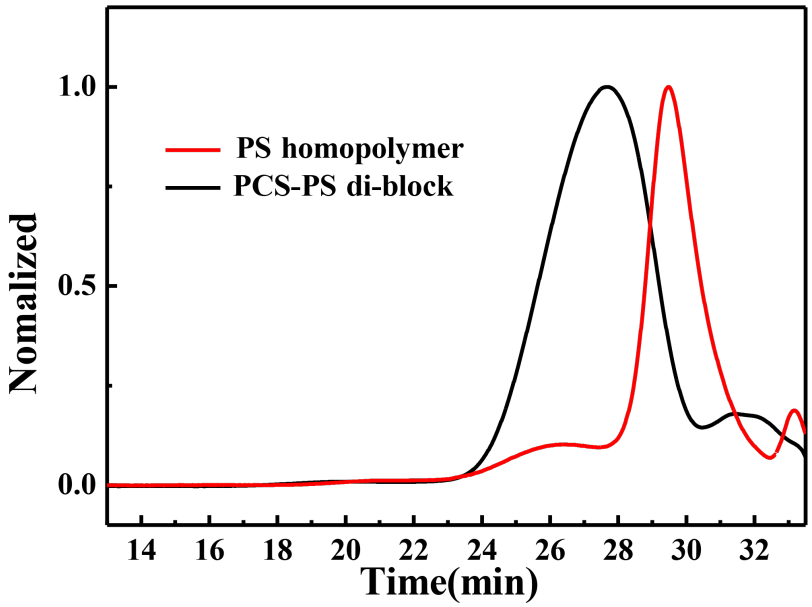

Figure S36. SEC trace of the PS-PCS diblock copolymer and PS homopolymer (Table 2, entries 1 and 2).

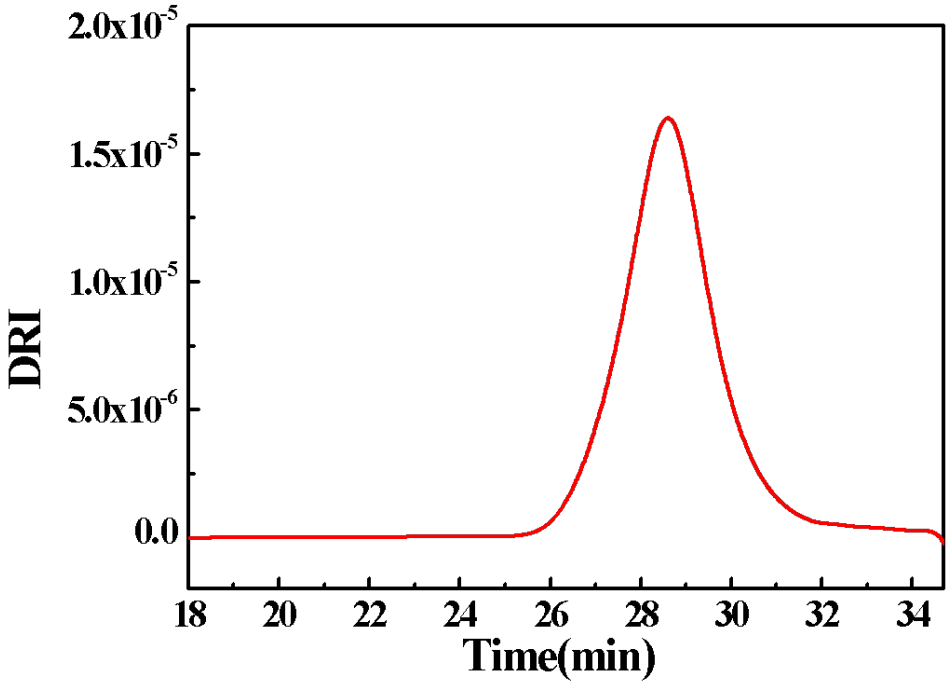

Figure S37. SEC trace of PCS homopolymer using ($fc^{P,B}$)NiBr at 25°C (Table 2, entry 3).

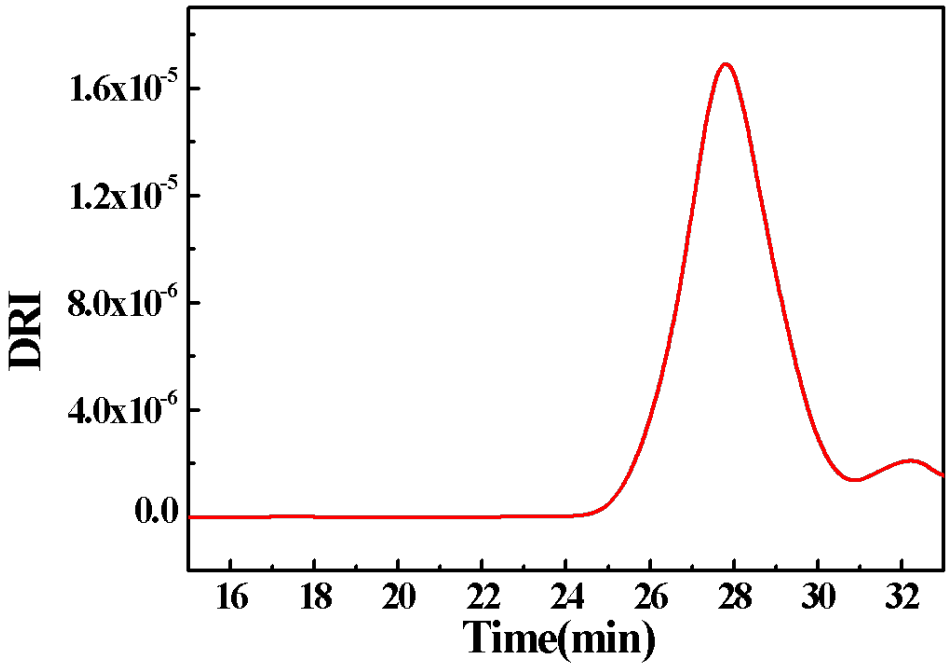

Figure S38. SEC trace of PCS-PS di-block copolymer using ($fc^{P,B}$)NiBr and [($fc^{P,B}$)NiBr][BAr^F] (Table 2, entry 4).

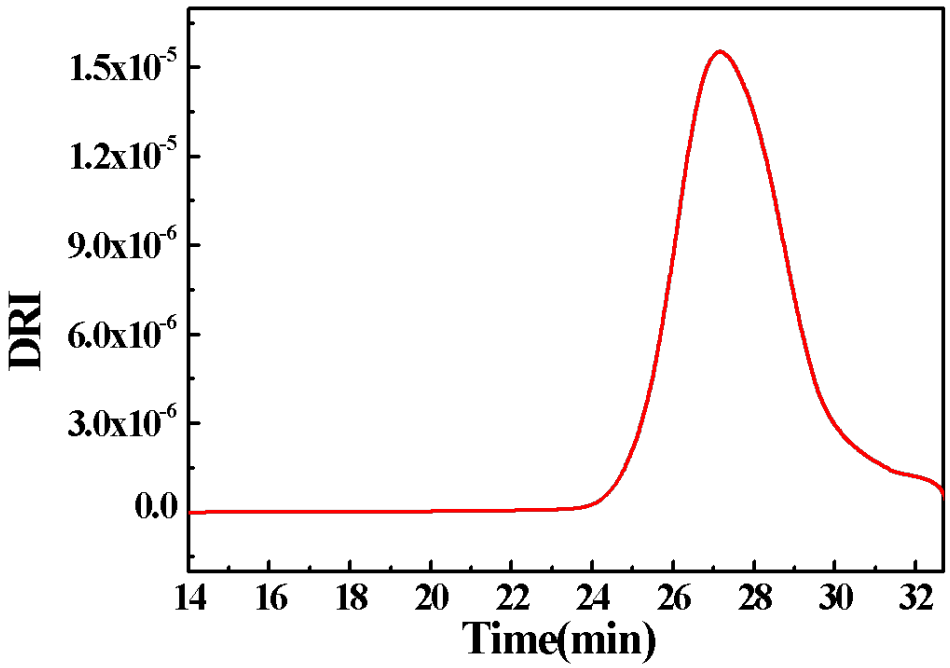

Figure S39. SEC trace of PCS-PS-PCS tri-block copolymer using $(fc^{P,B})$NiBr and $[(fc^{P,B})NiBr][BAr^F]$ (Table 2, entry 5).

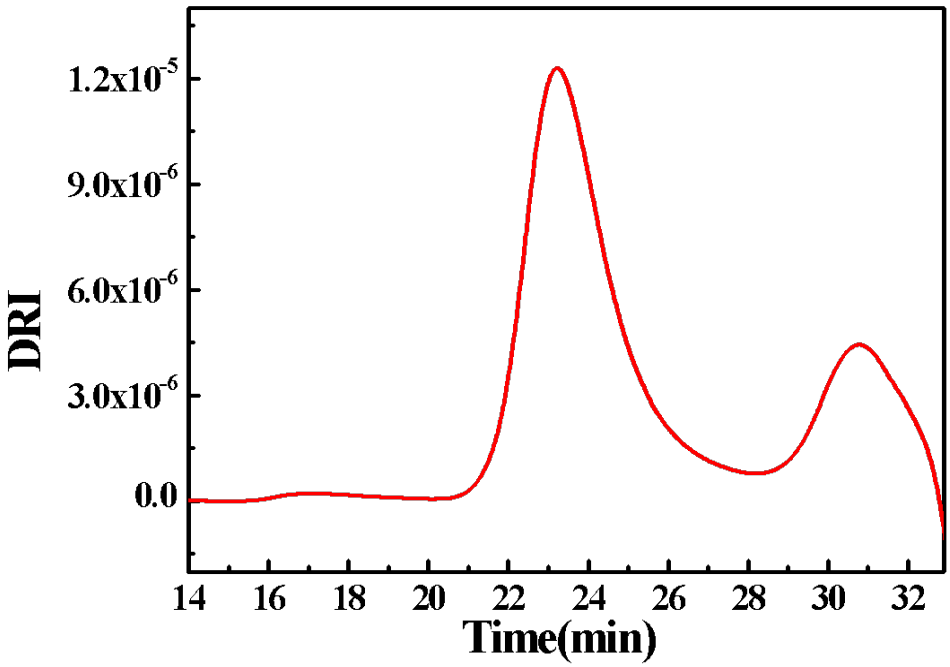

Figure S40. SEC trace of PS-PCS-PS tri-block copolymer using $(fc^{P,B})$NiBr and $[(fc^{P,B})NiBr][BAr^F]$ (Table S2, entry 5).

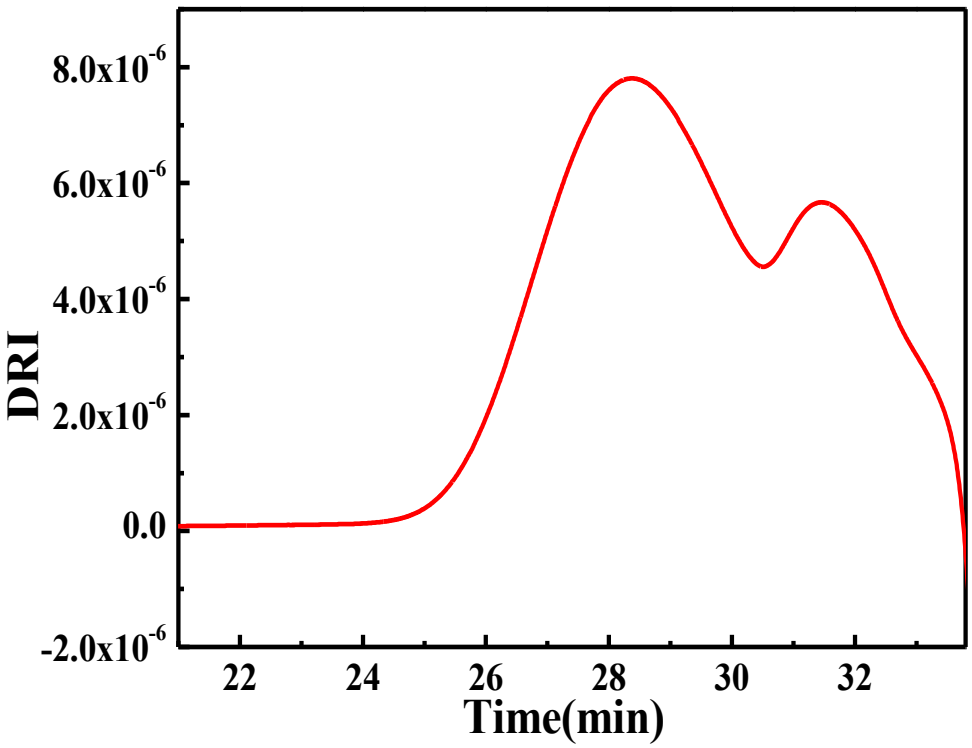

Figure S41. SEC trace of PS-PCS polymer obtain using a one pot synthesis by ($fc^{P,B}$)NiBr and [($fc^{P,B}$)NiBr][BAr^F].

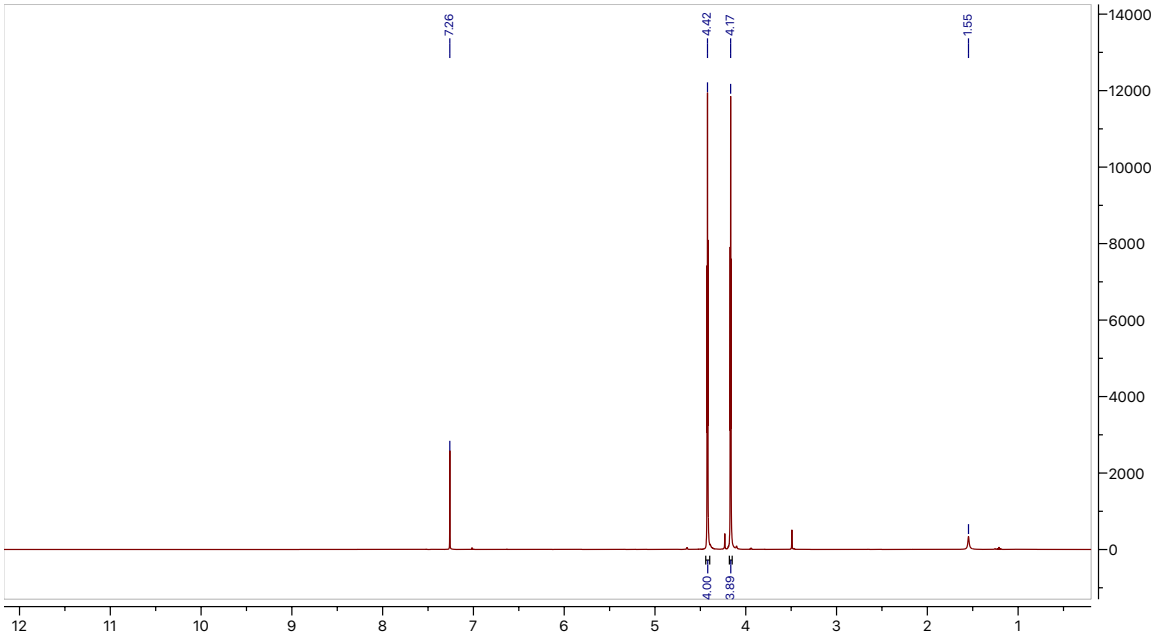

Figure S48. ^{1}H NMR (400 MHz, 298K, $CDCl_3$) spectrum of 1,1'-dibromoferrocene. δ (ppm): 4.42 (t, 4H, Cp-H), 4.17 (t, 4H, Cp-H). The peak at 1.55 ppm is attributed to residual water.

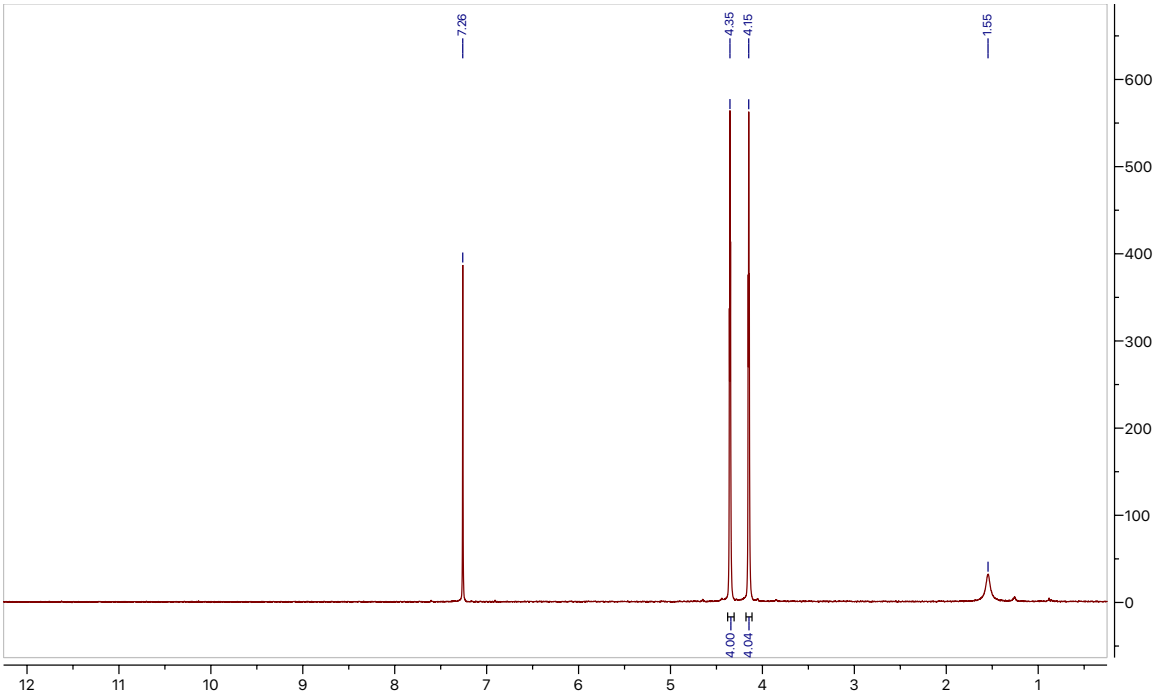

Figure S49. ^{1}H NMR (300 MHz, 298K, $CDCl_3$) spectrum of 1,1'-diazidoferrocene. δ (ppm): 4.35 (t, 4H, Cp-H), 4.15 (t, 4H, Cp-H). The peak at 1.55 ppm is attributed to residual water.

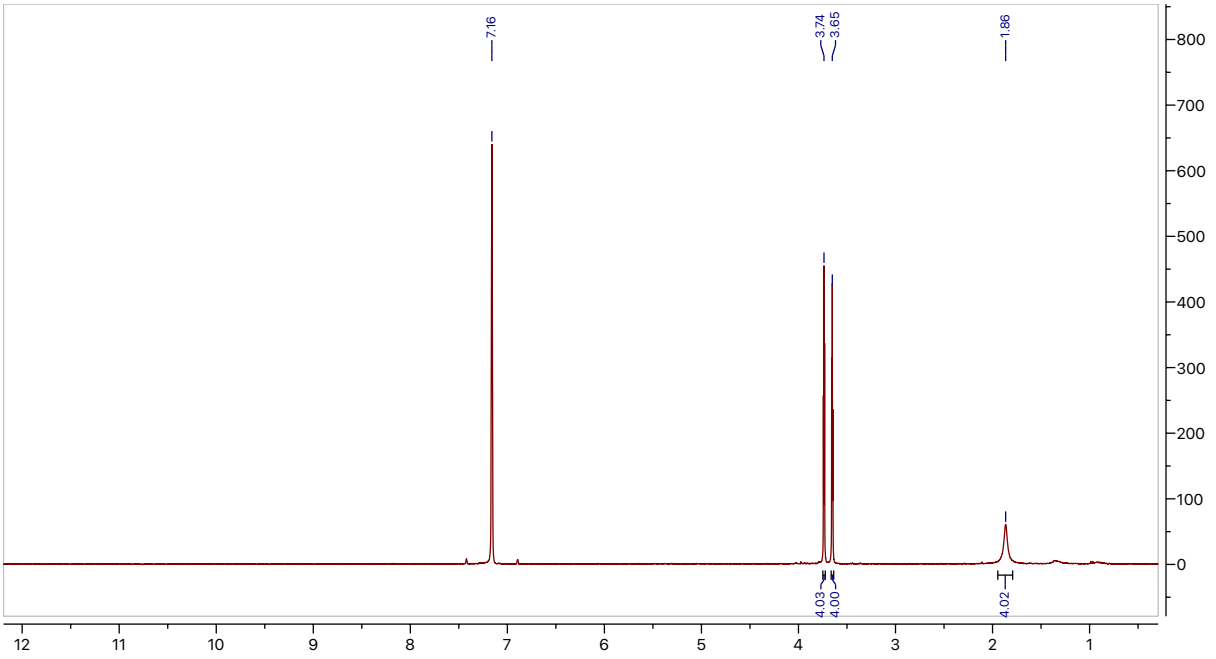

Figure S50. ^{1}H NMR (300 MHz, 298K, C_6D_6) spectrum of 1,1'-aminoferrocene. δ (ppm): 3.74 (t, 4H, Cp-H), 3.65 (t, 4H, Cp-H), 1.86 (br s, 4H, NH_2).

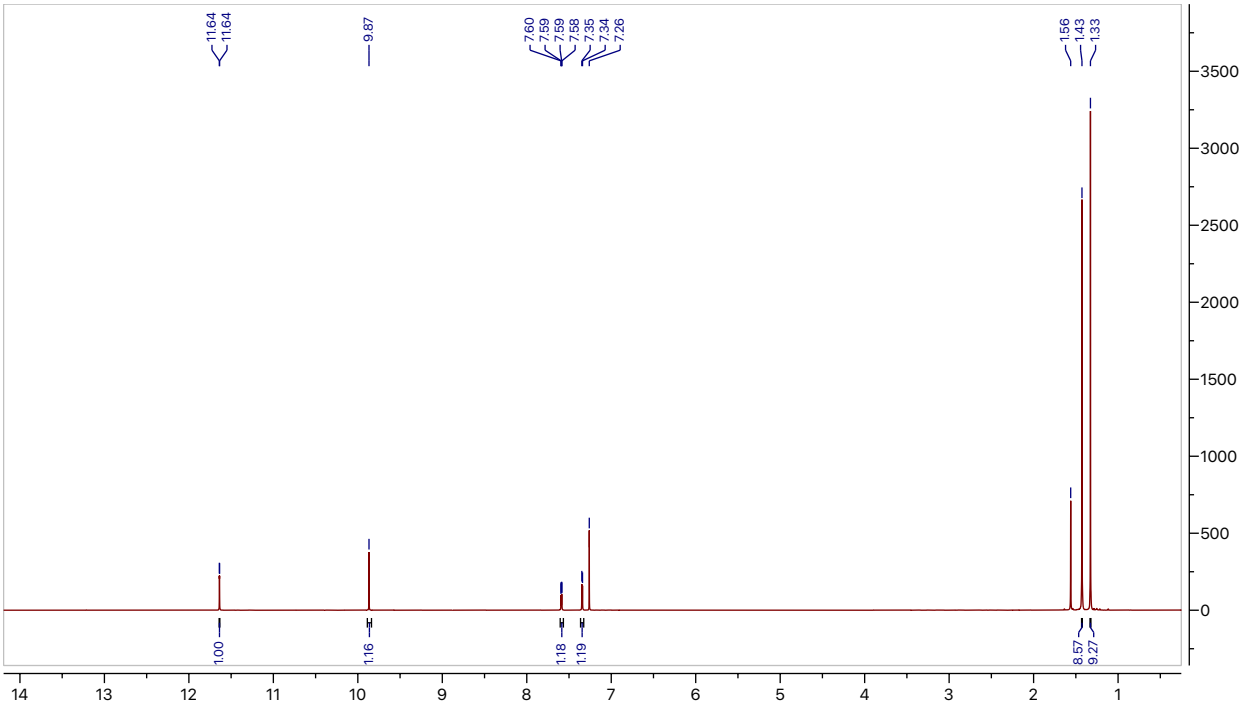

Figure S51. ^{1}H NMR (300 MHz, 298K, $CDCl_3$) spectrum of 3,5-di-*tert*-butyl-2-hydroxybenzaldehyde. δ (ppm): 11.64 (s, 1H, OH), 9.87 (s, 1H, N=CH), 7.60 (d, 1H, Ar-H), 7.34 (d, 1H, Ar-H), 1.84 (s, 9H, CCH_3), 1.34 (s, 9H, CCH_3). The peak at 1.56 ppm is attributed to residual water.

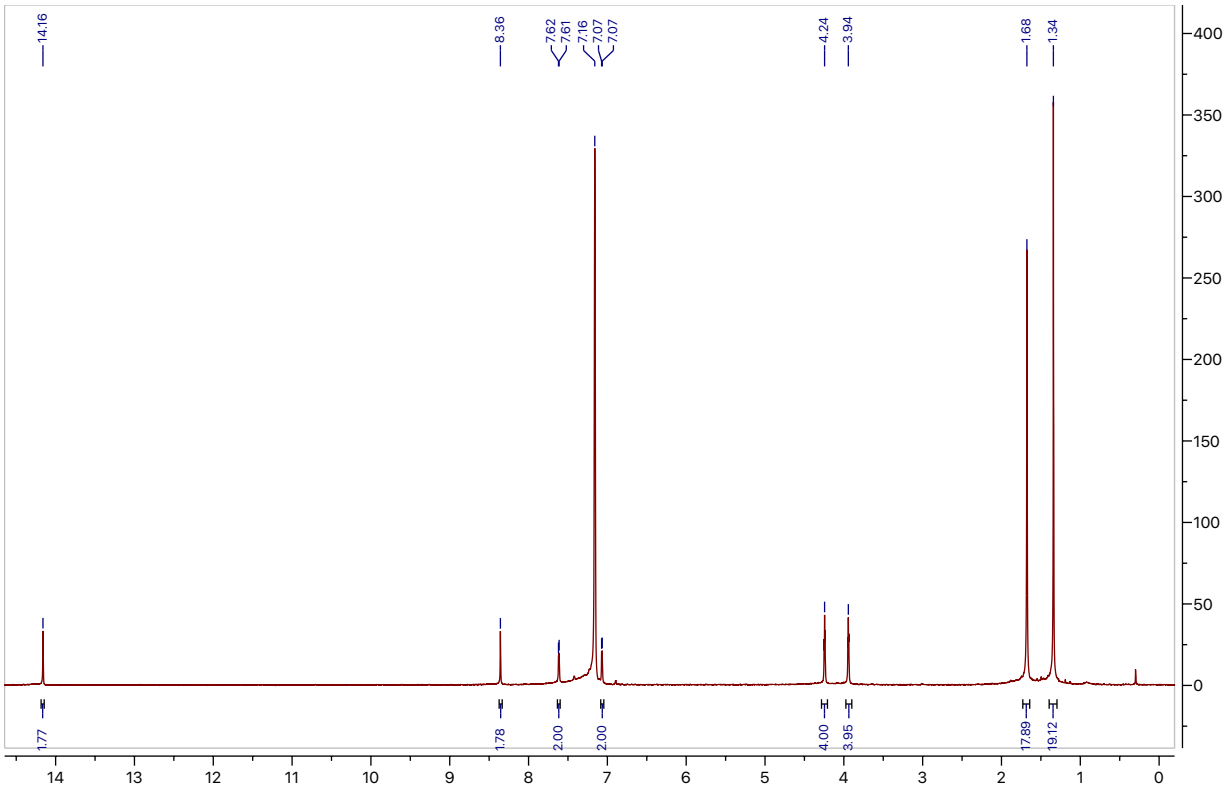

Figure S52. ^{1}H NMR (300 MHz, 298K, C_6D_6) spectrum of H_2(salfen). δ (ppm): 14.16 (s, 2H, OH), 8.36 (s, 2H, N=CH), 7.762(d, 2H, Ar-H), 7.07 (d, 2H, Ar-H), 4.24 (br s, 4H, Cp-H), 3.94 (br s, 4H, Cp-H), 1.68 (s, 18H, CCH_3), 1.34 (s, 18H, CCH_3).

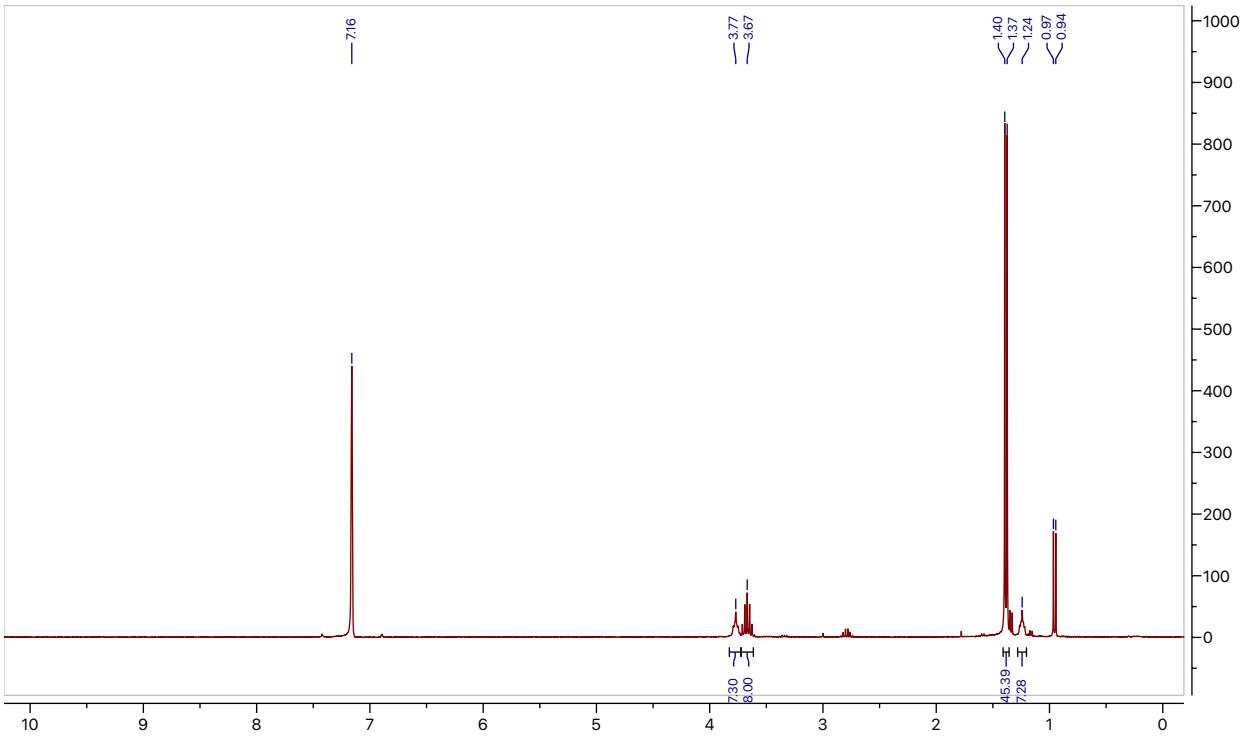

Figure S53. ^{1}H NMR (300 MHz, 298K, C_6D_6) spectrum of $[Sc(DIPA)_2(THF)(\mu\text{-}Cl)]_2$. δ (ppm): 3.77 (m, 8H, OCH_2CH_2), 3.67 (s, 8H, $CH(CH_3)_2$), 1.38 (d, 48H, $CH(CH_3)_2$), 1.24 (m, 8H, OCH_2CH_2). The peaks at 0.98 are attributed to residual DIPA.

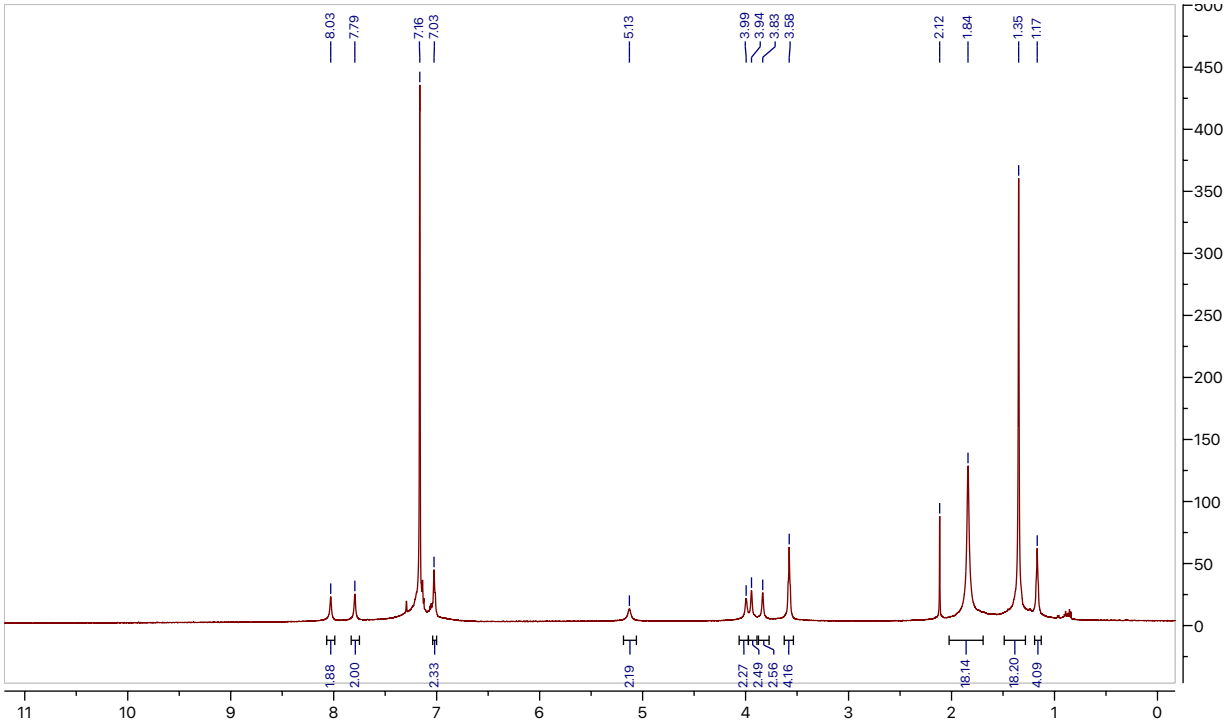

Figure S54. ^{1}H NMR (600 MHz, 298K, C_6D_6) spectrum of (salfen)ScClTHF. δ (ppm): 8.03 (br s, 2H, N=CH), 7.79 (br s, 2H, Ar-H), 7.02 (br s, 2H, Ar-H), 5.12, 3.99, 3.94 and 3.83 (br s, 8H, Cp-H), 3.57 (br s, 4H, OCH_2), 1.84 (br s, 18H, CCH_3), 1.34 (br s, 18H, CCH_3), 1.16 (br s, 4H, CH_2CH_3O). The peak at 2.12 ppm is attributed to residual toluene.

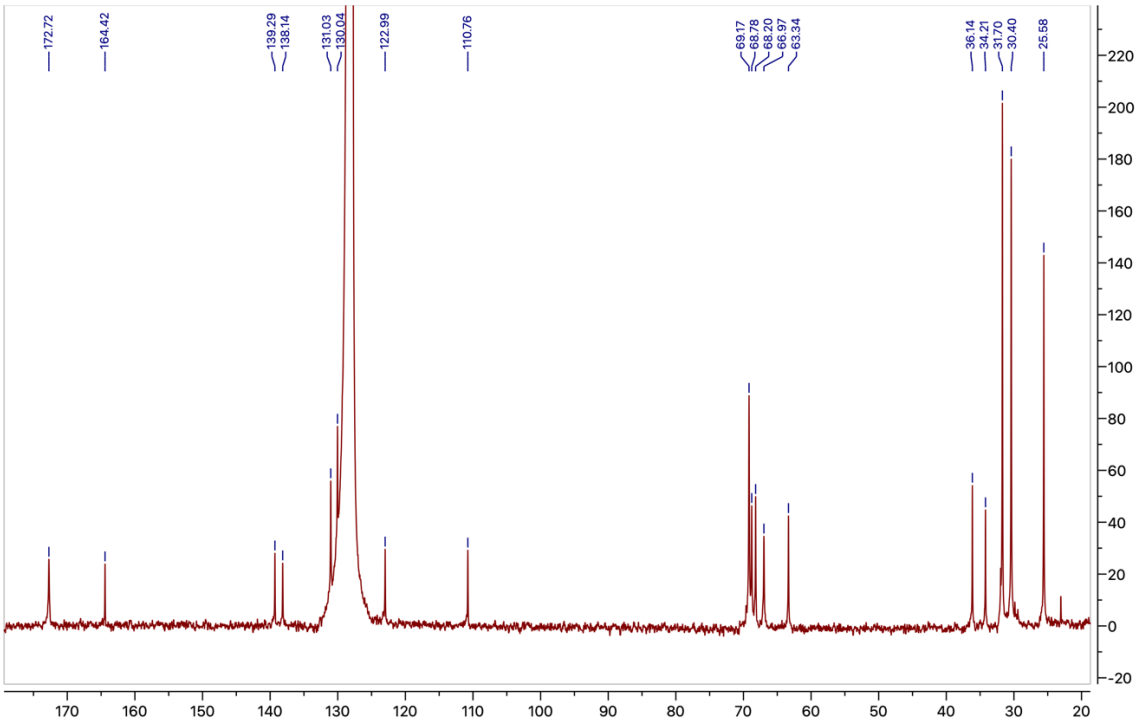

Figure S55. ^{13}C-NMR (125 MHz, 298K, C_6D_6) spectrum of (salfen)ScClTHF. δ (ppm): 172.72 (N=C), 164.42 (OC_6H_2), 139.29 (OC_6H_2), 138.14 (OC_6H_2), 131.03 (OC_6H_2), 130.03 (OC_6H_2), 122.99 (OC_6H_2), 110.76 (N-C), 69.17-66.97 (C_5H_4), 63.34 (OCH_2CH_2), 36.14 ($C(CH_3)_3$), 34.21 ($C(CH_3)_3$), 31.70 ($C(CH_3)_3$), 30.40 ($C(CH_3)_3$), 25.58 (OCH_2CH_2).

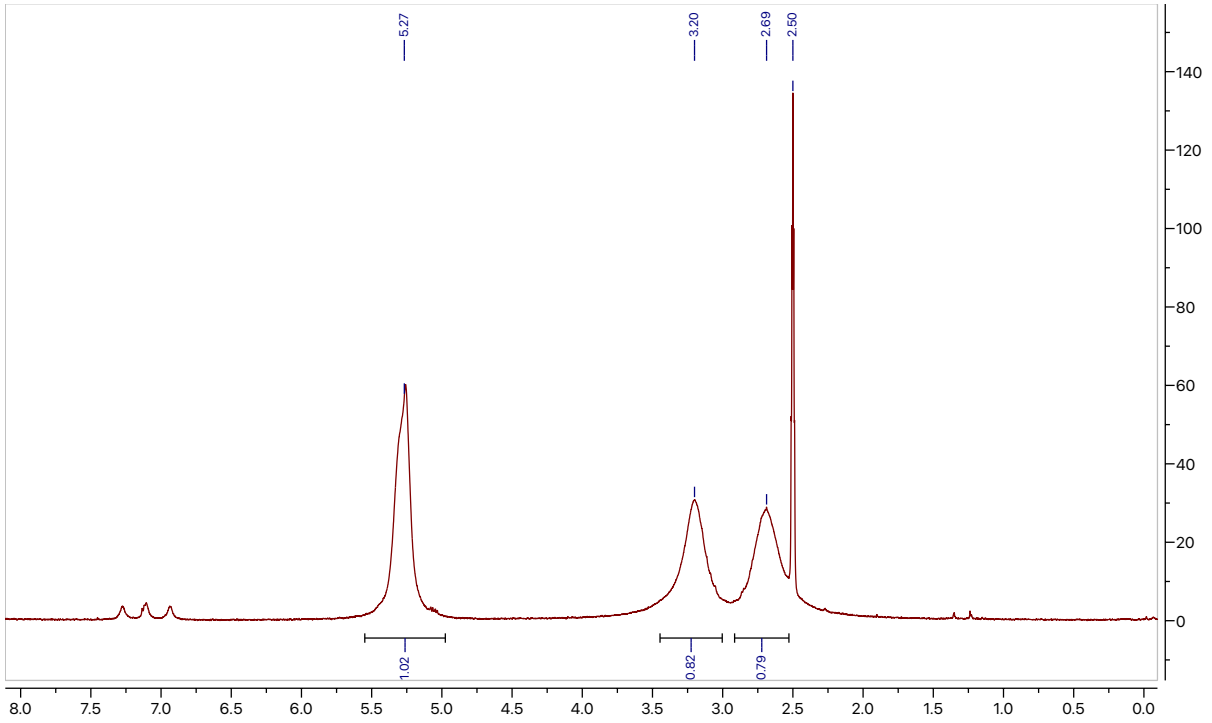

Figure S56. ^{1}H NMR (300 MHz, 298K, D_6-DMSO) spectrum of PSI. δ (ppm): 5.27 (br s, 1H, CH), 3.20 (br s, 1H, CH_2), 2.69 (br s, 1H, CH_2).

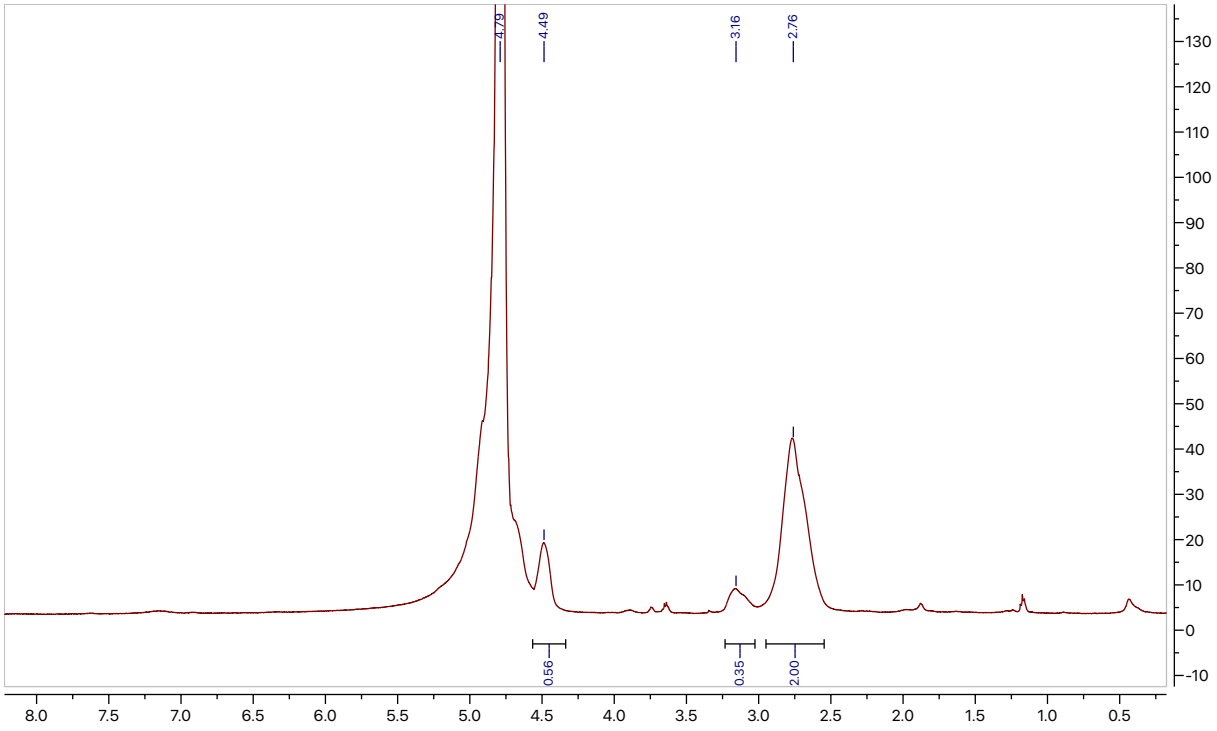

Figure S57. ^{1}H NMR (500 MHz, 298K, D_2O) spectrum of NH_4OH treated PSI. δ (ppm): 4.49 (br s, 1H, CH), 3.16 (br s, 2H, CH_2 (pendant $CONH_2$)), 2.76 (br s, 2H, CH_2 (pendant COOH)).

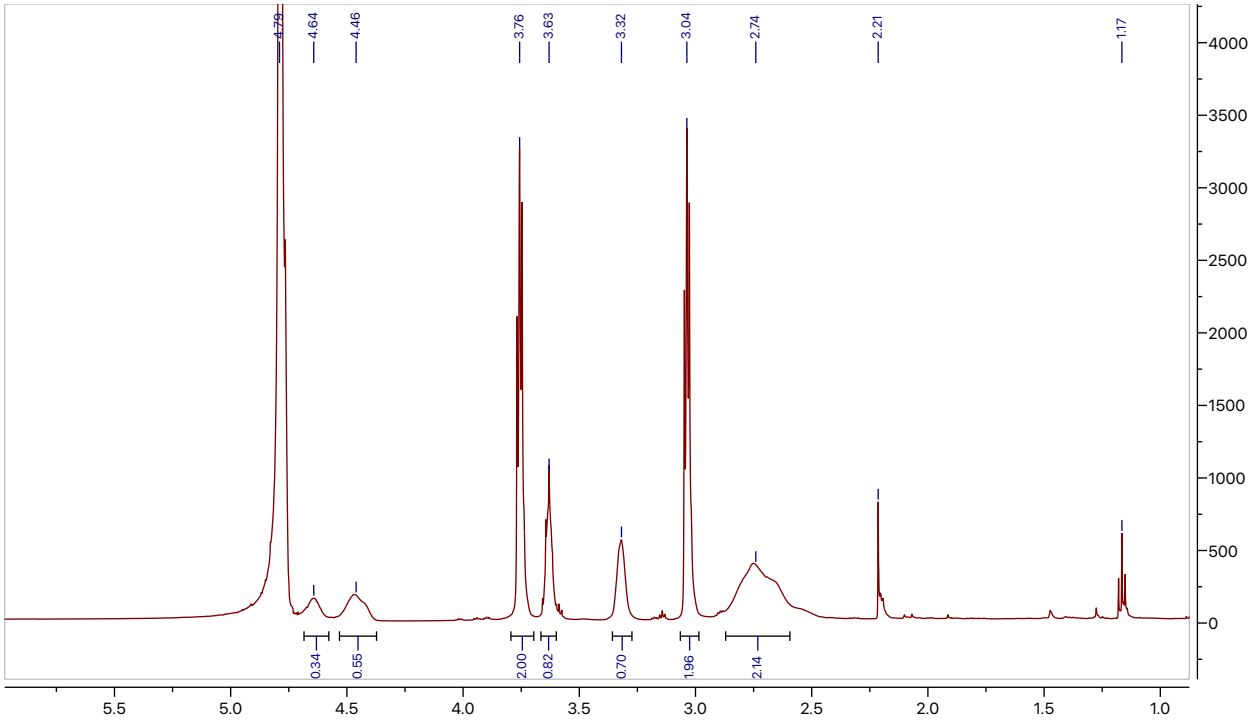

Figure S58. ^{1}H NMR (500 MHz, 298K, D_2O) spectrum of PHEA. δ (ppm): 4.64 (br s, 1H, α-CH), 4.46 (br s, 1H, β-CH), 3.76 (t, 2H, CH_2CH_2OH), 3.04 (t, 2H, CH_2CH_2OH), 2.74 (br s, 2H, CH_2CON). The peaks at 3.63 and 3.32 are thought to be the methylene units on the pendant ethanolamine residue as reported in *Polym. Chem.* **2017**, *8* (12), 1872-1877, but variable temperature NMR would need to be run to confirm.

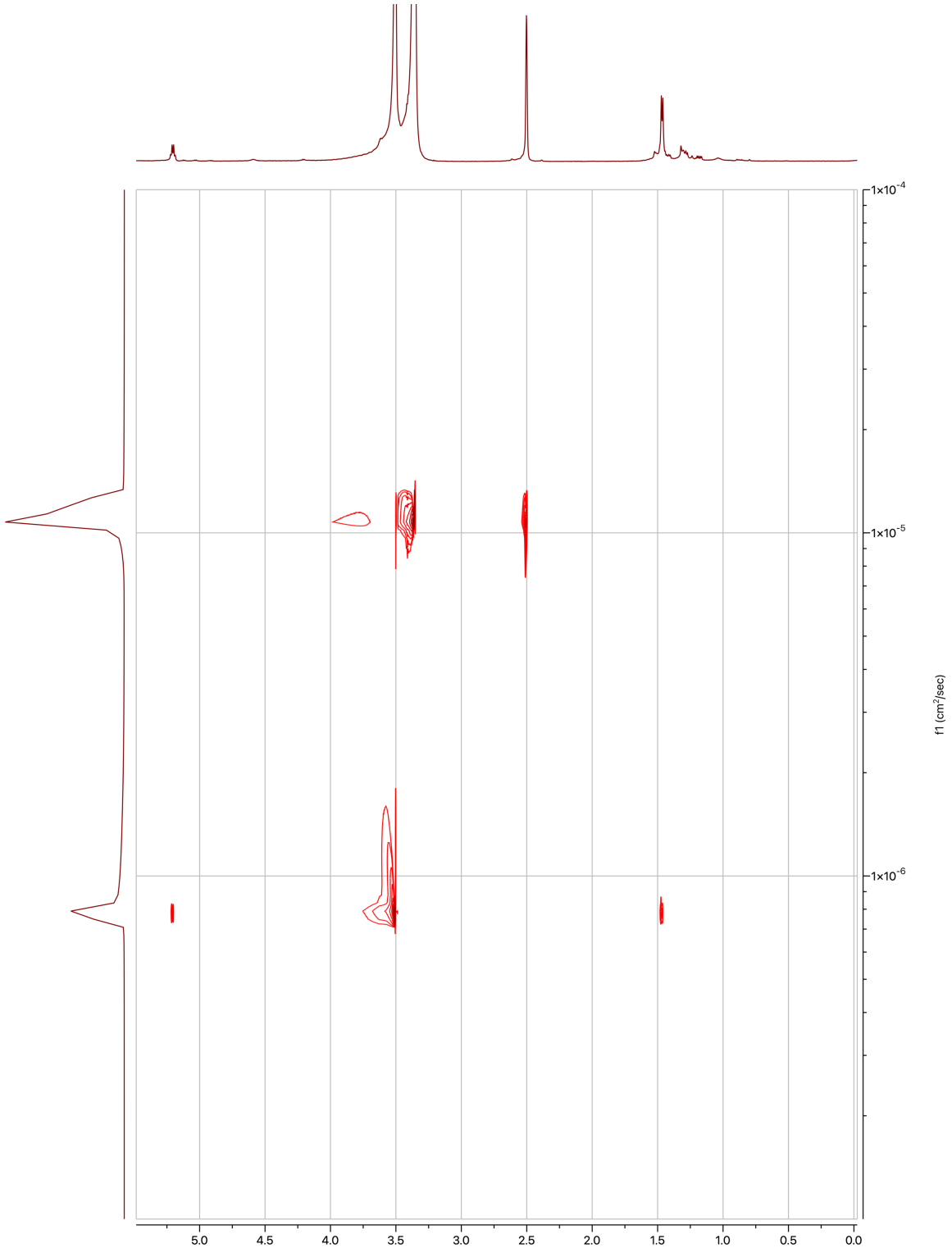

Figure S59. DOSY (600 MHz, 298K, d_6-DMSO) of the product obtained (a mixture of PLA and PEG) after PEG quenching.

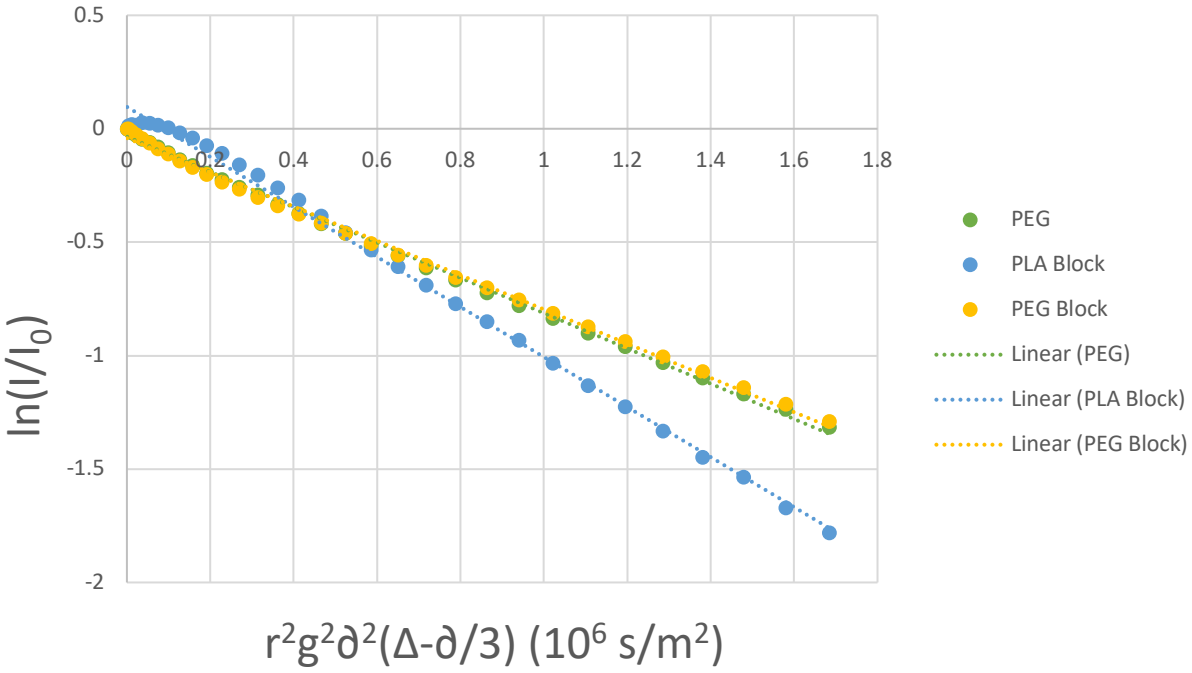

Figure S60. Stejskal-Tanner plot of the diffusion activity of the PEG and PLA in the product of the PEG quenching experiment.